ÉCOLE DE TECHNOLOGIE SUPÉRIEURE
UNIVERSITÉ DU QUÉBEC

THESIS PRESENTED TO
ÉCOLE DE TECHNOLOGIE SUPÉRIEURE

IN PARTIAL FULFILLMENT OF THE REQUIREMENTS FOR
A MASTER'S DEGREE IN MECHANICAL ENGINEERING
M. ENG.

BY
Brendan REHEL

EXPERIMENTAL INVESTIGATION OF FLAME STRUCTURE OF CO2-DILUTED SYNGAS AND BIOGAS MIXTURES BY LASER DIAGNOSTICS

MONTRÉAL, JULY 9, 2013

BOARD OF EXAMINERS (THESIS M. ENG.)

THIS THESIS HAS BEEN EVALUATED

BY THE FOLLOWING BOARD OF EXAMINERS

Mr. Patrice Seers, Thesis Supervisor
Département de génie mécanique à l'école de technologie supérieure

Mr. François Garnier, Member of the Board of Examiners
Département de génie mécanique à l'école de technologie supérieure

Mr. Mathias Glaus, President of the Board of Examiners
Département de génie de la construction à l'école de technologie supérieure

THIS THESIS WAS PRESENTED AND DEFENDED

IN THE PRESENCE OF A BOARD OF EXAMINERS AND PUBLIC

ON JUNE 27, 2013

AT ÉCOLE DE TECHNOLOGIE SUPÉRIEURE

ACKNOWLEDGEMENTS

I would first and foremost like to thank my research advisor, Dr. Patrice Seers. The guidance and support received from Dr. Seers throughout my time at l'ÉTS has been a major source of encouragement. Thank you for helping make this project an extremely gratifying and fulfilling experience.

My family deserves the honour of being acknowledged for their patience and support throughout my academic development. They represent my first ever network of support and they have never once left my side. Upon completing this body of work, I can only hope that I have made them proud. That is what I truly care about the most.

The staff at l'ÉTS has provided me with the tools necessary for the completion of this project. Technicians Alain and Michel have been extremely helpful in preparing and arranging the laboratories and equipment. I must also thank Pascale Ouimette, Simon Bergeron and Étienne Plamondon for letting me learn from their own research experiences, as well as Alana Battiston for being my motivator. Furthermore, I would like to thank the Pöyry Montréal office for their understanding as I completed the writing of my thesis.

As well, I would like express my appreciation towards Rolls-Royce Canada for the creation of this project. In particular, Michael Johnson's leadership and initiative were very influential. The input from Rolls-Royce as well as all the universities involved in this project created a terrific collaborative environment.

Finally, I must give special mention to McGill University for providing me with the fundamentals of mechanical engineering. On this note, I must praise Dr. Andrew Higgins, my former professor of Thermodynamics II at McGill University. Not only did your lectures open my eyes to combustion theory, but your unique perspective on engineering and science has changed my life more than you will ever know.

EXPERIMENTAL INVESTIGATION OF FLAME STRUCTURE OF CO2-DILUTED SYNGAS AND BIOGAS MIXTURES BY LASER DIAGNOSTICS

REHEL, Brendan

ABSTRACT

The primary objective of this research project is to experimentally investigate the laminar flame structure of syngas and biogas mixtures through Raman laser spectroscopy. The gaseous fuel mixtures have been predetermined by an industrial partner and are composed of varying concentrations of H_2, CO and CH_4 with CO_2 dilution. The laminar flame structure was characterized through measurements of flame temperature as well as major species concentration (H_2, CO, H_2O, CO_2, O_2, N_2 and CH_4 where applicable) at standard temperature and pressure conditions. The target operating conditions were set at an equivalence ratio of 3 and a Reynolds number of 1400. In total, four different groups of fuel mixtures are represented in this study: 1) one biogas fuel with 40% CO_2 dilution; 2) four syngas fuels with CO_2 dilution; 3) three syngas fuels with 5% CH_4 and 20% CO_2 dilution; 4) two syngas-methane mixtures with CO_2 dilution. The analysis of the experimental results is divided into four sections, each one corresponding to a fuel group. Concerning the biogas with 40% CO_2 dilution, it was seen that CH_4 depletion occured at a radial distance which corresponds to the the maximum concentration of H_2O and the minimum concentration of O_2. The maximum temperature was located at the flame's reaction boundary whereas much of the central axis of the flame was occupied by unburned reactants. The syngas mixtures with 25% CO_2 dilution demonstrated that a decrease in H_2/CO ratio causes a decrease in flame temperature due to an increase in radiative heat loss stemming from the additional CO_2 production. An increase in flame cone length, or a decrease in laminar burning velocity, was noted in conjunction with decreasing H_2/CO ratio. Conversely, increasing H_2/CO ratios coincide with higher levels of H_2O production and shorter flame cones. CO_2 addition causes a decrease in flame size as well as a decrease in flame temperature. Regarding syngas mixtures with 5% CH_4 and 20% CO_2 dilution, the experimental results suggest that the CH_4 reacts and/or dissociates early, within the first 10% of the flame's visible height. It was shown that the height of flame cones decreased in conjunction with increasing H_2/CO ratio, suggesting an increase in laminar burning velocity. The flames of methane-syngas mixtures with CO_2 dilution provided evidence of CH_4 dissociation early in the flame's development since measured H_2 and CO concentrations increased slightly. It was noted that the maximum concentration of H_2O occurred at the same radial location as the maximum temperature. In general, reaction boundaries of laminar, partially premixed flames of all syngas and biogas mixtures could be identified by a decrease in the concentrations of the unburned reactants and an increase in the concentrations of H_2O and CO_2. The reaction boundary is also characterized by an increase in O_2 and N_2 concentrations. The flame temperature reduces to room temperature beyond this reaction boundary.

Keywords: Synthesis gas, Flame structure, Laminar flame, Raman spectroscopy, Fuel

EXPERIMENTAL INVESTIGATION OF FLAME STRUCTURE OF CO2-DILUTED SYNGAS AND BIOGAS MIXTURES BY LASER DIAGNOSTICS

REHEL, Brendan

RÉSUMÉ

Ce projet de recherche a pour but d'examiner expérimentalement la structure de flamme laminaire par spectroscopie Raman et ce, pour différents syngas et biogaz. Les carburants gazeux, qui ont été prédéfinis par un partenaire industriel, sont composés d'une combinaison de H_2, CO et CH_4 et de la présence d'un diluant, le CO_2. Plus précisément, la structure de flamme pour chaque carburant à été défini par des mesures de température de flamme ainsi que des mesures des espèces majeures dans la flamme (dont l'H_2, CO, H_2O, CO_2, O_2, N_2 et CH_4 où approprié) à une richesse de 3, une nombre de Reynolds de 1400, et une température et pression standard. Au total, quatre groupes de carburants ont été considérés dans cette étude : 1) un carburant biogaz avec 40% CO_2; 2) quatre carburants de syngas avec dilution de CO_2; 3) trois carburants de syngas avec 5% CH_4 et 20% CO_2; 4) deux mélanges de méthane-syngas avec dilution CO_2. Ainsi, l'analyse des résultats expérimentaux a été divisée en quatre sections, chacune correspondant à un groupe de carburants. En ce qui concerne le biogaz avec 40% CO_2, les résultats démontrent que la position radiale de la valeur maximale d'H_2O correspond à la position radiale d'une concentration de CH_4 égale à zéro ainsi que la position où l'O_2 atteint une valeur minimale. La valeur maximale de la température se situait à la frontière de la réaction chimique de la flamme. Toutefois, l'axe central de la flamme se composait largement de carburant imbrûlé. Les quatre carburants syngas avec dilution de 25% de CO_2 démontrent qu'une diminution du ratio H_2/CO entraine une diminution dans la température de flamme en raison d'une augmentation des pertes de chaleur par radiation causée par la croissance de la production de CO_2. La diminution du ratio H_2/CO provoque aussi une augmentation de la hauteur du cône interne de la flamme, ce qui indique une baisse de la vitesse de flamme laminaire. De plus, l'augmentation du ratio H_2/CO amène une croissance de la production d'H_2O et une diminution de la hauteur du cône interne. L'addition de CO_2 au carburant cause une diminution de la hauteur de flamme ainsi qu'une réduction de la température de flamme. Concernant les flammes de syngas avec 5% CH_4 et 20% CO_2, les résultats démontrent que le CH_4 réagit et/ou se dissocie tôt dans l'évolution de la flamme. La hauteur du cône interne de la flamme diminue avec l'augmentation du ratio H_2/CO, indiquant une augmentation de la vitesse de flamme. L'addition de l'H_2 peut augmenter la vitesse de flamme grâce aux effets chimiques sans influencer la température de flamme adiabatique. Les deux mélanges méthane-syngas avec dilution CO_2 démontrent que le CH_4 dissocie tôt dans le développement de la flamme. La concentration maximale de l'H_2O s'y trouve à la même distance radiale que la température maximale. Parmi tous les carburants, les frontières de réaction pour les flammes laminaires partiellement prémélangée sont caractérisées par la diminution de la concentration des réactants, une augmentation des produits de combustion, et la diminution de la température de flamme à la valeur ambiante.

Mots clés : Syngas, structure de flamme, flamme laminaire, spectroscopie Raman, carburant

TABLE OF CONTENTS

Page

LIST OF TABLES

LIST OF FIGURES

LIST OF ABBREVIATIONS AND ACRONYMS

GHG	Greenhouse gas
ID	Inner diameter
IR	Infrared
LFL	Lower flammability limit
LIF	Laser induced fluorescence
PLIF	Planar laser induced fluorescence
UFL	Upper flammability limit
UV	Ultraviolet
Nd :YAG	Neodymium-doped yttrium aluminum garnet

LIST OF SYMBOLS AND MEASUREMENT UNITS

Greek Symbols:

α	Premixed flame half cone angle
Δw	Raman shift expressed in wave number
λ	Wavelength
ρ	Density
ρ_u	Density of unburned gas
φ	Equivalence ratio
σ	Standard deviation
σ_R	Rayleigh scattering cross section
σ_{R_N}	Normalized Rayleigh scattering cross section
θ	Scattering angle
υ	Frequency
χ	Molar fraction
χ_i	Molar fraction of a given species in ambient condition
χ_j	Molar fraction of a given species in flame condition

Latin Symbols:

a	Velocity gradient
A_f	Flame surface area
B_i	Fixed error
B_{X_i}	Bias limit
c	Speed of light
d	Bunsen burner cylinder diameter
E	Energy
h	Planck's constant
H_T	Flame height
I	Intensity of Rayleigh signal
$\dot{m}_u$	Mass flow rate of unburned gas

n	Particle refractive index
N_T	Number of performed measurements
$\dot{Q}_u$	Volumetric flow rate of unburned gas
Re	Reynolds number
s^{-1}	Stretch rate
S	Average flame speed
S_L	Laminar flame speed
$S_L{}^o$	Unstretched laminar flame speed
$s_u{}^o$	Laminar burning velocity
$S_{\bar{X}_i}$	Precision index
t	Student's *t* multiplier
T	Temperature [K]
T_{ad}	Adiabatic flame temperature [K]
$U_{0.95}$	Uncertainty of a measurement
$(U_y)_{max}$	Uncertainty of an experimental result
v	Velocity of premixed gas
v_u	Unburned gas velocity
$v_{u,n}$	Normal of the unburned gas velocity
z*	Normalized height $\frac{z}{H_T}$

Species:

C	Carbon
CH_4	Methane
CO	Carbon monoxide
CO_2	Carbon dioxide
H	Hydrogen atom
H_2	Hydrogen
H_2O	Water
N_2	Nitrogen

O	Oxygen atom
O_2	Oxygen
OH	Hydroxyl group

Measurement Units:

atm	Atmosphere
°C	Degrees Celsius
cm	Centimetres
cm^{-1}	Per centimetre
cm/s	Centimetres per second
g	Gram
Hz	Hertz
J	Joule
K	Kelvin
kg	Kilogram
kg/m^3	Kilograms per cubic metre
L	Litre
Lpm	Litres per minute
mm	Millimetre
N	Newton
nm	nanometres
W	Watts

INTRODUCTION

The concentrations of most greenhouse gases (GHG) in the atmosphere have been rising steadily for over a century, prompting the creation of emission laws and policy which govern the amount of pollutants that can be legally released into the environment. Many industrialized countries currently find themselves having to demonstrate how their adjustments to climate policy have achieved quantifiable decreases in their GHG emission levels. In order to abide by the increasingly stringent emission standards, the need for cleaner energy sources is more important than ever. Although progress has been made, there is still increasing pressure to further reduce emissions. In the pursuit of cleaner energy solutions, syngas and biogas are considered to be appealing fuels.

The main combustible syngas constituents are H_2 and CO although it generally contains varying amounts of CO_2, CH_4, H_2O and N_2 as well according to Prathap *et al*. (2008). The many different possible compositions of syngas are due largely to the various gasification processes used for a wide range of organic materials. Some examples of syngas production include mainly the gasification of coal, waste-to-energy gasification, and steam reforming of natural gas or liquid hydrocarbons. On the other hand, biogas is a different type of biofuel composed primarily of CH_4 (45-70%) and CO_2 (25-55%), sometimes with traces of H_2S and/or N_2. Biogas is produced from the biological breakdown of biodegradable materials such as biomass, sewage, animal manure and various forms of waste.

Ideally, flexible combustors will be developed in order to treat a wide variety of biofuels. In order to properly design and develop these flexible combustors, a full spectrum of syngas and biogas flame characteristics need to be properly researched and defined. This study covers a portion of a much larger investigation by Rolls Royce Canada into uncovering the potential of various mixtures as a cleaner fuel for gas turbine operation. The objective of this study is to investigate the combustion characteristics of ten gaseous mixtures, primarily syngas including varying concentrations of H_2, CO and CH_4 with CO_2 as diluent. This portion of the project covers the investigation of flame structure through Raman laser spectroscopy at

standard temperature and pressure. Results will serve to characterize the combustion of these fuels particularly at standard temperature and pressure conditions, whereas combustion at gas turbine conditions will be treated in a different study. As well, the results from each mixture will be compared between similar fuels and, where applicable, compared to literature data.

This report is divided in the following manner: firstly, a literature review chapter will provide the reader with the context of the study. This will serve to explain how this study contributes to the field of renewable fuel research. In doing so, previous studies will be explored to give insight into the various possible approaches and methods to characterizing syngas combustion.

The second chapter covers the experimental approach used in this study. This includes the methodology and setup leading to the flame length, species concentration and flame temperature measurements. Subsequently, the chapter will conclude with an explanation regarding the procedure of estimating the experimental uncertainties.

The experimental results from this study are presented in the third chapter. Both qualitative observations and quantitative data are presented in this chapter. Experimental data is presented as radial profiles of both temperature and major species concentrations. An analysis of the results will accompany the experimental data in an attempt to characterize the ten flames.

The report ends with general conclusions regarding flame structure. Details concerning the problems and limitations encountered in the project will also be discussed as it will ultimately help future studies in successfully characterizing the combustion of syngas and biogas mixtures.

CHAPTER 1

LITERATURE REVIEW

Before getting into the details of this particular experiment, it is important to review several topics concerning laminar flames and how to characterize them. An overview of syngas and biogas combustion will be covered, which includes mixing, flame temperature and flame stability. As well, laser spectroscopy measuring procedures will be described in detail since it is an integral part of the spectroscopic experimental process. Although it has been removed from the project's scope, a review of laminar flame speed is included since it may contribute to the understanding of this study. The chapter concludes with a summary of previous works.

1.1 Combustion of Syngas and Biogas

There are many important elements to cover when discussing the combustion of syngas and biogas. Section 1.1 is designed to provide the background information required for understanding the concepts involved in this paper.

1.1.1 Premixed and Nonpremixed Combustion

In general combustion systems, a fuel and an oxidizer must interact and mix in order to guarantee combustion. For this reason, mixing is a key theme in combustion and gives rise to the categorization of premixed and nonpremixed combustion. According to Law (2006), nonpremixed (or diffusion) flames are produced when the fuel and oxidizer are separated, interacting only at the combustion zone. In diffusion flames, the mixing of the fuel and oxidizer is controlled by diffusion, hence the name. The fuel and oxidizer mix stoichiometrically in this case. On the other hand, Law (2006) states that premixed flames occur when the fuel and the oxidizer are thoroughly mixed before the reaction takes place. In a premixed flame, the availability of all the reactants results in a thinner, more stable flame. Fuel lean mixtures designate mixtures in which there is an excess (more than the stoichiometric value) of the oxidizer in the premixed fuel-oxidizer mixture. Conversely, fuel

rich mixtures contain an excess of fuel. Fuel rich combustion can share characteristics of both premixed and nonpremixed flames. For instance, a fuel rich mixture can react, consuming all the available oxidizer, while producing a diffusion flame further downstream as the excess fuel draws ambient air to complete the reaction.

1.1.2 Laminar and Turbulent Flames

Laminar flames acquire their name from the "laminar" flow of the combustible mixture. More specifically, it means that the mixture's flow is characterized by smooth, distinct streamlines. Similarly, a turbulent flame is characterized by the turbulent flow of its mixture. Law (2006) describes turbulent flow can be described as chaotic in motion, with abrupt changes in pressure, velocity and direction. The chaotic nature of turbulent flow makes it ideal for mixing, which makes nonpremixed mixtures more prone to turbulence since the mixing of reactants is ultimately required.

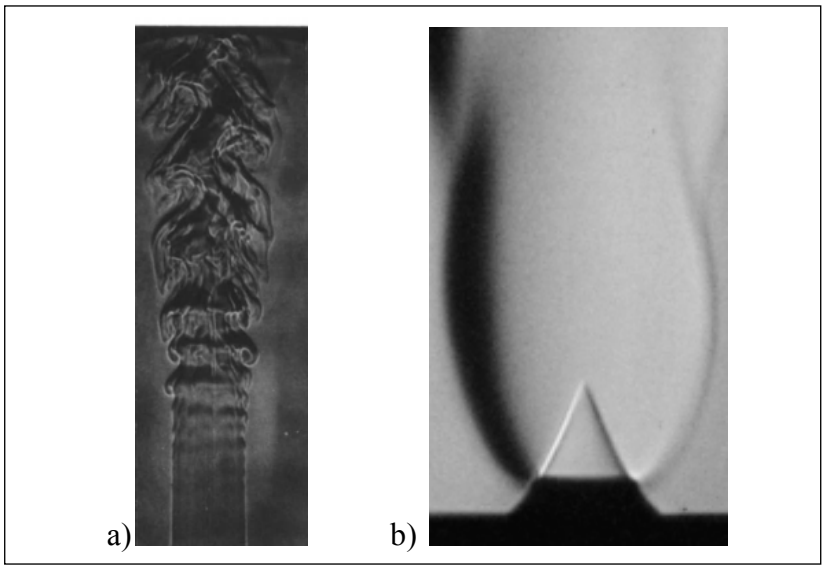

Figure 1.1 Schlieren imagery depicting the visible differences between a) a typical turbulent flame and (b) a laminar flame Taken from Eickhoff (1982) and Bouvet (2011) respectfully

The visible differences between laminar and turbulent flames can be seen in Figure 1.1. On the left, the turbulent flame is characterized by its chaotic appearance, whereas the laminar

flame on the right of the image is characterized by its smooth appearance. Laminar and turbulent flame regions can be referred defined with respect to flow velocity, as well as the transition process from laminar to turbulent. According to Law (2006), the transition zone can be represented in terms of Reynolds number, a ratio of inertial forces to viscous forces, at a value of approximately 2300. The laminar regime falls below this value and the turbulent regime lies above it.

1.1.3 Adiabatic Flame Temperature

Adiabatic flame temperature, represented as T_{ad}, is an important factor in the analysis of combustion and flames. In "Combustion Physics" by Law (2006), it is explained as the final temperature attained given the combustion of a uniform mixture with an initial temperature and pressure, in which the mixture achieves chemical equilibrium through an adiabatic, isobaric process. Several factors influence T_{ad}, such as the pressure, the initial temperature and the initial composition of the mixture. The equivalence ratio also has a direct influence on T_{ad}, generally peaking in value close to stoichiometry. As the mixture becomes leaner or richer, the value of T_{ad} will decline mostly due to the losses involved in heating the excess reactants.

1.1.4 Flame Stability

For many reasons, it is desirable to have the ability to keep a flame stationary in space. Having the ability to do so implies that a flow of fresh mixture can be delivered to the combustion site at the exact same rate at which the fuel is being burned. In industrial applications, this typically describes the desired performance within a combustor for continuous and predictable operation (for example, a gas turbine or a furnace). Practically speaking, a perfect and continuously-balanced flame is impossible to accomplish. Furthermore, constant operating conditions can very rarely be guaranteed. According to Law (2006), the purpose of flame stabilization is to supply a means by which a flame can be flexible enough to adjust its location, orientation and configuration in a non-uniform, temporally varying flow field. However, stabilization will not always be possible, and the

domain of unstable systems leads to a discussion of concepts such as flashback and blowoff. For burner-stabilized flames, flashback is a phenomenon in which the velocity of the oncoming mixture has decreased to a level below the burning rate, causing the flame to propagate against the flow of the mixture and back into the tube (which can be quite dangerous). Blowoff describes more or less the opposite scenario, in which the velocity of the unburned fuel mixture increases to a value, lifting the flame off the burner. Initially, as the flame is lifted off the burner from the increased flow of the mixture, the burning rate will also increase since there is less heat lost to the burner rim, creating a higher temperature and faster reaction. However, there is a limit at which point the burning rate cannot be further increased and the lifted flame can no longer be sustained. Evidently, the dynamic balance between flame speed and velocity is achieved between the points of flashback and blowoff. In Figure 1.2, curve 3 represents the state in which flow velocity is higher than the flame speed, annihilating the flame at some elevation above the burner rim.

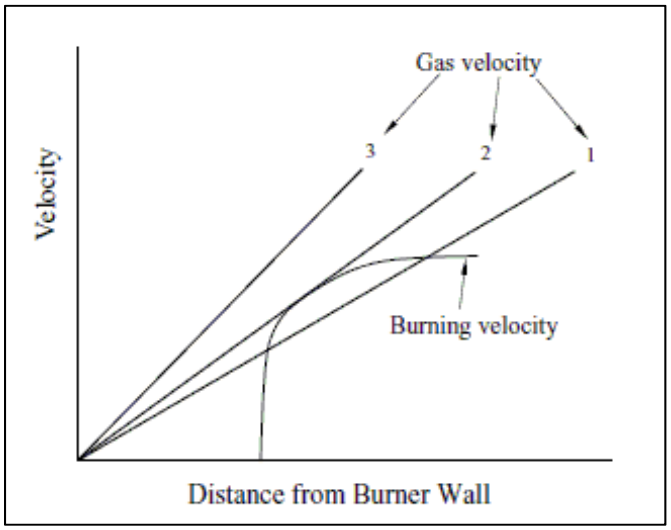

Figure 1.2 Representation of flashback and blowoff
Taken from C.K. Law, Combustion Physics,
Cambridge press (2006, p. 360)

Curve 2 displays the initial state in which flashback is possible, whereas curve 1 is a stronger depiction of the state of flashback, where the velocity of the combustible gas is lower than the burning velocity.

From Williams (1985), a flammability limit of a combustible mixture refers to the composition, temperature or pressure in which the mixture cannot be made to burn. Naturally, the flammability limits of a system involve a lower (LFL) and an upper flammability limit (UFL). The LFL represents the lean limit condition whereas the UFL designates the rich limit condition of the system at a given temperature and pressure. Generally, the flammability limits pertain to the combustion of fuel in air.

Table 1.1 Flammability limits in terms of
equivalence ratio of some common fuel-air mixtures at 1 atm
Taken from C.K. Law, Combustion Physics, Cambridge press (2006, p. 347)

Fuel	**Lower Flammability Limit**	**Upper Flammability Limit**
Hydrogen	0.10	7.14
Carbon Monoxide	0.34	6.8
Methane	0.50	1.67
Propane	0.56	2.7
Benzene	0.56	3.7
Butane	0.57	2.8

Flame reattachment is a seldom researched phenomenon that describes the reattachment of a lifted flame to the nozzle from which the unburned fuel exits. According to Lee and Chung (2001), flame reattachment is due to a nonlinear decrease in a flame's liftoff height at a particular balance between propagation speed and flow velocity. This phenomenon may be a function of flow velocity, mass/molar fraction, and nozzle diameter, although the exact conditions for flame reattachment require further investigation. Furthermore, there has been relatively little research in regards to the stabilization of a flame from reattachment.

Another flame phenomenon worthy of mention is the occurrence of flame flicker. Shepherd *et al*. (2003) describes flame flicker as a buoyancy-driven oscillation, where vortices are formed due to the interaction of the hot burned gas and the cold ambient air, as seen in Figure 1.3. It is also explained that the frequencies of the flame oscillations can be associated to

several system parameters. In general, the characteristic frequencies of oscillation are in the range of 10 to 20 Hz.

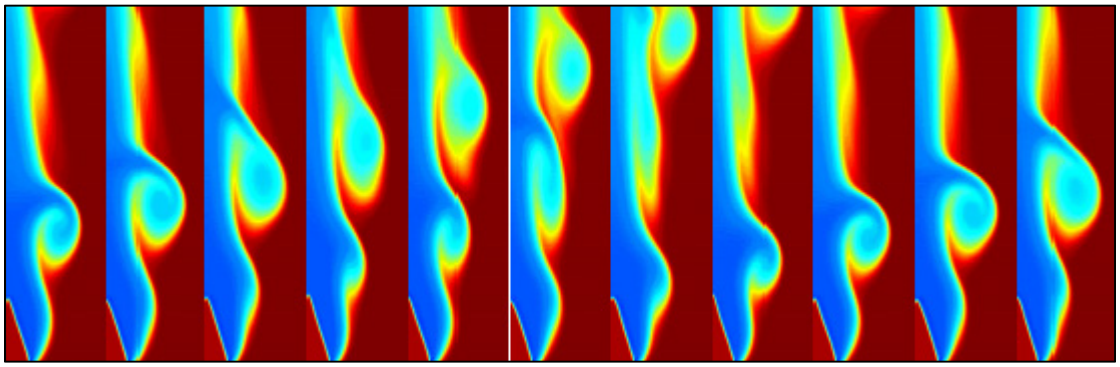

Figure 1.3 Density field representation of vortex evolution over time
Taken from Shepherd *et al*. (2003)

1.2 Laser Spectroscopy

Laser spectroscopic measurement techniques are commonly used in combustion studies. They provide non-obtrusive methods of measuring combustion characteristics in laminar and turbulent flames, such as temperature, density and species concentration. In previous studies, such as Ouimette (2012), laser spectroscopic techniques were successfully used for in-flame measurements of temperature and species concentration. If desired, laser spectroscopy can also be used to measure other characteristics such as velocity flow fields. In this section, the various laser spectroscopic measurement techniques will be examined so as to assess their potential worth to this study.

1.2.1 Raman Spectroscopy

When light is scattered from a light source, the majority of the photons are scattered elastically. Elastic scattering refers to the situation in which the scattered photons maintain the same frequency as the incident photons. However, not all photons are elastically scattered. A very small minority of photons undergoes inelastic scatter; a scenario in which the frequencies of the scattered photons differ from that of the incident photons. When the

scatter is inelastic, it is referred to as Raman scattering since the process is due to the Raman effect. The Raman effect simply refers to the alteration in the wavelength/frequency of light when a light beam is deflected by molecules. This effect was first witnessed by the Indian physicist Sir Chandrasekhara Vankata Raman in 1922.

From Hollas (2004), the frequency (or wavelength) of a photon is related to energy, E, through the Planck relation as seen in Equation (1.1), where υ denotes the frequency of the photon, λ is the wavelength, c represents the speed of light and h refers to Planck's constant:

$$E = h\upsilon = \frac{hc}{\lambda} \qquad (1.1)$$

This implies that when the frequency or wavelength of a scattered photon differs from that of the incident photon, there is a corresponding change in energy. This corresponding change in energy has been associated with transitions between different vibrational and rotational energy states of the scattering molecule. Typically, Raman applications focus on vibrational transitions due to their larger, more observable shifts. The small rotational shifts generally are not used except when applied to simple gaseous molecules.

The difference in energy between the incident and scattered photons can be demonstrated visually as seen in Figure 1.4:

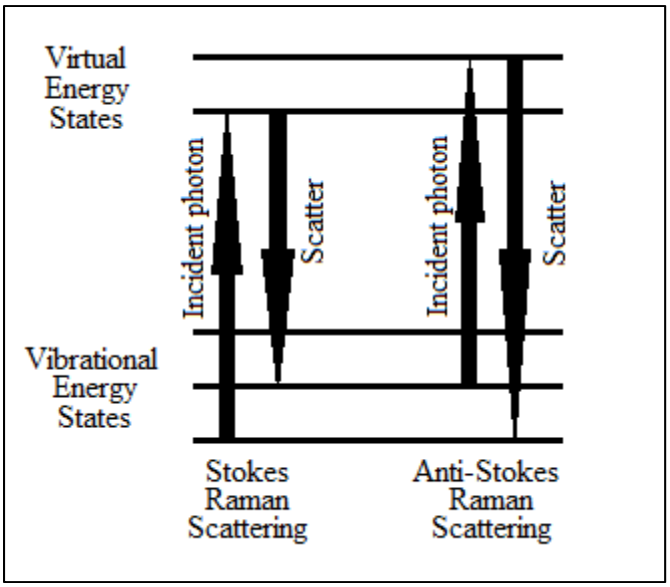

Figure 1.4 Raman scattering energy level diagram
Taken from The Internet Journal of
Vibrational Spectroscopy (2004)

The arrows in Figure 1.4 are of different lengths in order to display the difference in energy between the incident and scattered photons. On the left, the Stokes shift corresponds to a higher final vibrational energy state of the molecule. This means that the scattered photon is shifted to a lower frequency in order for the system's total energy to remain constant. Conversely, when the final vibrational energy state of the molecule is lower than the inital state, the scattered photon is shifted to a higher frequency. This is illustrated in the right of Figure 1.4 and it is referred to as an Anti-Stokes shift. The Raman shift can be calculated using Equation (1.2), where λ is the wavelength given in cm and Δw is the Raman shift expressed in wave number, given in cm^{-1} as explained in Hollas (2004):

$$\Delta w = \frac{1}{\lambda_{incident}} - \frac{1}{\lambda_{scattered}} \qquad (1.2)$$

A normal mode of vibration is a pattern of motion in which the components of a system moving sinusoidically with the same frequency and with a constant phase angle. An object, such as a bridge, a building or a pipeline, has a set of normal modes which depend on several

factors such as the design of the system as well as the materials used. The system can achieve any of its normal modes depending on the conditions set upon it, such as loads, earthquake, wind, etc. A similar concept applies to molecules, where the normal modes of vibration simply refer to the vibrational states of the molecule which depend on the sinusoidal motion of the molecule's atoms. The molecule can achieve its vibrational states by absorbing or emitting energy due to the interaction of incident photons. Linear molecules with N atoms possess 3N-5 normal modes, whereas non-linear molecules possess 3N-6 normal modes. The vibrational spectrum of a molecule is dependent on its "design", including the mass and arrangement of each of the molecule's atoms, which is analogous to the "design" of a structure in the physical world. The vibrational spectrum is therefore unique to each molecule and can be referred to as the "fingerprint". This implies that if the Raman scattering characteristics of a certain species are known, useful properties and information of the species can be measured. Vibrational spectra are particularly useful in the study of molecular structure. For gases, the combination of rotational and vibrational spectra is useful in the study of combustion reactions.

Raman spectroscopy usually involves shining a laser beam onto a sample and collecting the incident light with a lens. This collected light is sent to a monochromator in which the elastic Rayleigh scattering is filtered out. The remaining Raman spectral response provides information about the vibrational modes of the molecules under investigation. This process can be applied to most solid and liquid samples. Gases produce less visible Raman effects due to their relatively low concentrations of molecules (at normal pressures), so special equipment may be required. Typically, a stronger laser is required in order to deliver a more intense beam of light in gaseous applications according to Hollas (2004).

Raman spectroscopy can be applied to the study of mixtures. Each species within a mixture can be observed simultaneously due to each species' characteristic Raman spectral response. For a given species, the characteristic Raman line pattern will vary in intensity depending on the number of scattering molecules in the mixture sample. The relative concentrations of each species are directly proportional to the relative intensity of each response, which makes

Raman spectroscopy a particularly useful tool in studying species concentrations. Other properties such as density and temperature can be derived by measuring these intensities. Figure 1.5 illustrates the general Raman spectroscopy experimental arrangement suitable for the study of a combustible mixture. A more detailed description of the Raman scattering laser diagnostic setup will follow in Chapter 2.

The major disadvantage of Raman spectroscopy is the weakness of the Raman scattering signal. The signal strength is relatively weak in comparison to that of elastic scatter.

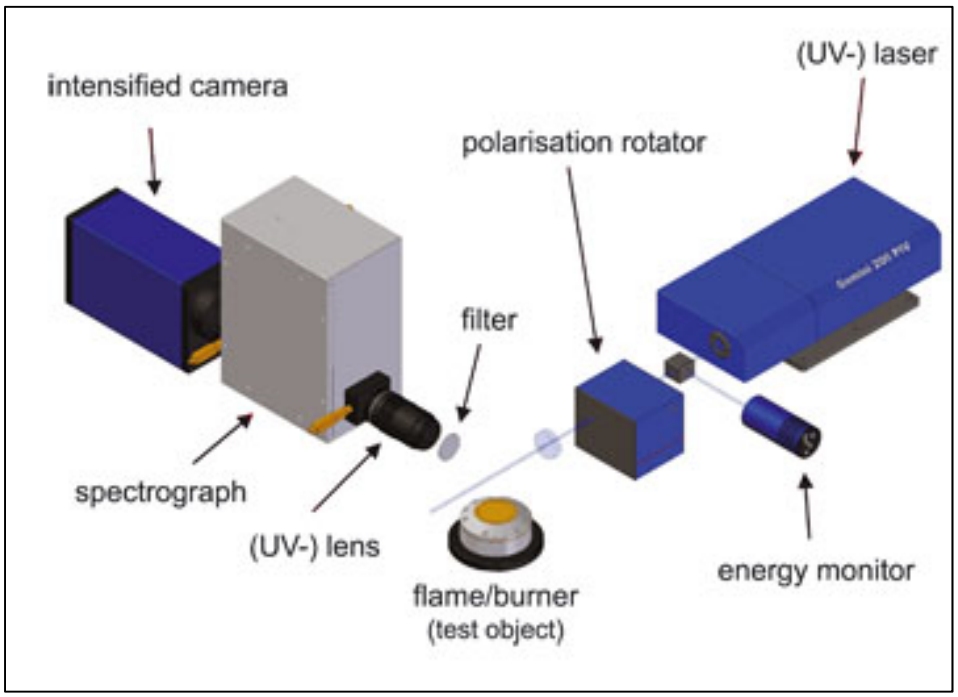

Figure 1.5 An illustration of a Raman spectroscopy experimental setup
Taken from *LaVision* website

1.2.2 Rayleigh Scattering

Rayleigh scattering refers to the elastic scatter encountered during the interaction of an incident photon with a particle much smaller than the wavelength of the light. This scenario applies to gas phase molecules which makes Rayleigh scattering particularly useful for gas applications. The elasticity of the interaction is illustrated in Figure 1.6:

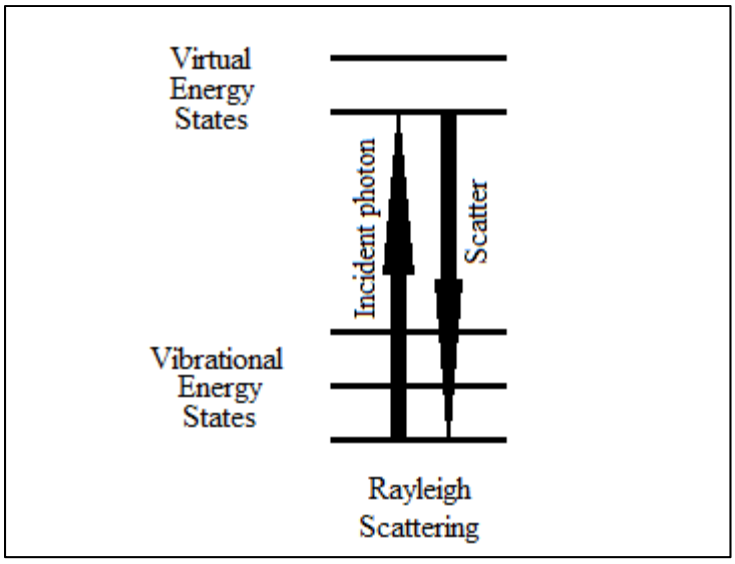

Figure 1.6 Rayleigh scattering energy level diagram
Taken from The Internet Journal of
Vibrational Spectroscopy (2004)

The combination of particle size and the wavelength of the incident light determines the extent of Rayleigh scatter for a given light beam. The intensity of scattered light is related to particle size and wavelength in Equation (1.3). From Hollas (2004):

$$I = I_0 \frac{1 + \cos^2 \theta}{2R^2} \left(\frac{2\pi}{\lambda}\right)^4 \left(\frac{n^2 - 1}{n^2 - 2}\right)^2 \left(\frac{d}{2}\right)^6 \qquad (1.3)$$

The intensity of scattered light due to a single particle is denoted by I, the initial beam of light of wavelength λ is denoted by I_o and the scattering angle is θ. The size of the small particle is represented by its diameter d and the distance to the particle is given by R, whereas n refers to the particle's refractive index. Equation (1.3) demonstrates that low-wavelength (or high-frequency) light is more susceptible to scattering. The blue sky owes its colour to this phenomenon since the shorter blue wavelengths are more intensely scattered than the longer red wavelengths.

Since Rayleigh scattering lacks the Raman shift “fingerprint”, Rayleigh scattering is not useful for determining species concentration. However, if the mole fractions of all major species in a sample are known, Rayleigh scattering can be an effective tool for determining the properties of the sample. Specifically, planar temperature fields can be derived from Rayleigh scattering provided the gas composition is known. The intensity of the Rayleigh signal is much stronger than the Raman signal, which makes Rayleigh spectroscopy a more suitable procedure for determining temperature fields of gases provided the constituent species concentrations are known.

The experimental setup for Rayleigh spectroscopy is usually similar to that of Raman spectroscopy (seen in Figure 1.5). Typically, a laser sends a beam of light onto a sample and the incident light is collected with a lens. However, in this case the Rayleigh scattering is not filtered out from the collected light. Although the similarities in the two experimental approaches makes it simple and natural to utilize combined Raman and Rayleigh techniques.

1.2.3 Laser Induced Fluorescence

Laser induced fluorescence (LIF) involves the excitation of a sample’s molecules to higher energy levels through the absorption of photons (typically from a laser beam). Some of these molecules fluoresce by de-exciting and emitting photons at a wavelength longer than the incident light’s wavelength. The level of fluorescence is dependent on the species concentration as well as the temperature and pressure of the sample. The emitted fluorescent light is usually captured by a photomultiplier tube. The excitation light can be filtered out since it is of a different frequency than the fluoresced light.

LIF imaging usually involves a procedure referred to as planar laser induced fluorescence (PLIF). Typically, PLIF uses a pulsed laser beam as a light source. The beam of light from the laser is usually fed through an arrangement of lenses and/or mirrors and emerges as a sheet of light which illuminates the fluid of interest. The resulting fluorescence is delivered through a filter and captured by a camera. If the fluid is not composed of a fluorescent

substance, the flow can be seeded with a fluorescent marker or tracer. An advantage of PLIF is that many combustion fuel species can be visualized directly without the need of markers or tracers. PLIF enables the determination of several flow variables, some of which include temperature, density, pressure and velocity. It is also known to have a high sensitivity in comparison to Rayleigh and Raman techniques, having the ability to detect species at the ppm level. Figure 1.7 illustrates a typical PLIF experimental setup.

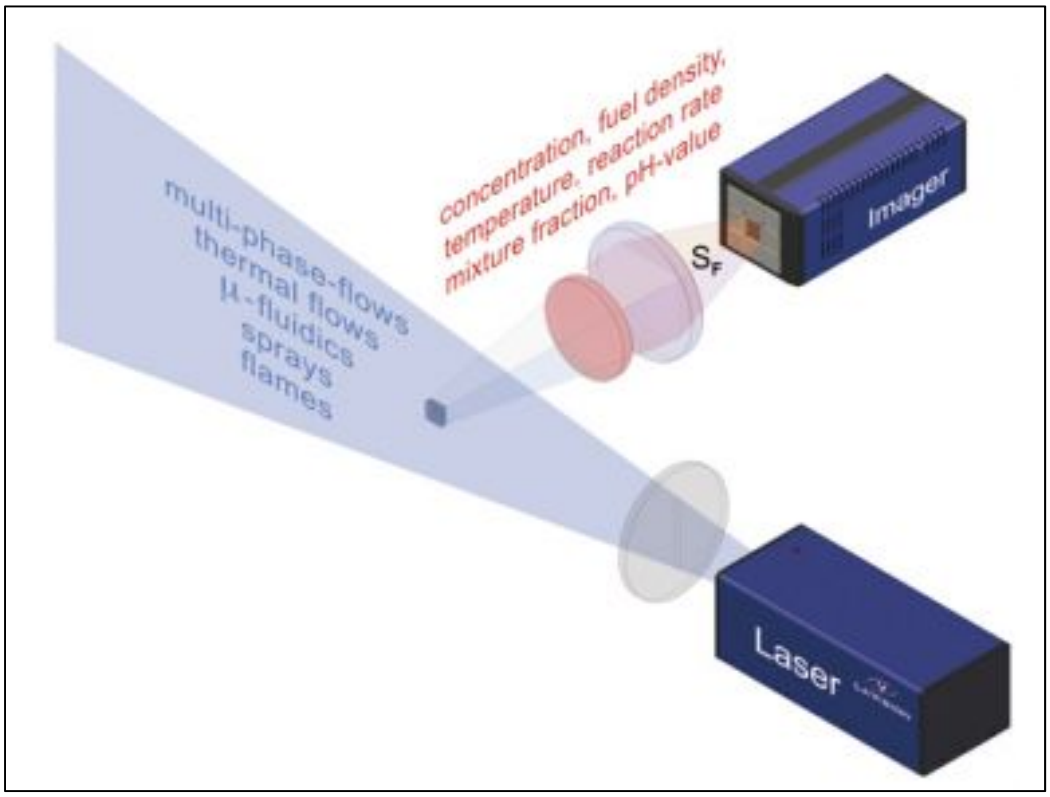

Figure 1.7 An illustration of a typical planar laser induced fluorescence experimental setup. Taken from the *LaVision* website

1.3 Laminar Flame Speed

The design of combustion engines cannot be accomplished without a thorough grasp of the laminar flame speeds of combustible gases. Laminar flame speed describes the propagation speed of an unstretched laminar flame. The term is often used interchangeably with "laminar burning velocity", although they differ slightly in meaning; laminar burning velocity refers

specifically to the *property* of a combustible mixture that describes the velocity of the combustion reaction relative to the unburned gas. Although there still remain several questions surrounding the structure of propagating laminar flames, equations do exist for use in theoretical analyses.

When Mallard and le Chatelier initially studied deflagration, it was believed that heat loss was the central factor affecting the propagation of laminar flames. The rates of chemical reactions were thought to affect these speeds to a lesser extent. According to Williams (1985), it was Mikhel'son who demonstrated that the burning velocity is proportional to the square root of the reaction rate as well as the square root of the ratio of the thermal conductivity to the specific heat at constant pressure. More recently, the development of asymptotic concepts within the scope of laminar flame theory has helped improve the accuracy with which burning velocity is calculated.

The influence of initial pressure on laminar flame speed is a topic of interest in combustion research. As initial pressures increase, it has been shown that laminar burning velocities decrease. This phenomenon is evident in Hu *et al*. (2009) as demonstrated both experimentally and numerically with hydrogen-air mixture. However, it was also demonstrated that an increase in initial pressure induces cellular instability and ultimately leads to an increase in flame instability. Tse *et al*. (2000) conducted a separate study to further examine the effects of pressures up to 60 atm on hydrogen flame propagation. Using the combustion bomb method (see Section 1.3.2), Law witnessed the flame instability at high initial pressures lead to the onset of heavy wrinkling on the flame surface at as low as 5 atm. This observation has particular significance because it reveals how the assumption of a smooth flame can be very misleading. The flame may appear to decrease in propagation rate as initial pressure increase. However, the heavy wrinkling increases the surface area over which the chemical reactions are taking place, resulting in a faster burning rate than had been originally observed. Law suggests that the flame may simply be trying to respond to the increase in pressure by creating wrinkles to maintain a higher burning rate. Note that this fundamental discovery in no way states that an increase in initial pressure results in an

increase in flame speed, but it opens the door to new research objectives. As well, this is yet another example of why it is important to visually record the deflagration.

Conversely, initial temperature conditions have shown little effect on flame stability. Nevertheless, an increase in initial temperature has shown to produce an increase in unstretched flame propagation as well as unstretched laminar burning velocity in Tang *et al*. (2008).

The influence of equivalence ratio on laminar flame speed can be partially investigated by analyzing its effect on flame temperature, although this does not apply to very rich mixtures in which case flame speed becomes increasingly limited by the rate of diffusion. Due to the heat of combustion and heat capacity of reaction products, it is a well-known phenomenon that maximum flame temperatures are found at slightly rich equivalence ratios, as stated by Tse *et al*. (2000). Consequently, the maximum flame temperature generally corresponds to the maximum laminar flame speed for combustible gases. Over a range of different equivalence ratios, one could expect a bell-curve-shaped graph in which the maximum lies slightly above $\varphi = 1$. An example of the typical relationship between laminar flame speed and equivalence ratio can be seen in Figure 1.8, which has been lifted from Appendix IV. It is worthwhile to note that the opposite relationship describes the laminar flame thickness with respect to equivalence ratio. As demonstrated by Tang *et al*. (2008) for a propane-hydrogen-air mixture, the relationship produced a U-shaped curve in which the minimum flame thickness was found around stoichiometry. Once again, this relationship does not apply to very rich mixtures.

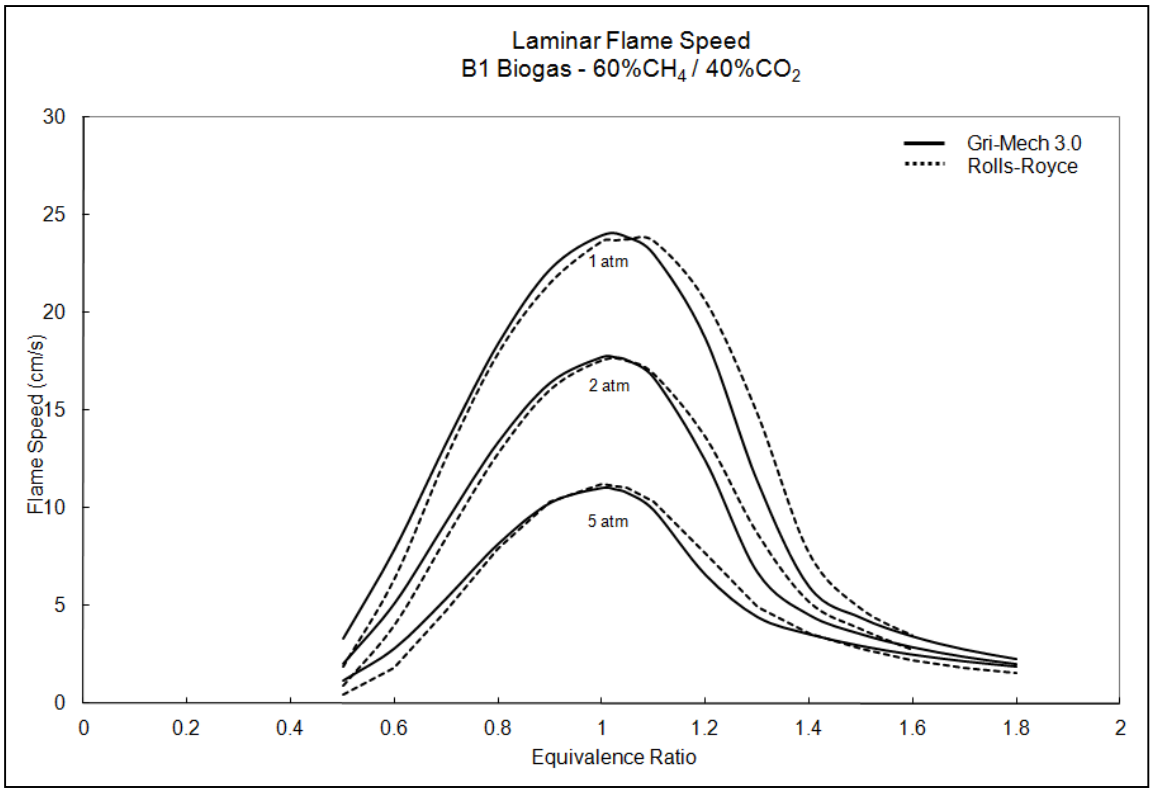

Figure 1.8 Example of the typical relationship between laminar flame speed and equivalence ratio at varying pressure

Another important consideration in laminar flame speed experimentation is the fuel type. Alkanes (such as methane, ethane and propane) are generally known for having lower laminar flame speeds. Alkenes (such as ethylene) generally have slightly faster burning velocities and reach higher flame temperatures at laminar flame speed, whereas alkynes burn faster still. The simplest of all fuels, hydrogen, is known for being reactive and possessing a very high burning velocity. Based on the findings of Tang *et al*. (2008), it can be expected that an increase in hydrogen percentage will render the mixture more reactive and thus increase the laminar flame speed. This explains hydrogen's presence in so many combustible gas mixtures. Not only does hydrogen have high thermal and mass diffusivity, but it also lacks the reaction of carbon monoxide to carbon dioxide present in hydrocarbon reactions. Monteiro *et al.* (2010) presents a comprehensive account of laminar burning velocities for various syngas mixtures.

Researchers have developed several different methods of experimentally measuring laminar flame speed, each method with its own level of uncertainty. The main techniques and their derivatives as observed in the literature will be described. The three main approaches to be discussed here are the Bunsen flame method, the combustion bomb method, and the stagnation flame method.

1.3.1 Bunsen Flame Method

The Bunsen flame method is a popular approach to determining laminar flame speed. Typically, this approach involves a premixed mixture flowing with a velocity *v* through a cylinder of diameter *d*. The air-fuel mixture produces a conical, fuel-rich inner flame surrounded by a diffusion flame. When the flame is stable, both the premixed and diffusion flames remain stationary. Although it has been shown by Echekki and Mungal (1991) that the flame speed is not constant over the entire flame surface, the Bunsen flame technique remains a popular method of determining laminar flame speed due to the simplicity of the experimental procedure. Perhaps the most significant drawback of this method is that it overlooks the influence of stretch on the flame speed measurements. Although the accuracy of the Bunsen flame method has been questioned, critical analyses have shown that it can produce results of sufficient accuracy.

As the gaseous mixture exits the burner, the normal of unburned gas velocity is equivalent to the flame speed for perfectly stationary flames. This is the principle behind the flame angle method. As seen in Figure 1.9, by measuring the angle $\propto$ between the premixed flame edge and the direction of the unburned gas velocity v_u, the flame speed *S* is equal to the normalized unburned gas velocity, $v_{u,n}$, and can be easily calculated according to Equation (1.4):

$$S = v_{u,n} = v_u \sin \propto \qquad (1.4)$$

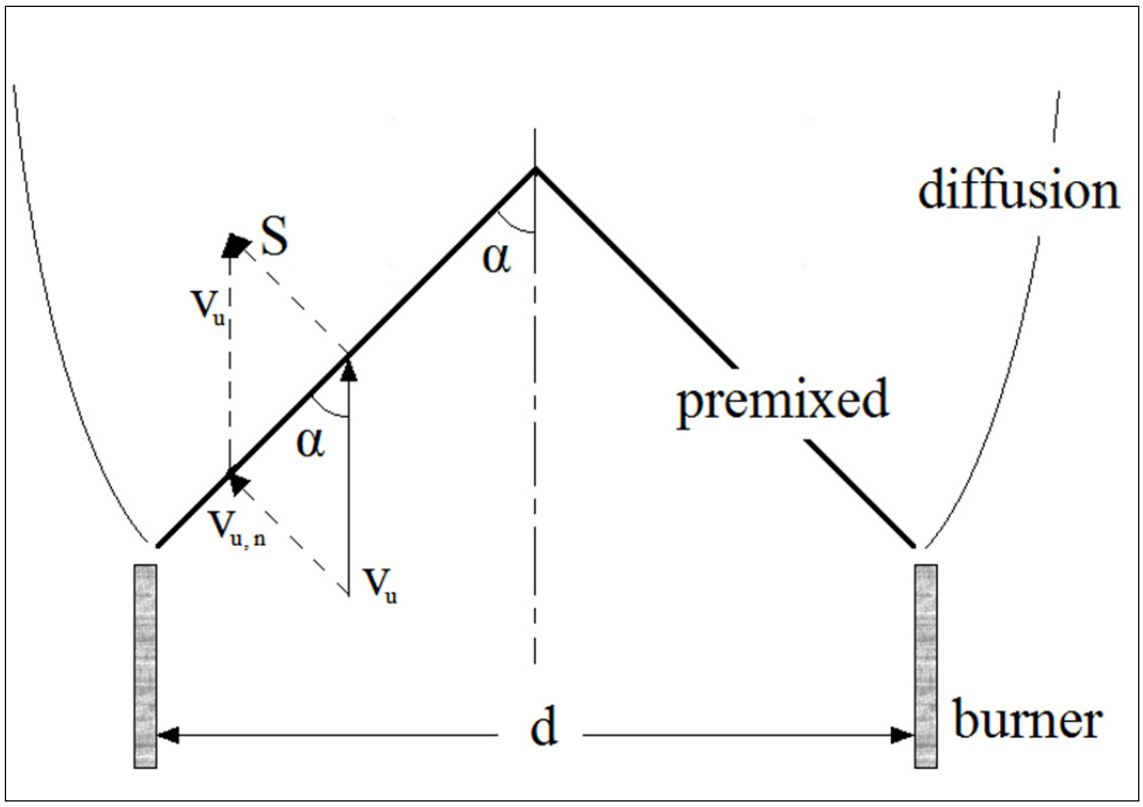

Figure 1.9 Bunsen burner apparatus depicting the angle
between the premixed flame edge and the unburned gas velocity
Taken from C.K. Law, Combustion Physics, Cambridge press (2006, p. 264)

In this approach, burners with contoured nozzles are generally favoured since they attempt to neutralize boundary layer effects. These boundary layer effects cause straight cylindrical burners to produce parabolic exit velocity profiles, which in turn causes premixed flames to be parabolic in shape as well. Contoured nozzles result in stabilized flames that are more conical in shape. This provides straighter edges with which to measure the flame's half cone angle α, but it does not guarantee straight edges. In Bouvet *et al*. (2011), contoured nozzle burners were utilized in determining the laminar flame speeds of a range of syngas mixtures composed of H_2/CO/Air. Despite the varying gas flow rates, it was observed that the contoured nozzles failed to produce straight-sided conical flames under each of the scenarios examined. The data from the flame angle method was used to compare with results obtained from another popular Bunsen flame approach called the flame area method, also under investigation by Bouvet *et al*. (2011) in the same study. In the flame area method, the

average laminar flame speed is calculated by dividing the gas flow rate by the surface area of the flame. If $\dot{m}_u$ and $\dot{Q}_u$ are respectively the mass and volume flow rates of the unburned gas, ρ_u is the unburned gas density and A_f is the flame surface areas, then the conservation of mass states in Equation (1.5):

$$\dot{m}_u = \rho_u S A_f \quad (1.5)$$

$$S = \frac{\dot{m}_u}{\rho_u A_f} = \frac{\dot{Q}_u}{A_f} \quad (1.6)$$

Since Equation (1.6) divides the gas flow rate over the surface area of the flame, there is an inherent assumption that the flame speed is constant over the entire surface area of the flame. As stated earlier, the flame speed is not constant over the surface area of the flame, meaning the flame area method does not calculate the true laminar flame speed S_L. Equation (1.6) solves for an averaged flame speed *S* that can closely approximate S_L when utilized carefully.

It is common for direct imaging techniques to successfully capture the flame edges. Schlieren or shadow photography tend to produce flame images with enhanced flame edge clarity. Traditionally, the inner edge of shadowgraph imagery has provided the best results due to its proximity to the unburned flame surface. Another valid technique involves tracing the flame edge by recording the maximum OH* chemiluminescence emission. In Bouvet *et al*. (2011), the OH* chemiluminescence methodology was even preferred over Schlieren diagnostics since it provided results comparable to the literature without the use of complex tracking techniques.

Although the flame angle and flame area approach appear quite straightforward due to the simplicity of Equations (1.5) and (1.6), they encounter complications in other areas. Due to the large difference in temperature between the flame and the burner rim, there is always a heat loss to the rim which reduces the flame speed. As well, with smaller diameter burners, the calculated flame speed increases approaching the flame tip when using Equation (1.4). This is due to the flame's curvature at the apex of the cone. As the flame edge approaches the

centerline, α approaches 90° and in turn, S approaches v_u. Since the flame surface does not produce a perfect cone, surface identification is difficult and stretch effects often go unaccounted for. This inconvenience can be eluded by using a flat-flame burner, reducing the 2-dimensional Bunsen flame to a 1-dimensional flat flame. This planar flame is normal to the unburned gas flow direction. The surface area of the flame is easily and accurately defined which reduces the potential for error. Applying Equation (1.6) produces the laminar flame speed. However, the flat-flame burner is non-adiabatic. The flat, porous burner has a cooled surface on which the flat flame is stabilized. Although this method eliminates the problem of stretch due to curvature, it yields a burning velocity lower than the true unstretched burning velocity ($S_L{}^o$) due to heat loss at the burner surface. In spite of this, measurements can be corrected for heat loss by varying the gas flow and tracking the corresponding cooling rate, then extrapolating the cooling rate to zero as explained in Law (2006).

1.3.2 Combustion Bomb Method

This method involves measuring a spherically expanding flame kernel in a combustion bomb ignited at the center of the combustion chamber. Rallis and Garforth (1980) concluded in their study that the spherical constant-volume combustion bomb method is the most versatile and accurate for experimentally determining the laminar flame speed. Typically, combustion chambers for this purpose are spherical in order to complement the flame's assumed spherical shape. The flame's spherical shape should nonetheless be verified visually upon experimentation if this method is to be used.

The flame propagates outward at the combustible mixture's laminar flame speed, thus the point of ignition is purposely located at the center of the chamber to allow for maximum propagation before disturbance from the chamber walls. As the deflagration wave spreads, the total amount of products from the reaction increases and the chamber pressure increases accordingly. Furthermore, the unburned gas upstream of the propagating flame is compressed, which in turns heats the unburned gas. As the unburned gas is subjected to higher pressures and temperatures, the initial state no longer applies within the confines of

the chamber. The combustion bomb experiment must therefore take this into account by measuring the pressure and temperature of the unburned gas over the course of the deflagration. Another option is to limit data acquisition to the time period in which the flame size is relatively small. In doing so, the pressure and temperature upstream of the flame should approximate the initial state to the point where the difference can be discounted. However, by limiting the data acquisition period to a smaller time window, the need for strong acquisition tools becomes more significant. Luckily, thanks to the increased use of better data acquisition systems, many of the problems inherent to the combustion bomb method have been overcome over the years or have been proven to be insignificant, according to Rallis and Garforth (1980).

The best option in laminar flame experimentation is to record the deflagration with a high speed photography system. This is the most direct way of documenting the history of the flame's spherical expansion. The rate of change of this radius is thus the flame propagation rate. This procedure requires optical windows within the chamber to record the flame progression. Commonly, the windows on such chambers are diametrically opposed and made of quartz, which can withstand high pressures and temperatures. It is best to include pressure and temperature sensors to monitor the state of the unburned combustible mixture. According to Gu *et al*. (2000), once significant pressure variation has commenced within the chamber, a pressure-time curve can be used to calculate the laminar flame speed. This makes it possible to cross-reference the calculated flame speed values with the observed values from the photography, as originally done by Manton *et al*. (1953). As well, if a high speed photography system cannot be obtained, the pressure history can serve as the single experimental input. The cube-root-law has been the most recognized model applied to a pressure-time curve in order to estimate the burning velocity and flame thickness.

The calculation of laminar flame speed from the pressure-time curve does come with its drawbacks. Since the pressure variations are more significant once the flame is relatively large, more time has passed for other outside factors to affect the deflagration, such as buoyancy. The deflagration is not homogeneous, meaning the reaction does not occur

uniformly throughout the vessel. Instead, the quantity of hot products increases and the quantity of cold reactants decreases as the flame propagates. This presence of hot products and cold reactants causes the spherical shape of the flame to adjust to more of a mushroom shape, according to Dahoe and de Goey (2003). Naturally, at lower burning speeds, buoyancy will be expected to introduce a greater degree of error. Evidently, it is risky to rely solely on the pressure-time curve as experimental input. The experiment can always be limited to the early portion of the pressure-time curve where it is safer to assume that the flame is spherical in shape, but pressure variations are less significant over this period so it can be problematic trying to determine which segment of data to use. A high-speed photography apparatus should be included within the experimental setup at least to verify the validity of the flame's spherical shape over time. At worst, if the spherical propagation of the flame tends to lose its shape, approximate corrections can be introduced as was done by Rallis and Garforth (1980).

The assumption is often made that there is no heat loss or gain from the burned or unburned regions. However, heat transfer is possible in several manners. For instance, heat may be transferred from the burned gas to the unburned gas, from the unburned gas to the walls of the chamber and also from the burned gas to the centrally positioned ignition system (particularly during the initial propagation phase). Heat transfer by radiation is also possible from the burned or unburned gases to the chamber walls, according to Rallis and Garforth (1980), who was able to show that heat transfer does occur but its effect is minimal. Generally, it is important to note that heat losses that reduce the flame temperature will also reduce the flame speed.

Since the pressure and temperature values change simultaneously within the chamber, correlations are required to account for their influence. These correlations offer an approach to circumventing the assumption that downstream pressure and temperature states at any instant are uniform throughout the unburned gas. Many correlations have been proposed over the years, many of which account for the temperature gradient downstream of the flame. This section will not cover the various correlations. Instead, it is simply important to note that

there exist correlations covering the influence of a wide range of unburned gas conditions. Parameters such as pressure, temperature and equivalence ratio can be simultaneously related to laminar flame speed for different fuel types. Each correlation comes with a certain degree of error and should only be used over the specified range.

1.3.3 Stagnation Flame Method

The stagnation flame method, sometimes referred to as the counterflow or twin flame method, involves the projection of two identical gas flows upon each other. This creates a "stagnation plane" at the location of collision. Igniting the system produces two symmetrical flat flames, each one located equidistantly on either side of the stagnation plane. Figure 1.10 depicts the stagnation plane and twin flame arrangement.

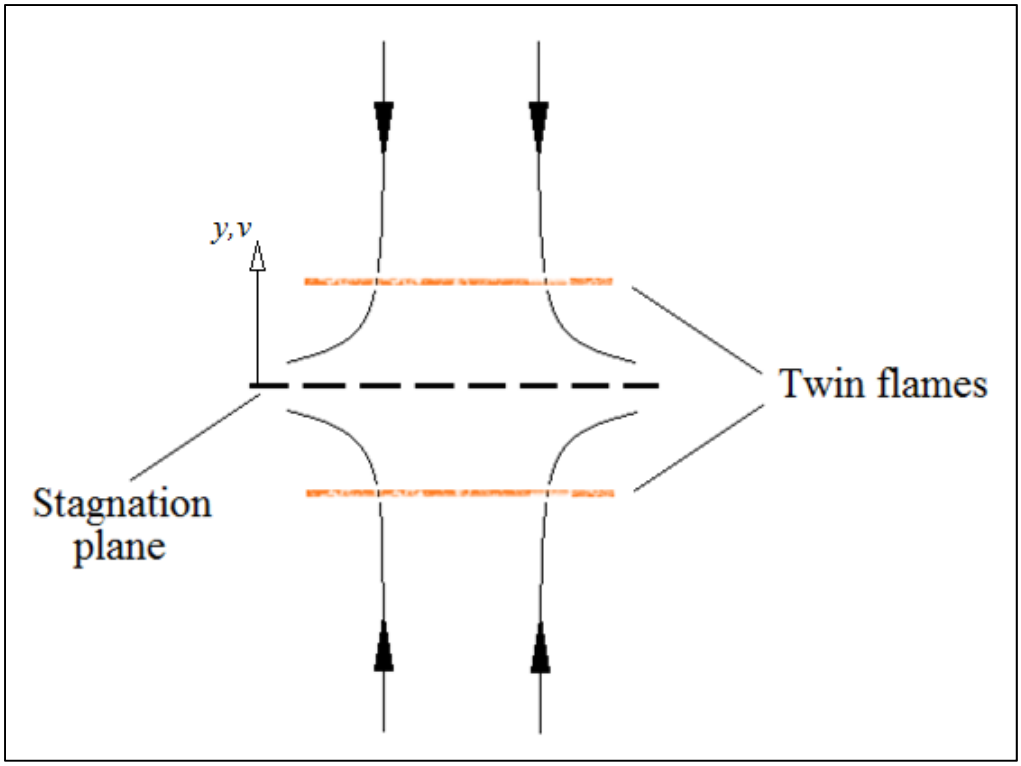

Figure 1.10 Depiction of the twin flames in the stagnation flame method
Taken from C.K. Law, Combustion Physics, Cambridge press (2006, p. 272)

In order to utilize this phenomenon for measurement purposes, it is necessary to understand the behaviour of the normal velocity component v with respect to the distance from the stagnation plane. As the gas flow approaches the stagnation plane prior to the preheat zone, the normal velocity decreases linearly according to Equation (1.7), where a is the velocity gradient as well as the stretch rate (s^{-1}) which is calculated in Equation (1.8):

$$v = ay \tag{1.7}$$

$$a = \frac{dv}{dy} \tag{1.8}$$

Entering the preheat zone, the increase in heat causes v to increase. In Figure 1.11, this decreasing trend is illustrated until v_{min}, after which point v increases linearly. At v_{max}, the increasing trend is once again reversed as the heat release is terminating and v approaches the stagnation flame. The v_{min} and v_{max} represent reference flame speeds at the upstream boundary of the preheat zone and the downstream boundary of the reaction zone respectively. In order to eliminate the stretch effect, v_{min} can be plotted against a and extrapolated to $a = 0$. The laminar burning velocity is simply equal to v_{min} at this intercept. Since v_{min} is used as the reference flame speed, the calculated laminar burning velocity represents s_u^o assessed at the upstream boundary. According to Law (2006), s_u^o is typically evaluated at the upstream boundary because heat loss and flow nonuniformity effects are minimized.

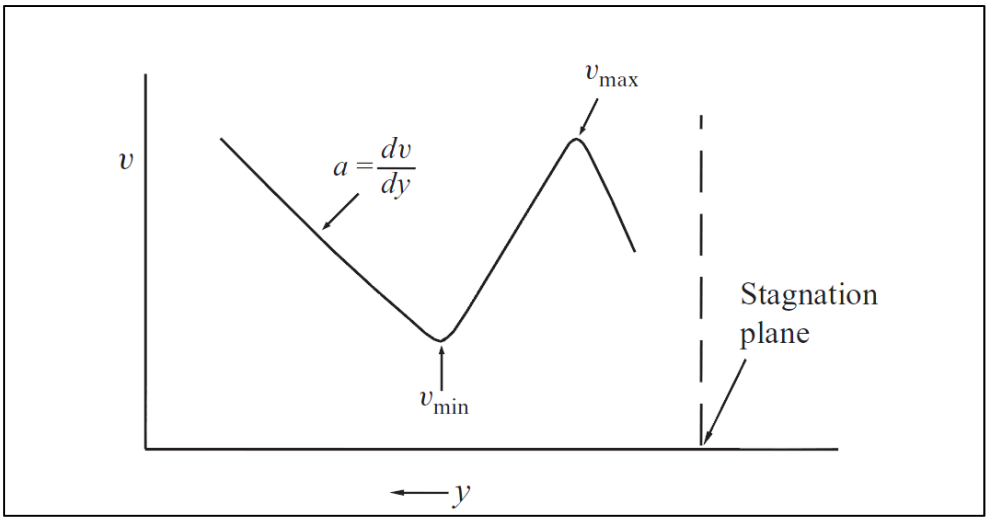

Figure 1.11 Axial profile illustrating the normal velocity of
the gas flow with respect to the distance from the stagnation plane
Taken from C.K. Law, Combustion Physics, Cambridge press (2006, p. 272)

1.4 Previous Works

This section contains a review of the studies conducted by other researchers that are similar in execution and/or subject matter to this project. At the time of this writing, there appears to be no available documentation of studies involving laser diagnostic techniques as a means to investigate flame structure of partially premixed laminar flames of $H_2/CO/CO_2$ or $H_2/CO/CH_4/CO_2$ mixtures. The majority of research conducted on partially premixed laminar flames of such mixtures concerns the measurement of laminar flame speed.

1.4.1 Flame Structure

Fernández *et al* (2006) studied lean, premixed CH_4/air laminar flames using Bunsen burner to stabilize the flames. The concentrations of the major species present in the flame as well as the flame temperature were measured using Raman spectroscopy. The objective of this study was to validate that Raman spectroscopy is an unobtrusive measurement technique that can be used to measure local properties in stationary flames. Experimental results from this study compared quite favourably with the literature.

Rabenstein and Leipertz (1998) used Raman spectroscopy to measure the major species concentrations (CH_4, H_2, H_2O, CO_2, N_2 and O_2) and temperatures of rich, partially premixed CH_4/air flames. The experimental measurements were obtained at various elevations above the exit of a dual flow burner, upon which the flame was stabilized. The results of the investigation concluded that the reaction zone can by identified by a region in which the unburned, premixed gas constituents decrease in concentration. This observation was coupled with an increase in molar fraction of the CO_2 and H_2O, which in this case represented the products of combustion. It was further shown that the boundary of the reaction zone is characterized by the diffusion of ambient air into the flame, which appeared in the Raman results as an increase in concentration of O_2 and N_2. This boundary was also represented in the temperature measurements, seeing as the temperature gradually reduced to ambient value towards the flame's periphery. As the elevation of the measurement increased with respect to the flame's height, this reaction zone boundary visibly shifted in the radial direction from the flame's central axis. The conclusion of this study was thus that Raman spectroscopy adequately provides a means of quantifying flame structure.

Han *et al*. (2006) studied the structure of low-stretch methane nonpremixed flames both experimentally and numerically. The objective of the study was to analyse the effects of flame radiation on flame response and extinction limits. The experimental setup involved generating a CH_4/N_2 flame using a porous, spherically symmetric burner with a large radius of curvature. Gas and flame temperatures were measure by Raman scattering while the temperature of the burner surface was measured by IR imaging. Furthermore, the reaction zone boundaries were illustrated through OH-PLIF and chemiluminescence imaging. The numerical investigation simulated low-stretch flame structure by accounting for detailed chemistry, thermodynamic/transport properties as well as radiative aspects. The study concluded with an agreement between the numerical results and the experimental observations.

Cheng *et al*. (2011) undertook an experimental and numerical investigation to characterize laminar premixed $H_2/CO/CH_4$/air flames at atmospheric conditions. The objective of the

study was to determine the effects of varying the fuel composition on the resulting flame characteristics at fixed stoichiometry. The experimental measurements were performed using an opposed-jet burner technique, which is described in Section 1.3.3 (stagnation flame method). The temperature and flame front position are measured and compared to results obtained from EQUIL and PREMIX numerical flame simulations. Flame structure was simulated using the OPPDIF package with the GRI Mech 3.0 mechanism. Cheng *et al*. (2011) concluded that the experimental measurements of flame front position and temperature were closely predicted by the simulations from the CHEMKIN codes. Furthermore, the chemical kinetic structures indicated that the increase in laminar flame speed associated with H_2 addition is probably owing to chemical effects as opposed to thermal effects.

1.4.2 CO_2 Dilution

Natarajan *et al*. (2007) studied the effect of CO_2 dilution on laminar flame speed on lean H_2/CO mixtures. The study covered a range of fuel compositions and CO_2 dilution levels and used a Bunsen flame approach, measuring the flame speed from images of the reaction zone area. The experimental results were compared to numerically simulated results; experimental data was compared to the GRI Mech 3.0 and Davis H_2/CO mechanisms, of which the Davis mechanism compared more favourably, particularly at higher H_2 concentrations. The study reports that flame speed decreases with increased CO_2 dilution due to the capability of CO_2 to lower the flame temperature by way of radiative heat transfer. More specifically, the CO_2 in the unburned fuel absorbs radiative energy from the hot products such as CO_2 and H_2O. The study concludes that the prediction models accurately predict the flame temperature and chemical effects related to CO_2 dilution.

Park *et al*. (2008) conducted a numerical study of H_2/CO syngas diffusion flames diluted with CO_2. The objective of the study was to gain further insight into the influence of fuel composition and flame radiation on flame structure and the oxidation process. The numerical results were compared to the models of Sun *et al*. and David *et al*., seeing as these models

were considered leaders in H_2/CO flame modelling. The investigation shows that losses in flame temperature are due to radiation increase as CO and CO_2 mole fractions increase. It was also demonstrated that H_2 and CO oxidation reaction pathways are sensitive to H_2/CO composition as well as the addition of CO_2.

An investigation of laminar burning velocities and flame stability was conducted by Burbano *et al*. (2011) for equimolar H_2/CO mixtures with dilution of two separate inert gases, CO_2 and N_2, at ambient conditions. Premixed laminar flames were produced using a contoured, slot-type burner and the angle method was used to calculate laminar flame speed from Schlieren imagery. The experimental measurements were compared to numerically computed results from three reaction mechanisms: Frassoldati *et al*., Davis *et al.*, and the H_2/CO/O_2 reactions of Li *et al*. The study concluded that N_2 and CO_2 dilution lowers the laminar burning velocity of the mixture due to the decrease in heat release and the increase in heat capacity. Between the two diluents, the effect was larger in the case of the CO_2 diluent due to its dissociation during combustion as well as its greater heat capacity. Burbano *et al*. observed flame instabilities at lean conditions and that H_2 has the tendency to destabilize the flame. On the other hand, CO has a stabilizing effect on the flame by decreasing hydrodynamic and thermal-diffusive instabilities. In the end, the destabilizing effect of H_2 is more dominant. When either of the two diluents is added to the mixture, instabilities were observed over a wider range of equivalence ratios, although stable flames are more likely to be obtained at rich equivalent ratios.

1.4.3 Biogas with CO_2 Dilution

An experimental study conducted by Cohe *et al*. (2009) investigated laminar and turbulent lean premixed CH_4/CO_2/air flames at various pressures using Bunsen flame. The investigation involved the analysis of flame propagation speed, flame surface density as well as wrinkling parameters of the flame front. The experimental data and PREMIX computations both revealed that CO_2 addition decreases the laminar flame speed.

1.5 Conclusion

The summary of previous works reveals how little research has been conducted into the flame structure of syngas and biogas structures with CO_2 dilution, particularly involving Raman scattering laser diagnostic techniques. Nonetheless, important material can be derived from the literature review. In summary, Raman spectroscopy can successfully be used to unobtrusively measure local properties in stationary flames. Although experimental results for the desired fuels do not exist in the literature, it was illustrated with similar mixtures that the reaction boundary of a laminar, premixed flame can be identified by a decrease in the unburned reactant concentrations as well as an increase in CO_2 and H_2O concentrations. Furthermore, the reaction boundary is characterized by the diffusion of ambient air into the flame, resulting in an increase of O_2 and N_2 concentrations. This also coincides with a decrease in flame temperature to room temperature. In H_2/CO flames, the radial position of the maximum temperature coincides with the maximum concentrations of H_2O and CO_2. The addition of H_2 generates an increase in flame temperature and it also increases the laminar burning velocity of the mixture due to chemical effects as opposed to thermal effects. On the other hand, the addition of CO lowers the flame temperature due to increased production of CO_2, which increases the radiative heat loss. This also has the effect of lowering the mixture's laminar burning velocity.

The main objective of this study is to measure the flame temperature and the concentration of the major species (H_2, CO, CH_4, H_2O, CO_2, O_2, N_2) via laser diagnostics for various syngas and biogas flames with CO_2 dilution. In addition to this main objective are the following sub-objectives:

1. Measure each mixture's visible flame height;
2. Qualitatively describe the characteristics of the each mixture's visible flame;
3. Study the effects of H_2/CO ratio on flame structure for the CO_2-diluted syngas and biogas mixtures;
4. Study the influence of CO_2 addition on flame structure for syngas and biogas mixtures.

This project is being conducted with an industrial partner and the results will permit the validation of chemical kinetics in computational fluid dynamics applications. The unique list of fuels to be tested has been predetermined by Rolls Royce Canada and there is no existing experimental data available in the literature for these mixtures. Furthermore, there is scarcely any data concerning flame temperature and major species concentration for partially premixed syngas flames. In order to study the effects of H_2/CO ratio or CO_2 addition on flame structure, experimental data from this study will need to be cross-compared between fuels to establish trends whenever a unique variable can properly parametrized. Thus, the experimental data should successfully allow for the characterization of each test fuel's flame structure as well as establish the possible effects H_2/CO ratio and CO_2 addition on these flames.

The following chapter will discuss the experimental setup used in this study. The methods and techniques will be introduced along with the descriptions of the mixtures, equipment and target conditions.

CHAPTER 2

EXPERIMENTAL APPROACH

This chapter introduces the experimental approach used in measuring the laminar partially premixed flame characteristics. This includes the experimental setups used to measure flame length, species concentration and flame temperature measurements. The investigation of laminar flame speed was removed from the project's scope.

2.1 Experimental Setup

Species concentrations and temperature are measured at pre-determined test heights. These test heights, represented by $\frac{z}{H_T}$, are calculated as 10%, 20%, 40% and 60% of the given flame's length. Therefore an accurate measurement of flame length is required for each of the ten flames. Next, at each specified test height, Raman spectroscopy is used to measure species concentrations. Temperature measurements are recorded separately since they require a different measurement technique. For simplicity, $\frac{z}{H_T}$ may be referred to plainly as z*.

Table 2.1 Compositions of mixtures

Mixture	CO (% Vol)	H_2 (% Vol)	CH_4 (% Vol)	CO_2 (% Vol)	H_2/CO Ratio
B1	0	0	60	40	-
S1	50	25	0	25	0.5
S2	37.5	37.5	0	25	1
S3	25	50	0	25	2
S4	50	25	5	20	0.5
S5	37.5	37.5	5	20	1
S6	25	50	5	20	2
S14	42.5	42.5	0	15	1
S5M50	18.75	18.75	52.5	10	1
S5M25	28.125	28.125	28.75	15	1

Table 2.1 presents the compositions of the ten gaseous mixtures under investigation. The fuel compositions were predetermined by the industrial partner. There is no available literature data with which to compare the results for the ten gaseous mixtures. Therefore, in order to validate the experimental method, a CH_4/air flame is measured first since there is existing literature data with which it can be compared.

The experimental setup is centered around the 10 Hz Spectra-Physics Nd:YAG laser. This laser generates the 1064 nm laser beam, which emits UV light of 266 nm, which passes through the electric LaVision shutter. The shutter serves to interrupt the laser beam's passage to the polarizer, also provided by LaVision. Polarization is an optical technique necessary to the experimental methodology due to its ability to alter the intensity of the laser beam. The polarizer is thus responsible for managing the beam into weak intensity (polarization P) and high intensity (polarization S). A two-mirror arrangement redirects the beam to a higher elevation more conducive to taking measurements. As the beam emerges from the optical arrangement, it passes through a 50.8 mm diameter lens which concentrates the 10 mm diameter beam into roughly 1 mm diameter. This concentrated beam passes over the burner through the center of the flame under examination. The burner sits on a stand of adjustable height, making it easy to take measurements at all necessary test heights.

Since the gaseous fuels do not come pre-prepared, they are mixed from their separated components. Five high pressure cylinders each contain one of H_2, CO, CH_4, CO_2 and air, all in their gaseous states. Silicon tubes carry the required gases from their cylinders to controlled Omega FMA5423 flow meters. A Labview program provides the control of the flow meters, regulating the flow of each gas in order to provide the desired percentages of each gas as well as the required equivalence ratio. Upon exiting the flowmeters, silicon tubes are branch connected so that the gases are mixed in line. To ensure an adequate level of mixing, the in-line mixing zone length exceeds 150 times the diameter of the burner as with Hariharan *et al*. (2007).

The 3.175 mm inner-diameter burner, depicted in Figure 2.1, is used in this experiment since it is readily available and ideally sized for producing laminar flames close to the desired equivalence ratio of 3. In order to prevent flashback, the 3.175 mm I.D. channel reduces to 1 mm I.D. in order to extinguish any potential return of the flame into the equipment. With a total length of 18.75 cm, the ratio of burner length to diameter exceeds 50, as recommended by Natarajan *et al*. (2007). This ensures a fully developed laminar exit flow. For instances in which a flame cannot be achieved, the 3.175 mm can be substituted for a 10 mm burner which is also available in the lab.

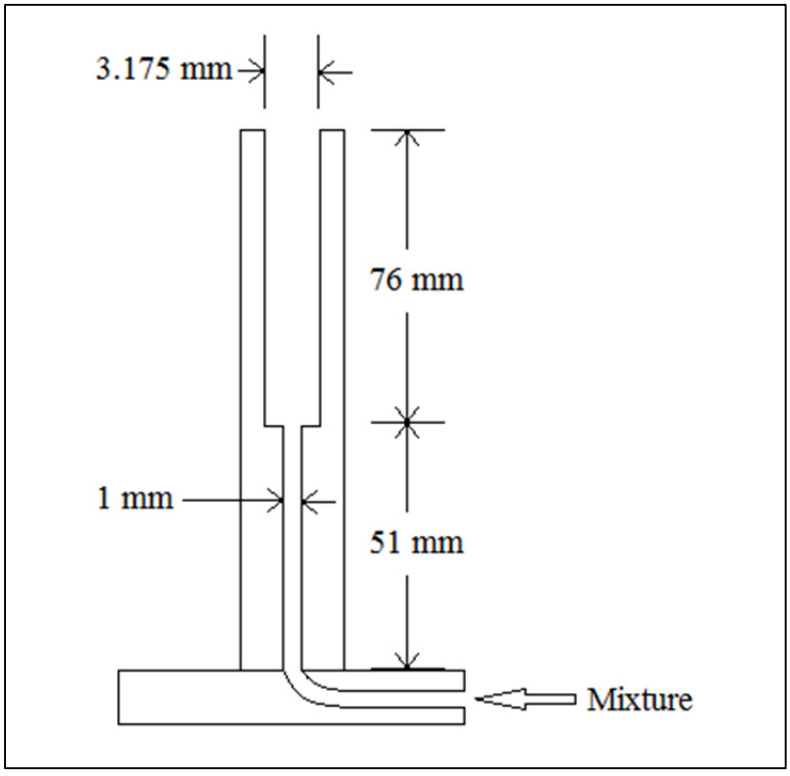

Figure 2.1 Dimensions of 3.175 mm inner diameter burner

Table 2.2 summarizes the target operating conditions for this experiment where the ambient temperature and pressure correspond to the room conditions in the lab. The target equivalence ratio has been set at 3 in order to correspond to the average equivalence ratio of annular gas turbine combustors. Mohammad *et al*. (2010) shows the local equivalence ratio imposed on flow field velocity vectors. The results give insight into the stability

characteristics of the gas turbine combustion system and thereby validate the equivalence ratio used in this study. The Reynolds number of 1 400 is a target value which corresponds to the general industry norm, falling well within the laminar regime.

Table 2.2 Target Operating Conditions

Ambient Temperature	295 K
Ambient Pressure	1 atm
Equivalence Ratio	3.0
Reynolds Number	1 400

2.2 Flame Length

The measurement of visible flame length (also called flame height) involves filming of the steadied flame with a digital camera. In this case, a Canon PowerShot A430 records a video of the flame in a darkened room with still air and the data is transferred to computer. Using the GIMP graphics editing software, the dimension tool allows the measurement in number of pixels of the visible flame as well as the measurement of a reference length (in this case, the burner height). Knowing the true length of the burner, a simple cross multiplication of these three variables yields the visible flame length.

An averaging technique is used to attain the most accurate measurement of flame height as possible. A video of each flame is divided into a series of images at equally spaced time intervals by using the VirtualDub software. The flame length is measured in a selection of 30 images for each flame and then averaged to produce the final result. Lyle *et al*. (1999) concluded (using methane-air flames) that 30 images is an adequate number over which to take the average. It was demonstrated that the average flame height did not change more than 5% when more than 30 images were used.

Since the B1 and S5M25 did not ignite with the 3.175 mm burner, the 10 mm burner is used for these two fuels. The S4 fuel did not ignite with the 3.175 mm and continuous flame

reattachment (see Section 1.1.4) was experienced on the 10 mm burner. The S4 fuel was dropped from the study since all stabilization attempts were not successful. Table 2.3 summarizes the operating conditions and flame height established for each mixture's flame. Some flexibility was permitted on the equivalence ratio and Reynolds number values in order to accommodate the flowmeters' inability to regulate the lower ranges of the H_2 and CH_4 flow requirements (for the S1, S4, S5, S6 and S5M50 fuels in particular).

Table 2.3 Summary of operating conditions and flame height for each gaseous mixture

	Burner	**Fuel**		**Visible Flame**	
Mixture	**Diameter [mm]**	**φ**	**Re**	**Length [cm]**	**Std Dev [cm]**
B1	10	3.12	1144	7.23	0.81
S1	3.175	3.28	1753	5.75	0.21
S2	3.175	3.38	1671	5.43	0.19
S3	3.175	3.44	1590	5.08	0.20
S5	3.175	3.41	1566	5.52	0.24
S6	3.175	3.26	1535	4.86	0.17
S14	3.175	3.42	1574	6.17	0.31
S5M50	10	3.17	1059	12.4	0.92
S5M25	3.175	3.37	1533	4.32	0.19

2.3 Species Concentration

This section of the study examines flame species concentrations using Raman spectroscopy (described in Section 1.2.1). With this methodology, the test flame is illuminated with the laser beam and light from the illuminated point is collected with lenses and concentrated into the SpectraPro 2300i spectrograph from Acton Research. The wavelengths from the elastic Rayleigh scattering are filtered out by a filter installed in front of the lenses. The SpectraPro is centered at 280 nm which permits the measurement of important species (O_2, N_2, H_2, H_20, CO and CO_2). The experimental setup is displayed in Figure 2.2.

At each polarisation angle, 700 photos are captured at a 10 Hz frequency using a LaVision camera (1 376 x 1 040 pixels where each pixel measures 6.45 x 6.45 µm) connected to a signal intensifier. An averaging technique is used to yield a sing image from the 700 photos.

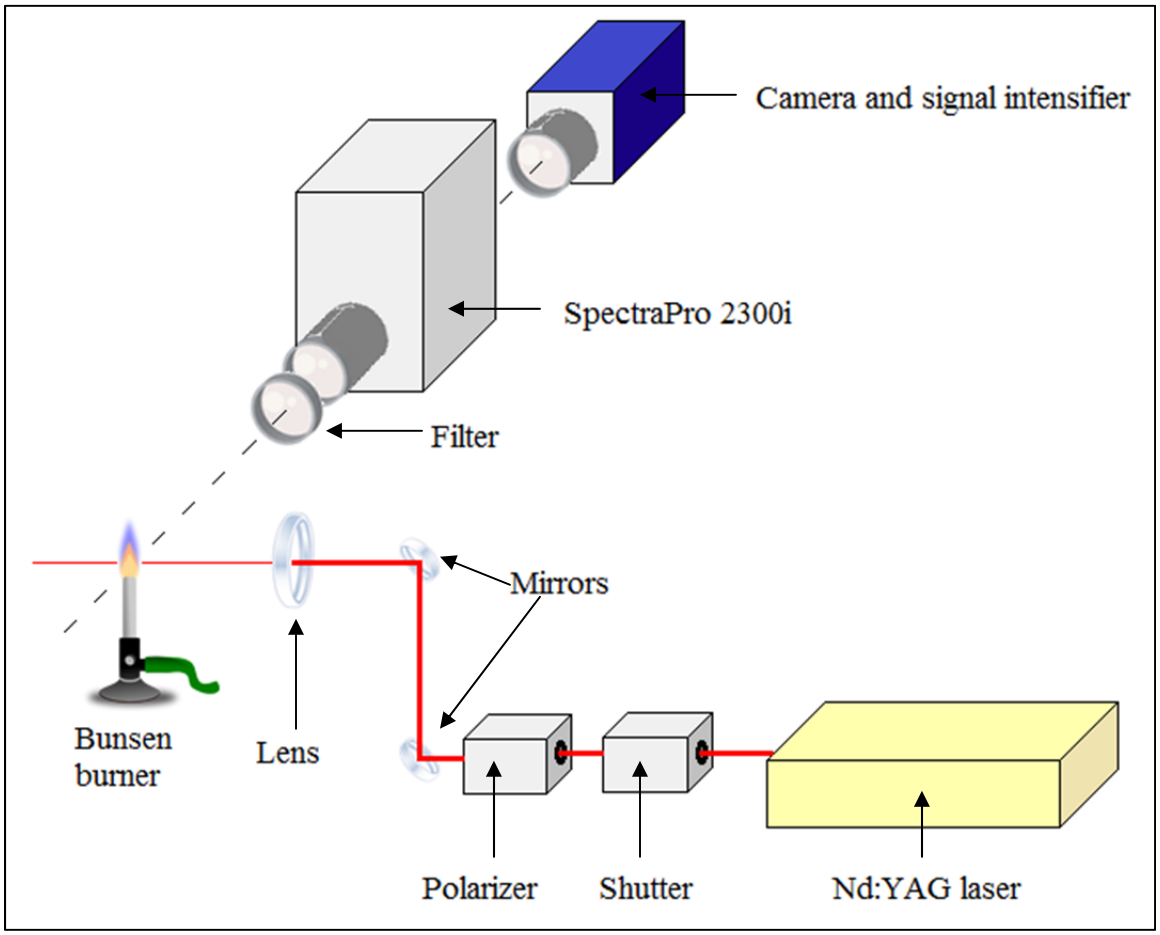

Figure 2.2 Experimental setup for the measurement of species concentration

The S and P polarisation angles represent the two light intensity directions emitted by the photons once a molecule is excited by the laser. The S angle corresponds to the vertical direction with respect to the scattering plane and it also coincides with the maximum light intensity emission. Conversely, horizontal polarisation angle P, which is parallel to the scattering plane, corresponds to the minimum light intensity emission. Hayashida *et al.* (2006) used a polariser in order to polarise the laser beam according to the polarisation angle. As a result, the Raman spectrum can be obtained by separating the Raman scattering

(Polarisation S) from the emission background noise (Polarisation P). The species concentrations can then be calculated based on the difference between S and P.

Since this study follows that of Ouimette, the S and P polarisation angles have already been established. The S and P angles were determined by measuring the intensity between 0 and 360 degrees in 10-degree intervals with no test flame (laser passing through ambient air). The maximum registered intensity corresponds to the S polarisation and the P polarisation corresponds to the minimum intensity.

2.4 Flame Temperature

The flame temperature measurement follows a similar experimental arrangement with slight modifications to that seen in Figure 2.2. The Rayleigh filter has been removed and the polarisation angle has been set to 250 degrees in order to increase the intensity of the laser passing through the flame. In an effort to eliminate chemoluminescence, the opening period of the intensifier has been reduced to its minimum possible value of 210 ns as seen in Lafay *et al*. (2008). The measurement technique involves setting the burner to the appropriate test height and then generating three separate images, each of which represent one of the following: one image of the background noise with no laser, one reference image of the laser in ambient air, and one image of the laser flame measurement. Each image is created by using an averaging technique similar to that of Section 2.3, however only 200 images are averaged in this portion of the experiment as recommended by Lafay *et al*. (2008). Ouimette (2012) explored the effects of increasing the number of averaged images to 700, however there was no increase in precision generated from this adjustment.

In order to obtain a useable reference and flame image, the background noise image is subtracted from the reference and flame images. Subsequently, the new reference image is subtracted from the new flame image in order to obtain useable flame intensity data. From this data, the flame temperature can be calculated using the Equations (2.1) and (2.2) in Lafay *et al*. (2008):

$$T(r,z) = T_0(r,z)\frac{I_0(r,z)}{I(r,z)}\sigma_{R_N} \quad (2.1)$$

$$\sigma_{R_N} = \frac{\Sigma_j X_j(r,z)\sigma_j}{\Sigma_i X_i(r,z)\sigma_i} \quad (2.2)$$

The temperature in degrees K is represented by $T(r,z)$ and the intensity of the Rayleigh signal is represented by $I(r,z)$. The χ value is the molar fraction of a given species and σ_R is the Rayleigh scattering cross section in m^2, whereas the normalized Rayleigh scattering cross section is represented by σ_{R_N}. In order to differentiate between the property of a given species in ambient air as opposed to its flame property, the subscripts *i* and *j* are used (the *i* subscript being the ambient air indicator and the *j* subscript being the flame indicator). Furthermore, the subscript *0* is used to indicate when temperature and intensity correspond to their ambient air values. The absence of subscript *0* for $T(r,z)$ and $I(r,z)$ indicates that they are flame measurements of temperature and intensity respectively.

Each test height corresponds to a fixed value of z^*, which specifically is equivalent to 10%, 20%, 40% or 60% of the visible flame length for each fuel. At a specified, constant value of z^*, spectroscopy measurements return values of species concentration along the flame's radius *r*. These values of species concentration correspond to the molar fraction χ_j, which is required to calculate the normalized Rayleigh scattering cross section in Equation (2.2). According to Lafay *et al*. (2008), σ_{R_N} depends on gas composition; however it can be assumed as independent of temperature. There exists published relative differential Rayleigh scattering cross sections, measured relative to nitrogen at 295 K, which allows for σ_N to be calculated according to Sutton and Driscoll (2004). The following table contains the relative cross sections for the species of interest:

Table 2.4 Relative cross sections of main species

Species	Relative Rayleigh Scattering Cross Section
N_2	1.00
O_2	0.97
H_2	0.24
CO	1.36
H_2O	0.86
CH_4	2.28
CO_2	2.50

2.5 Experimental Uncertainty

There is an overall uncertainty associated to each single experimental measurement and these uncertainties are used to calculate the overall uncertainty. Ouimette (2012) employs a technique from Moffat (1988) that makes it possible to quantifiably describe a system's overall uncertainty. This approach describes the quality of the experiment much better than merely reporting the precision of each measurement. The objective of this section is to determine the overall uncertainty of the experimental measurements and results. This will establish the uncertainty associated with the flame length, equivalence ratio, and flame temperature of each mixture.

2.5.1 Overall Uncertainty of a Single Measurement

From Moffat (1988), for a variable, X, the overall uncertainty of a single measurement, $U_{0.95}$, can be calculated using Equation (2.3):

$$U_{0.95} = \left\{ \left(B_{X_i}\right)^2 + \left(t_{v,0.95} S_{\bar{X}_i}\right)^2 \right\}^{1/2} \qquad (2.3)$$

The symbol t_v represents the Student's *t* multiplier for *v* degrees of freedoms. For 95% confidence, $t_{v,0.95}$ can be looked up in any T-distribution table or graph found in most statistics textbooks. The overall bias limit of the measurement, B_{X_i}, and the precision index, $S_{\bar{X}_i}$, can be calculated from Equation (2.4) and Equation (2.5) respectfully.

$$B_{X_i} = \left[\sum_{i=1}^{M} {B_i}^2\right]^{1/2} \quad (2.4)$$

$$S_{\bar{X}_i} = \frac{\sigma}{\sqrt{N_T}} \quad (2.5)$$

From Equation (2.4), it is shown that $B_{X_i}$is the root-sum-square combination of the fixed error components, B_i. In Equation (2.5), σ represents the standard deviation as measured during the experimental measurements whereas N_T corresponds to the number of performed measurements. The values of B_i for this project's experimental measurements are outlined in Table 2.5 along with the overall bias limit of the measurement. Table 2.6 summarizes the overall measurement uncertainty for the flame height and equivalence ratio of each measurement.

Table 2.5 Summary of the overall bias limits and
fixed error components for each measurement instrument

Measurement	**Instrument**	**Source of Uncertainty**		$\boldsymbol{B_{X_i}}$
Equivalence Ratio	Flowmeter	Precision	± 1.5% full scale	1.6%
		Repeatability	± 0.5% full scale	
Flame Height	Ruler	Precision	0.1 cm	0.12 cm
	Camera	Pixel size	0.07 cm	

Table 2.6 Estimation of the overall measurement uncertainties
for each mixture's flame height and equivalence ratio

Mixture	Flame Length (cm)	Uncertainty (%)	Equivalence Ratio	Uncertainty (%)
B1	7.23	5.49	3.12	4.18
S1	5.75	3.81	3.28	4.01
S2	5.43	3.73	3.38	3.91
S3	5.08	4.86	3.44	3.85
S5	5.52	3.71	3.41	3.89
S6	4.86	4.95	3.26	4.03
S14	6.17	2.53	3.42	3.87
S5M50	12.4	5.02	3.17	4.13
S5M25	4.3	3.22	3.37	3.92

2.5.2 Overall Uncertainty of the Experimental Results

At this stage, the uncertainties calculated in section 2.5.1 can be combined to calculate the overall uncertainty of the experimental results. Ouimette (2012) uses a method from Lee (2008) of calculating the overall uncertainty of the experimental results, which is summarized by Equation (2.6):

$$\left(U_y\right)_{max} = \sqrt{\sum_{i=1}^{n}\left(\frac{df_1}{dx_i}U_i\right)^2} \qquad (2.6)$$

The symbol $\left(U_y\right)_{max}$ denotes the final overall uncertainty of the variable y, where y is calculated by a function, f_1, of a measured variable, x_i. The partial derivative of function f1 can be closely approximated through a simple spreadsheet calculation in which a delta is incorporated into a fundamental principle of calculus. From Stewart (1991), Equation (2.7) states:

$$\frac{df_1}{dx_i} = \frac{f_1 x_2 - f_1 x_1}{x_2 - x_1} \quad (2.7)$$

Following the same procedure as Ouimette (2012), $x_2 = x_1 + 0.0000001$ and x_1 represents the known variable and the delta is equal to 0.0000001. Essentially, the partial derivative is calculated by substitution over an infinitesimally small change in the measured variable x_i. This method avoids the need to solve complicated equations. A summary of the calculated uncertainty results can be seen in Table 2.7 while the uncertainty associated to each measurement can be found in APPENDIX II. The overall uncertainty associated with the calculated flame temperature is below 10%, which is the typical uncertainty for the Rayleigh method according to Ouimette (2011).

Table 2.7 Overall uncertainty of the calculated corrected temperature

	Temperature Uncertainty $(U_T)_{max}$	
Mixture	**Minumum**	**Maximum**
B1	2.75%	4.04%
S1	6.06%	7.51%
S2	6.10%	7.24%
S3	5.99%	7.12%
S5	6.65%	7.63%
S6	8.35%	9.14%
S14	4.26%	5.30%
S5M50	4.77%	5.35%
S5M25	8.33%	8.57%

CHAPTER 3

RESULTS AND DISCUSSION

The experimental results and discussion are provided in this section. Flame chemical structures for each fuel are represented graphically as functions of species concentration and flame temperature against flame radius at each of four test heights (z* values of 10%, 20%, 40% and 60%). Results are presented for the major species: H_2, CO, CO_2, N_2, O_2 and H_2O (as well as CH_4 for methane-containing fuels). The flame height measurements will be incorporated in this chapter, as will qualitative and quantitative observations for each flame. In order to facilitate the analysis, Table 3.1 and Table 3.2 have been included in this section in order to present, respectfully, the concentrations of major species exiting the burner rim and the concentrations of the products of combustion at stoichiometry. Where appropriate, measured data from several mixtures will be consolidated and compared in order to analyse the effects of CO_2 dilution or H_2/CO ratio.

Table 3.1 Theoretical species concentrations at burner exit with equivalence ratio of 3

Mixture	**CO (%vol)**	**H_2 (%vol)**	**CH_4 (%vol)**	**CO_2 (%vol)**	**N_2 (%vol)**	**O_2 (%vol)**
B1	0.00	0.00	20.66	13.77	51.79	13.77
S1	31.35	15.67	0.00	15.67	29.47	7.84
S2	23.51	23.51	0.00	15.67	29.47	7.84
S3	15.67	31.35	0.00	15.67	29.47	7.84
S5	21.38	21.38	2.85	11.40	33.95	9.03
S6	14.26	28.51	2.85	11.40	33.95	9.03
S14	25.38	25.38	0.00	8.96	31.81	8.46
S5M50	6.33	6.33	17.72	3.37	52.34	13.92
S5M25	11.92	11.92	12.19	6.36	45.50	12.10

Table 3.2 Stoichiometric products of combustion

Mixture	H_20 (%vol)	CO_2 (%vol)	N_2 (%vol)
B1	17.88	14.90	67.22
S1	10.37	31.12	58.51
S2	15.56	25.93	58.51
S3	20.75	20.75	58.51
S4	N/A	N/A	N/A
S5	16.46	21.66	61.88
S6	20.79	17.33	61.88
S14	16.36	22.13	61.51
S5M50	18.46	12.12	69.42
S5M25	17.86	14.99	67.15

3.1 Biofuel Mixture B1 – $60CH_4/40CO_2$

The B1 mixture is the only biofuel under examination in this study. The mixture is composed of CH_4 diluted with 40% volume of CO_2. Its composition differs more significantly from the other test fuels and therefore its behaviour cannot be directly compared to that of the other test fuels. The B1 results are, therefore, analysed on their own.

3.1.1 Qualitative Observations

Ignition difficulties were experienced when using the 3.175 mm burner. A sustained flame could be achieved only with the help of an external flame source, which resulted in a blue flame with a flame cone clearly visible above the burner exit. Since the flame could not be sustained, no measurements could be taken with this burner arrangement. Instead, the 10 mm burner was used and only then was a sustained flame achievable on its own. At a Reynolds Number of 1400, the flame was rather unstable as flicker was clearly evident. In an attempt to stabilize the flame for improved measurements, the Reynolds Number was reduced to 1000 in order to be even more on the laminar end of the spectrum. The stability of the flame improved slightly, although flicker was still present. The stability of the flame was

satisfactory closer to the burner exit, therefore measurements were taken only at 10% and 20% of the flame heights; measurements at 40% and 60% were unsatisfactory due to the effects of flicker.

Figure 3.1 Photograph of the B1 flame
at Re=1000 (B1: $60CH_4/40CO_2$)

As seen in Figure 3.1, the B1 flame is a blue flame with a high level of transparency. Under the given conditions, no flame cone could be distinguished. The flame itself is relatively conical in shape, with the widest part of the flame apparently located at the very base of the flame. The height and width of the flame fluctuated quite often and several measurements had to be taken due to the instability.

3.1.2 Quantitative Results and Analysis

The quantitative results provide insight only into the behaviour of the flame. Of note, the temperature remains close to ambient within 2 mm of the central axis of the flame. The weak temperature could be an indication that there has not yet been a sufficient level of premixing with ambient air. The temperature begins to increase towards the central axis as z/H_T increases to 20%, however the maximum temperature value has decreased. The early decrease in temperature could be caused by the production of CO_2, due to the reaction of

CH_4, which increases the radiation heat loss. The position of T_{max} has shifted slightly inwards in relation to the radial distance. At z*=10%, T_{max} is radially located at roughly 6 mm and decreases to roughly 5 mm at z*=20%. This indicates the width of the flame at each test height and supports the observation that the flame is conic and widest at its base.

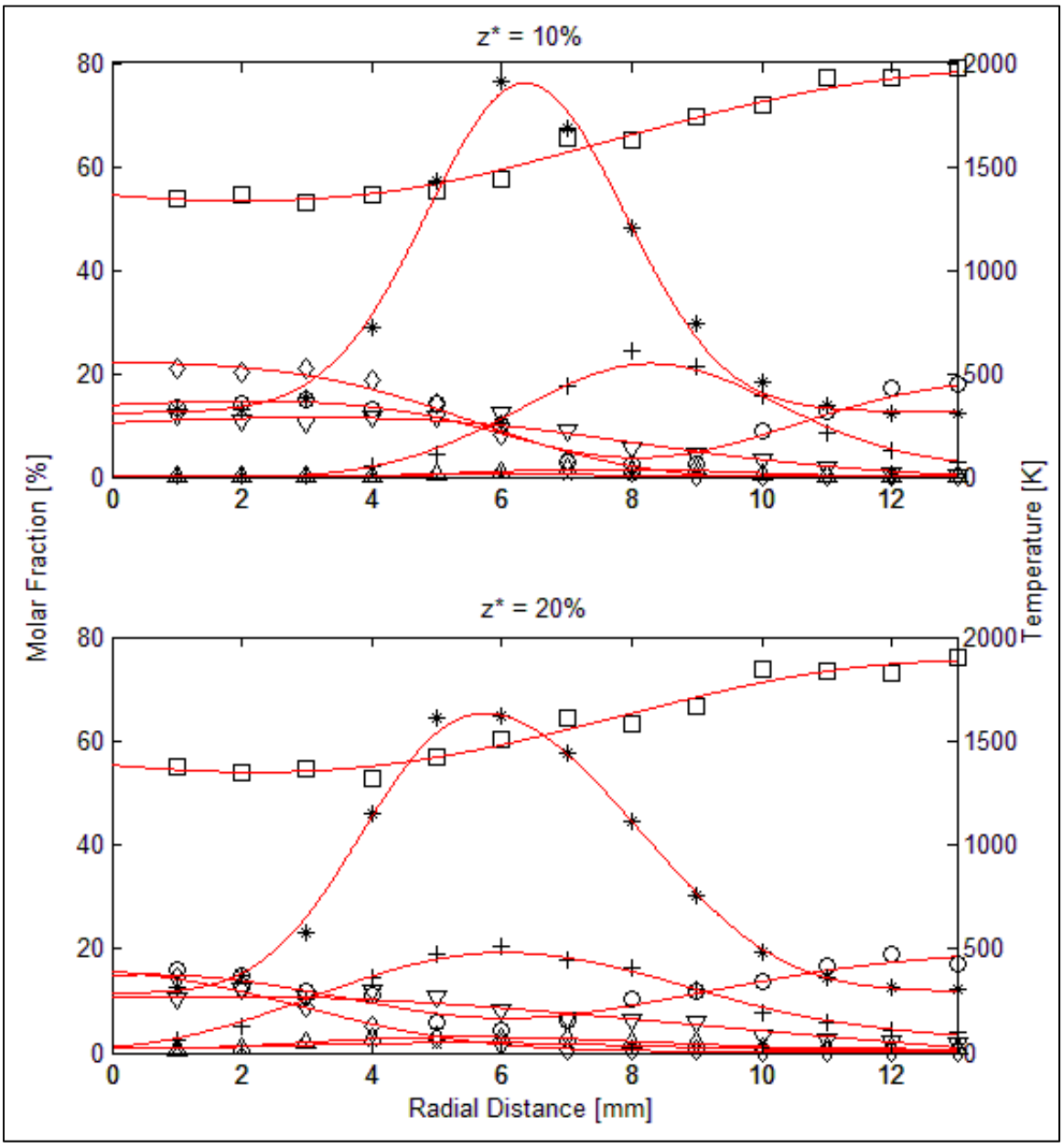

Figure 3.2 Radial profiles of temperature and species concentrations of the B1 flame at z*=10% and 20% (×=H_2, Δ=CO, +=H_2O, ∇=CO_2, □=N_2, ○=O_2, ∗=Temp)

The concentration of CH_4 decreases gradually in relation to the radial distance from the flame's central axis. At the higher z* elevation, the CH_4 concentration decreases at a faster rate. At both measurement heights, the concentration of CH_4 reaches a value close to zero at the same approximate location where H_2O reaches its maximum value and O_2 reaches its minimum value. This is a good indication that the CH_4 has been entirely consumed in the radial direction and stoichiometry has been achieved. Along the flame's central axis, the measured concentration of CH_4 has decreased from roughly 22% to 15% as z* increased from 10% to 20%. This suggests that there is a fair amount of CH_4 which has yet to react or dissociate.

Along the central axis, the concentration of CO_2 is lower than its stoichiometric for both measurement heights, meaning the maximum concentration level has likely not yet been achieved. The maximum CO_2 level must be achieved at a higher measurement height, presumably when more CH_4 has reacted.

3.2 Synthesis Gas with CO_2 Dilution

The S1, S2 and S3 syngas mixtures are each composed of H_2, CO and CO_2. They each contain equivalent concentrations of diluent, specifically 25% of CO_2. Since they contain no CH_4 and only the concentrations of H_2 and CO differ between the three syngas mixtures, it is particularly favourable for investigating the effects of H_2/CO ratio on syngas flames with 25% CO_2 diluent.

The S14 synthesis gas mixture contains a H_2/CO ratio of 1 with 15% CO_2 diluent. Since the S2 fuel also has an H_2/CO ratio of 1, their results can be compared along with results from Ouimette (2012) to investigate the effects of CO_2 dilution. Results from Ouimette (2012) are from equimolar H_2/CO flames. These results were selected due to the identical operating conditions in both studies as well as the similarites in the experimental approach, setup and equipment.

3.2.1 Qualitative Observations

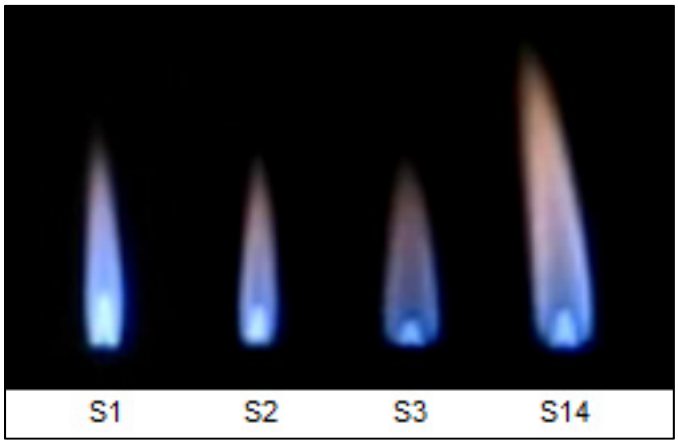

Figure 3.3 Photograph of H_2/CO syngas flames with CO_2 dilution

S1 – 50CO/25H_2/25CO_2

The S1 mixture experienced some ignition difficulties but was still able on occasion to achieve a sustained flame for several minutes with the 3.175 mm burner. The flame would regularly blow off when the hydrogen flow was either too low or fluctuated too much. In order to achieve ignition, the hydrogen flow was increased to beyond the required level. After ignition, the hydrogen flow was decreased to match the target hydrogen concentration for the S2 mixture. The flame stabilized often enough to successfully take measurements at the target operating conditions.

Visually, the S1 flame is distinguished by a light blue colour which fades to light orange at its apex. The flame cone is clearly visible at the burner exit with a distinctively triangular shape. The peak of the flame cone is very slightly rounded. The S1 flame burns rather bright, emitting more white light than the other fuels under investigation in this section.

S2 – 37.5CO/37.5H_2/25CO_2

The S2 flame is predominantly blue and assumes an orange colour towards the tip of the flame. It does not emit as much light as the S1 flame. The flame is noticeably shorter than the

S1 flame and appears to be of a slightly deeper blue, although more transparent. The S2 flame cone also appears to be visibly shorter than that of S1.

S3 – 25CO/50H_2/25CO_2

The S3 flame is very similar to S1 and S2 in reference to its colour, although S3 has an evidently higher level of transparency. The majority of the flame is a deep blue whereas the flame tip gradually assumes an orange tint. The flame cone is very obviously smaller than that of the other fuels, at just a fraction of their size. However the width of the flame appears visibly larger than that of the S1 and S2 flames as seen in Figure 3.3.

At times, it appeared the S3 flame was unstable. The instability arose due to the flowmeter's difficulty in regulating the very minuscule hydrogen molecules. Measurements were therefore taken after letting the flame burn for at least two minutes in order to allow the flowmeter to regulate the hydrogen flow.

S14 – 42.5CO/42.5H_2/15CO_2

Visually, the S14 flame has a noticeably higher flame length than the other fuels of section 3.2 and appears to be roughly the same width as the S3 flame. The relatively small flame cone is clearly visible to the naked eye and an orange tint is evident over a large portion of the flame's upper half in particular. The lower region of the flame is deep blue, surrounding the bright flame cone which shines a light blue. The transparency of the flame appears similar to that of the S2 fuel.

The greater flame height likely made the S14 flame more vulnerable to drafts of air as it was quite difficult to steady the flame in a vertical position. The S14 flame appeared otherwise quite stable and there were no problems with ignition. There appeared to be some fluctuation in the flowmeter's regulation of the hydrogen, but this fluctuation did not have a discernible effect on the flame's behaviour.

3.2.2 Quantitative Results and Analysis

3.2.2.1 The Effects of H_2/CO Ratio on Flame Structure

The effects of H_2/CO ratio on flame structure are illustrated in Figure 3.4 and Figure 3.5, which highlight the flame temperature and concentrations of main species (H_2, CO, CO_2, H_2O, O_2 and N_2) respectfully. This section studies partially premixed flames of syngas mixtures of varying H_2/CO ratio (0.5, 1 and 2) and 25% CO_2 dilution.

From Ouimette (2012), it is established that flame temperatures of H_2/CO mixtures will decrease in conjunction with CO addition. This is worthy of explanation because CO has the higher adiabatic flame temperature of the two species at 2400 K, which is slightly higher than that of H_2 (2350 K). This decrease in flame temperature can be explained by an increased presence of CO_2 within the flame generated by the reaction of CO. This increase in CO in turn increases the heat losses due to radiation. In Figure 3.4, it is evident that the fuels under investigation support this observation. Measurements suggest that there are no significant changes in temperature profiles at heights greater than or equal to 40% of the flame heights. At 10% flame height, it is apparent that higher concentrations of CO can be linked to longer flame cones, which is visually represented by the sharp decreases in flame temperature along the central axis of the S2 and S3 flames. The z*=10% elevation thus lies within the height of the flame cone. This means that the measurements were taken within the cone and therefore reflect the nature of the unburned reactants at that elevation. Hydrogen rich fuels, such as S3, react faster due to hydrogen's elevated laminar burning velocity, thereby resulting in flame cones of shorter length. Ouimette (2012) supports this finding as it was observed that higher concentrations of CO result in longer flame cones due to the slower laminar burning velocity.

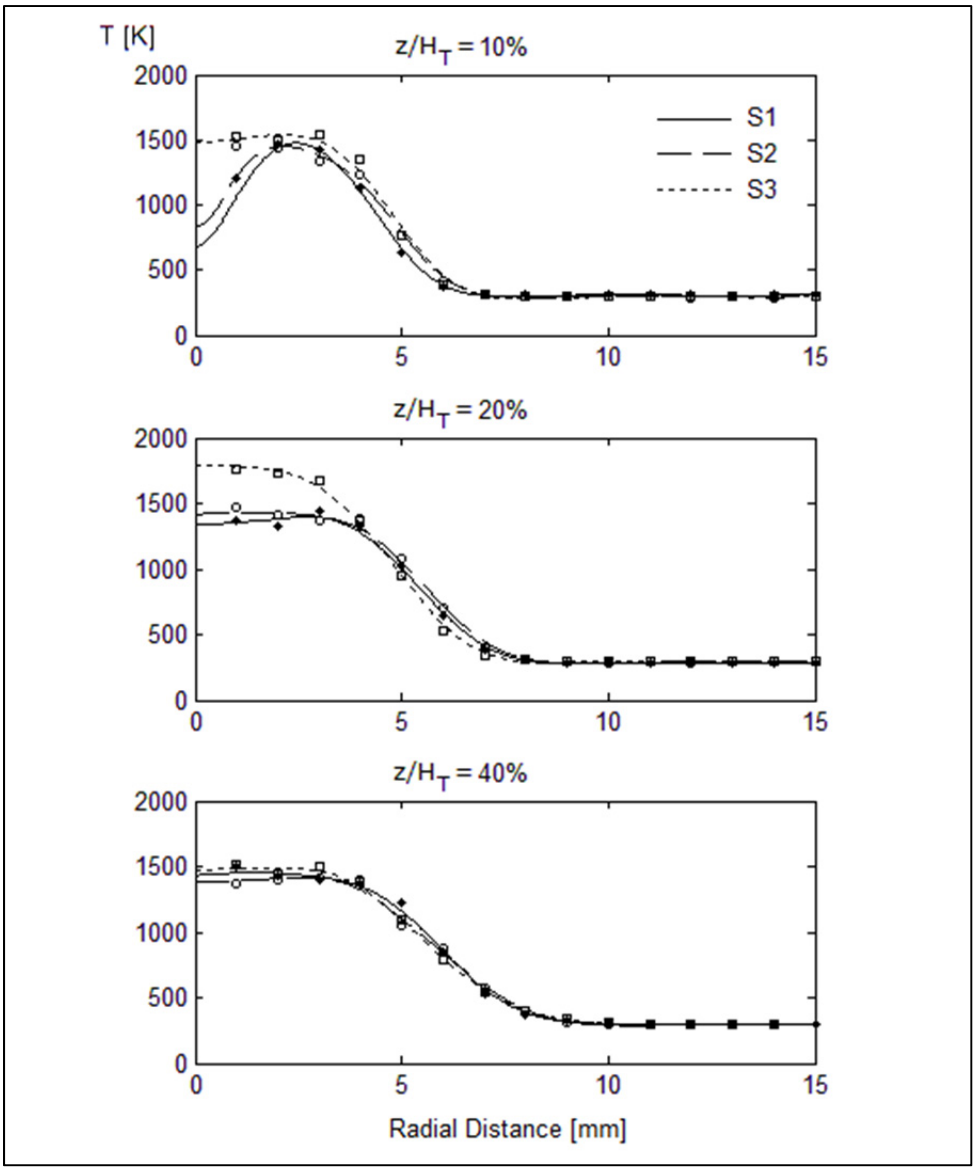

Figure 3.4 Temperature profiles of S1, S2 and S3 flames at various flame elevations (• = S1: $25H_2/50CO/25CO_2$, ○ = S2: $37.5H_2/37.5CO/25CO_2$, □ = S3: $50H_2/25CO/25CO_2$)

Figure 3.5 illustrates the variation in species concentration of all the major species in relation to the change in H_2/CO ratio. Data is plotted from measurements taken at z*=20%, as in Ouimette (2012), in order capture the state of the flame relatively early in the combustion process. The literature states that a decrease in H_2 concentration should be observed along the central axis as the H_2/CO ratio decreases. This notion is loosely supported by Figure 3.5,

although H_2 concentrations have already evened out amongst the three fuels at this elevation. It is made clear that, for each fuel, much of the H_2 reacts very quickly. Since only small amounts of H_2 remain, differences in H_2 levels between each fuel are less apparent. Figure 3.6 has been included to provide clarity to the H_2 concentration in the early stages of the flames.

The CO and H_2 graphs essentially offer an idea of how much of the fuel has already reacted at the specified elevation. Since it has been established that H_2 reacts quickly, it is expected to observe a corresponding early increase in H_2O along the central axis. Figure 3.5 suggests that mixtures higher in H_2 will experience higher levels of H_2O concentration about the flame's central axis. Furthermore, the experimental H_2O concentrations for each fuel are either equal to or slightly lower than their stoichiometric values. The S3 fuel's H_2O concentration is equivalent to the stoichiometric value, whereas S2 and S3 both indicate lower levels than stoichiometry. This likely means that the maximum H_2O concentration for S2 and S3 has not yet been reached.

An opposite trend is observed in conjunction with the increase in CO: Figure 3.5 indicates that increasing CO concentration within the fuel results in lower H_2O production and an increase in CO_2 production. For each fuel, the CO_2 concentrations along the flame's central axis register close to their stoichiometric values. Since the fuels are each equally diluted by CO_2, the effects of the CO_2 dilution are investigated later in this study using an approach more conducive to investigating the effects of CO_2 dilution (see Section 3.2.2.2).

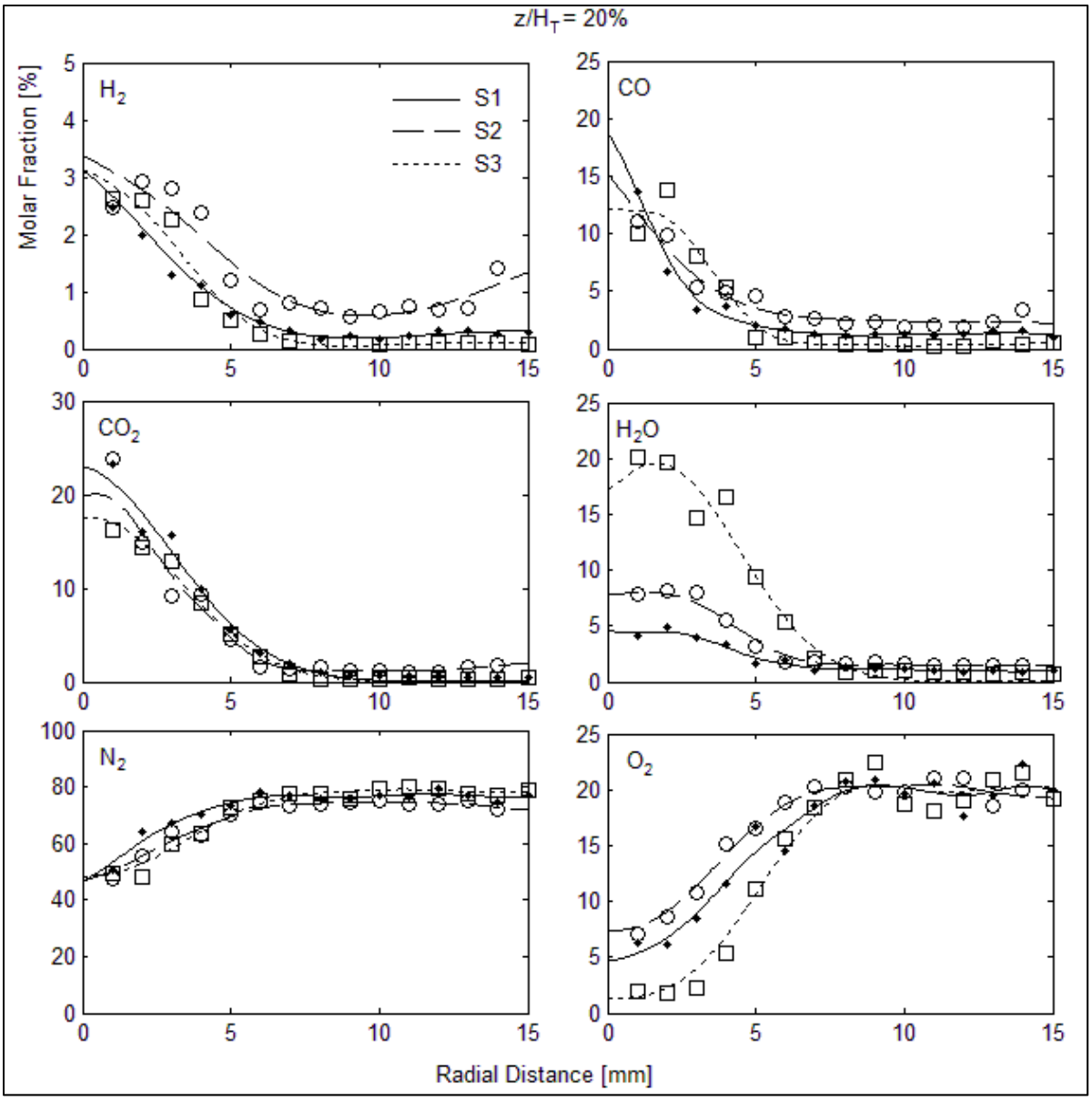

Figure 3.5 Radial profiles of species concentrations for S1, S2 and S3 fuels, measured at 20% of flame height (• = S1: $25H_2/50CO/25CO_2$, ○ = S2: $37.5H_2/37.5CO/25CO_2$, □ = S3: $50H_2/25CO/25CO_2$)

Figure 3.5 offers little evidence that H_2/CO ratio has an effect on N_2 and O_2 production. However, these two species indicate where the boundary between the fuel and the ambient air is located (in the radial direction). The proportions of the visible flames can thus be verified to a certain degree. In this case, both N_2 and O_2 return to ambient air values at the farthest radial distance from the flame's central axis. Thus, the observation that S3 is the

widest of the three flames is corroborated by the experimental data. When taking into account the experimental measurements from z*=60%, it also supports that S3 is the shortest of the three flames since the highest values of O_2 and N_2 along the central axis belong to the S3 fuel. This differs from the concept suggested in Ouimette (2012), where it was proposed that increases in a fuel's CO concentration resulted in a slight decrease in flame size due to the increased production of CO_2. However, this assertion from Ouimette pertains to H_2/CO mixtures without CO_2 dilution. Globally, Ouimette (2012) states that CO_2 dilution has a greater effect on flame height than the H_2/CO ratio and effects become apparent above equivalence ratios of 3. An experimental investigation into the effects of H_2/CO ratio under varying levels of CO_2 dilution could be of interest in the future.

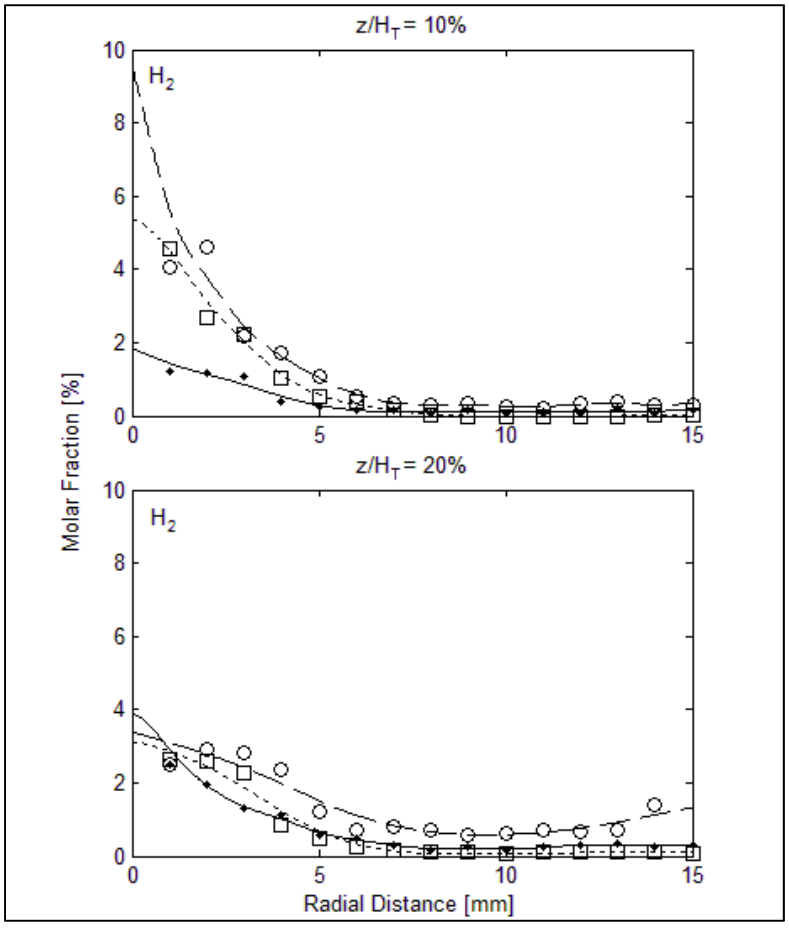

Figure 3.6 Radial profile of H_2 for S1, S2 and S3 fuels
(• = S1: $25H_2/50CO/25CO_2$, ○ = S2: $37.5H_2/37.5CO/25CO_2$,
□ = S3: $50H_2/25CO/25CO_2$)

3.2.2.2 Effects of CO_2 Dilution

The influence of CO_2 dilution on flame structure has not been widely studied, but useful information pertaining to this field can be extracted from the likes of Natarajan *et al*. (2007) and Burbano *et al*. (2011), both of whom studied laminar flame speeds of H_2/CO mixtures with CO_2 dilution using Bunsen burners. These works reveal that increases in CO_2 dilution significantly decrease the laminar burning velocities of these mixtures. Higher levels of CO_2 concentration within the fuel result in a decrease in heat release and an increase in heat capacity of the flame. The resulting decrease in temperature is associated with the reduction in the rates of reaction of H_2 and CO. The temperature profile in Figure 3.7 supports this assertion as it displays a decrease in central axis temperature in conjunction with increasing CO_2 concentration in the fuel. Furthermore, the temperature profiles over all of the measurement elevations suggest that an increase in CO_2 composition in the fuel results in a shorter, thinner flame. This is evidenced by the S2 flame's tendency to return to ambient temperature at the lowest elevation and nearest radial distance of the three samples. Further corroboration is available in Figure 3.7, where it is evident that fuels with higher CO_2 concentration produce O_2 profiles that return to ambient air values earlier along the radial axis, implying thinner flames. Burnabo *et al*. (2011) also reports an association between higher CO_2 concentrations and increased levels of flame instability over an increased range of equivalence ratios.

Natarajan *et al*. (2007) explains that the presence of CO_2 in the reactant fuel influences the flame chemistry and the radiative heat transfer. It absorbs radiative energy from the hot products and thereby affects the flame's behaviour. The CO_2 radial profile in Figure 3.7 provides further insight into the behaviour of CO_2 in the combustion process. According to the experimental results, it is shown that measured CO_2 quantities increases in accordance with increasing levels of CO_2 dilution along the central axis, as would be expected. However, the data suggests that the CO_2 levels decrease at a faster rate for fuels with higher CO_2 dilution. Furthermore, the equimolar H_2/CO mixtures with higher levels of dilution exhaust their CO_2 sooner than mixtures with lower dilution levels. Due to the lack of research in this

particular area, these assertions cannot be readily supported by outside literature, although it does provide more evidence that a higher concentration of CO_2 in the fuel results in thinner flame.

The H_2 and CO profiles give insight into the rates at which the fuels` combustible constituents are reacting. The CO curves present the most obvious indication of reaction trends, further supporting the notion that CO reaction rates decrease with increasing levels of CO_2 dilution. Along the central axis, CO concentration is higher for mixtures with more CO_2 dilution, as expected. Trends are not as easily identifiable from the H_2 radial profile, although it would appear that rates of H_2 reaction are slower for higher levels of CO_2 dilution.

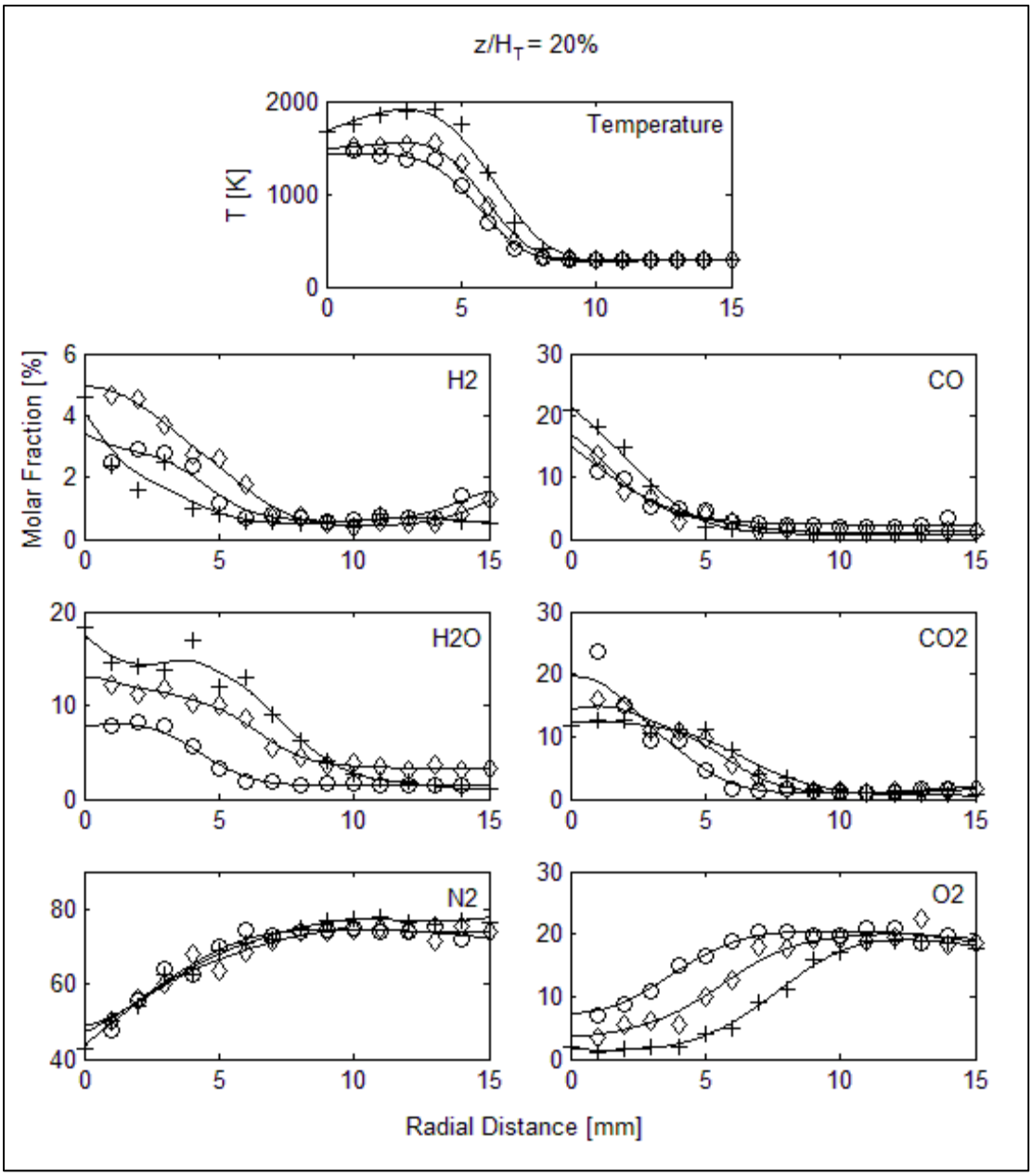

Figure 3.7 Comparison of species concentrations and temperature for S2, S14 fuels and experimental data from Ouimette (2012) measured at z/H_T=20% (○ = S2: $37.5H_2/37.5CO/25CO_2$, ◊ = S14: $42.5H_2/42.5CO/15CO_2$, + = Ouimette: $50H_2/50CO$)

3.3 Synthesis Gas with 5% CH_4 Addition and 20% CO_2 Dilution

The S4, S5 and S6 mixtures each contain 5% CH_4 and 20% CO_2 dilution in addition to varying concentrations of H_2 and CO. No data was obtained for the S4 mixture, therefore

only the S5 and S6 fuels could be used to investigate the flame structures of syngas flames with 5% CH_4 and 20% CO_2 dilution.

3.3.1 Qualitative Observations

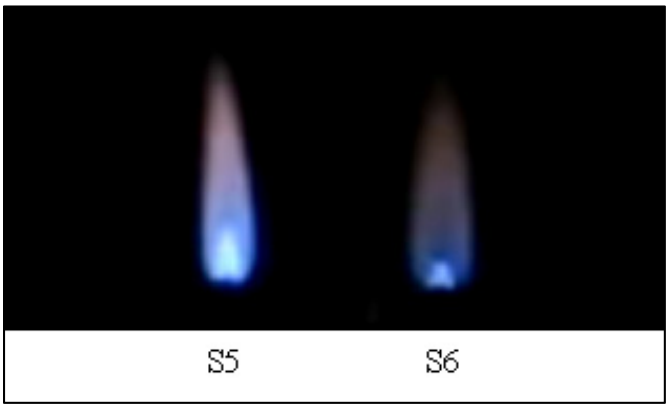

Figure 3.8 Photograph of syngas flames
with 5% CH_4 and 20% CO_2 dilution

S4 – 50CO/25H_2/5CH_4/20CO_2

The S4 syngas mixture failed to ignite with the 3.175 mm burner as well as the 10 mm burner. In order to achieve ignition, the Reynolds number was reduced to 1000 and again the mixture failed to ignite with the 3.175 burner. With the 10 mm burner, the reattachment phenomenon was experienced. Ignition was attempted with a 15 mm burner and reattachment was again observed. In the end, it was impossible to obtain any qualitative data for the S4 syngas mixture.

It is noteworthy that the S1 mixture, with a similar composition to S4, was capable of achieving ignition despite its higher concentration of CO_2. The H_2 and CO levels of concentration are identical between the two mixtures, meaning their H_2/CO ratios are equivalent.

S5 – 37.5CO/37.5H_2/5CH_4/20CO_2

There is no discernible difference in appearance between the S5 and S2 flames, meaning the 5% addition of CH_4 (and 5% reduction of CO_2 diluent) contributed very little to the flame's visual appearance and behaviour. Although there does appear to be a very slight reduction in size of the S5 flame cone when compared to the S2 flame cone, which suggests that the 5% increase in CH_4 has increased the burning velocity from that of S2. The degree of transparency appears to be equivalent to that of the S2 flame.

S6 – 25CO/50H_2/5CH_4/20CO_2

The difference in composition between S6 and S3 did not translate into any noticeable differences in flame appearance or behaviour between the two samples. The S6 flame exhibits the same blue colour with orange tint at the apex of the flame and a high degree of transparency as seen in Figure 3.8. The flame cone is also quite small and the dimensions of the flame appear quite similar to that of S3, with perhaps only a slight decrease in size in the S6 dimensions. Again, this makes sense since replacing 5% of an inert gas constituent with 5% of a combustible gas should increase the burning velocity of the mixture.

3.3.2 Quantitative Results and Analysis

The S5 and S6 fuels are similar in composition, differing only in H_2/CO ratio. Due to this similarity, the juxtaposition of the two fuels can provide some insight into the effects of H_2/CO ratio on the flame structure of such fuels. Figure 3.9 displays the radial profiles for temperature (K) and molar fraction of major species (% volume) at a measurement height of z*=20%. The temperature profile indicates that the S5 and S6 flames reach almost equivalent maximum temperatures, registering slightly under 2000 K. The S6 fuel, with the slightly higher maximum of 1994 K, reaches its peak temperature along the flame's central at z*=20%. On the other hand, the S5 fuel, which peaks closer to 1976 K, reaches its maximum temperature at a radial distance of approximately 2 to 3 mm. Moving inwards towards the center from $T_{max\text{-}S5}$, the temperature of the S5 flame lowers slightly to roughly 1863 K at the central axis. The low central axis temperature is even more apparent at z*=10%, where the

S5 central axis temperature is measured at approximately 467 K, whereas the S6 flame's temperature does not display a high variance between the central axis temperature and T_{max-S6}. In this case, since H_2 reacts first for both fuels, the difference in temperature at z*=10% can be explained by the higher amount of H_2 present in the S6 mixture. All this means is that, as seen in Ouimette (2012), a higher H_2/CO ratio results in a faster burning rate and therefore the S5 fuel produces a longer flame cone, which explains the lower central axis temperature at z*=10%. However, the distinction should be made clear that the higher level of H_2 coupled with the higher rate of reaction seen in the S6 mixture does not necessarily equate to a higher adiabatic flame temperature. As shown by Cheng *et al*. (2011), H_2 addition can increase the laminar flame speed of a H_2/CO/CH_4 mixture through chemical effects without necessarily increasing the adiabatic flame temperature. In regards to the oxidation of hydrogen, the H_2 radial profiles indicate that the majority of the species has reacted prior to reaching the z*=10% elevation, with only a molar fraction of roughly 4% in each flame. The concentration of H_2 continues to decrease thereafter in conjunction with increasing z*. The H_2O profile compliments the H_2 measurements at z*=10%. At this elevation, the concentration of H_2O has almost attained the stoichiometric value, with still some amounts of H_2 yet to react. The maximum concentration of H_2O is not located along the S5 flame's central axis, but rather at a radial distance of approximately 4 mm. Again, this is a strong indication that the z*=10% measurement intersects the S5 flame cone. The S6 flame displays very little discrepency between the maximum H_2O concentration (located at a radial distance of 3 mm) and the concentration along the central axis. So far, the S6 data suggests that the tip of the flame cone is located at or close to the z*=10% elevation. At z*=20%, the maximum concentration of H_2O is located along the central axis for both the S5 and S6 flames, as seen in Figure 3.9, which suggests that the flame cone is located entirely below this elevation.

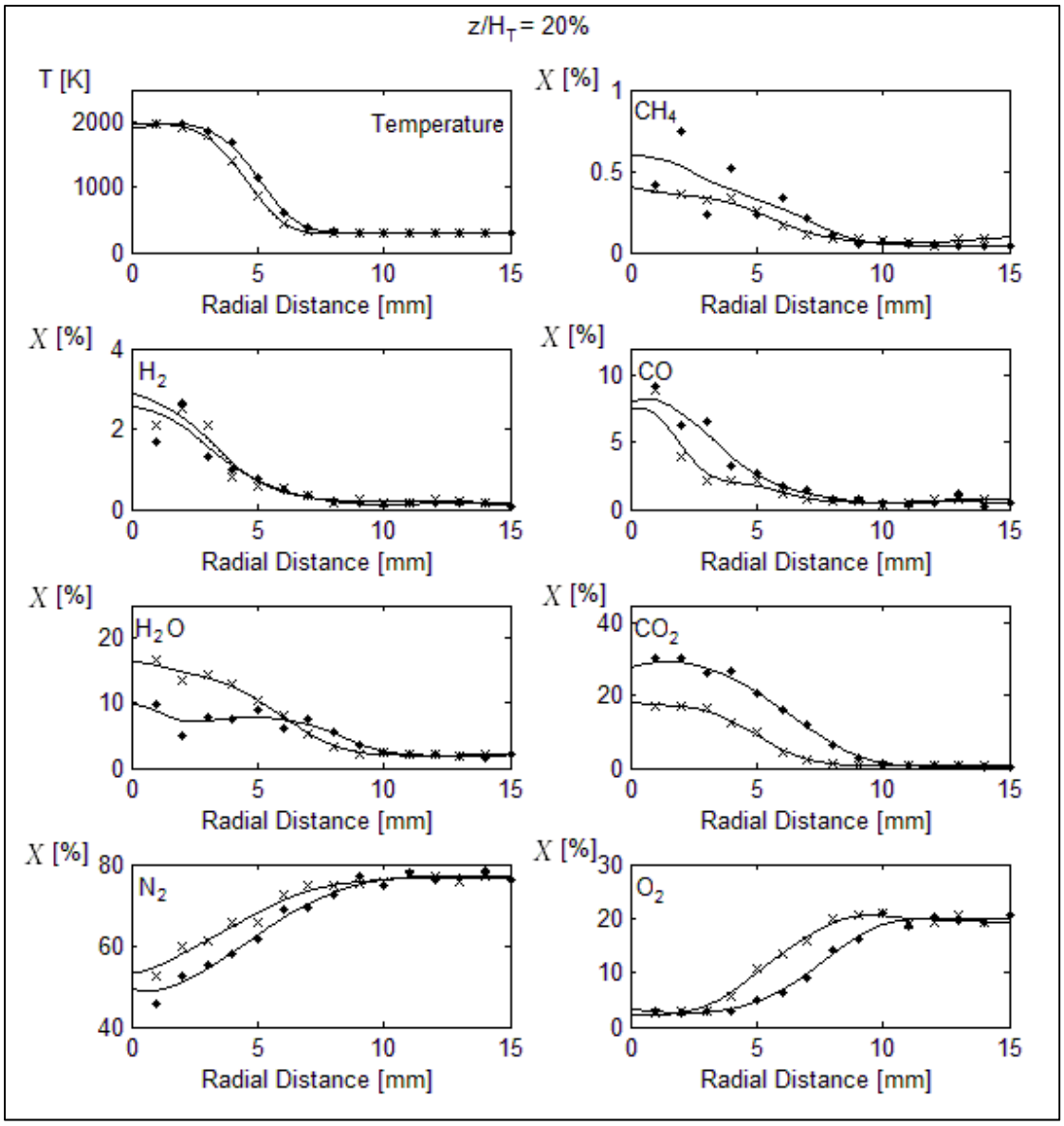

Figure 3.9 Comparison of species concentrations and temperature for S5 and S6 fuel measured at z/H_T=20% (• = S5: $37.5H_2/37.5CO/5CH_4/25CO_2$, × = S6: $50H_2/25CO/5CH_4/20CO_2$)

At z*=10%, the concentration of CO for both fuels suggests that there has not been significant oxidation of CO prior to this stage. The S5 flame registers a concentration of CO nearly equivalent to the initial concentration at the burner exit (19% at z*=10% compared to 21% at burner exit). On the other hand, although significant levels of CO remain for the S6 flame (9% compared to 14% at burner exit), the S6 flame appears to be further along in the

process of oxidizing CO. This makes sense when considering the faster burning rate of mixtures with higher H_2/CO ratios. At this stage, the combustion process has been dominated by the reaction of H_2 and the higher initial concentration of H2 for S6 evidently generates the faster burning rate. At this point, both fuels have experienced a similar level of CH_4 dissociation and/or oxidation so its effect will be discounted for now. However, by z*=20%, the divide in CO concentration has drastically reduced between the two flames, measuring approximately 8% and 7.5% for S5 and S6 respectively along the central axis. In other words, after nearly complete oxidation of H2, the S5 fuel burns its CO at an apparently faster rate than the S6 flame. Further illustrating this point is the amount of remaining CO at z*=60%: the S5 fuel registers less CO (approximately 1.5%) compared to the S6 fuel (approximately 3%). The CO_2 profiles support much of the previously stated assertions, although it is rather difficult to trace the origins of CO_2 data since it could have originated from the reaction of CO or CH_4. It could also still be present in the mixture simply as originally introduced diluent. What can be stated for certain is that the S5 mixture would be expected to produce more CO_2 than the S6 mixture, which is validated by the data.

The O2 and N2 radial profiles do not offer a great deal of further insight into the S5 and S6 flame structures. At z*=10%, the concentration of O_2 along the central axis of the S5 flame once again supports the notion that this first measurement lies within the flame cone. At this point, the O_2 concentration is almost equivalent to the initial concentration at the burner exit. In Figure 3.9, the O2 curves of each fuel differ only in terms of where the concentration returns to ambient air values. Evidently, the measurements suggest that the S6 fuel produces a thinner flame since the reaction boundary is located radially closer to the flame's central axis.

The presence of CH_4 among the reactants complicates the analysis. Furthermore, since CH_4 only accounts for 2.85% of the partially premixed mixture, its effect on the combustion of the system may not be apparent enough for proper examination. In this case, it appears as though the minimal concentration of CH4 begins oxidation prior to z*=10% and essentially reacts in its entirety prior to the z*=20%. Its contribution to the combustion of the system is largely

inconclusive, although recorded laminar flame lengths indicate that replacing 5% of CO_2 diluent with CH_4 has increased the overall mixture's burning rate. The effect of added CH_4 to syngas mixtures with CO_2 dilution should be further investigated in a future study by parametrizing the addition of CH_4.

3.4 Methane-Syngas Mixtures with CO_2 Dilution

Gaseous mixtures of methane and synthesis gas with carbon dioxide dilution are not uncommon and this section investigates two such mixtures. The S5M50 fuel is a mixture consisting primarily of methane (52.5%) with equivalent concentrations of CO and H_2 (18.75% each). The remaining 10% consists of CO_2 diluent. The second gaseous mixture, S5M25, is composed of similar concentrations of CO (28.125%), H_2 (28.125%) and CH_4 (28.75%). The remaining 15% consists of CO_2 diluent.

The S5M50 flame could not be sustained under the desired operating conditions therefore it was necessary to use the 10 mm burner in place of the 3.175 mm burner and reduce the Reynolds number from 1400 to 1000. This change in operating conditions permitted a sustainable flame for the S5M50 fuel, although only the measurements at z*=10% and 20% were retained due to instabilities present in the upper portion of the flame's height. As such, the conditions do not allow for a straightforward comparison between the two fuels. Furthermore, the compositions of each fuel do not lead to favourable comparison. For these reasons, the S5M50 and S5M25 fuel results are analysed separately.

3.4.1 S5M50 – 18.75CO/18.75H_2/52.5CH_4/10CO_2

The analysis of the S5M50 flame includes the presentation of both qualitative and quantitative results. The qualitative observations section discusses the appearance and behaviour of the visible flame as witnessed during experimentation. The quantitative results lead to the discussion of the chemical and thermal structure of the flame based on the profiles of flame temperature and major species concentration.

3.4.1.1 Qualitative Observations

With the 3.175 mm burner and a Reynolds number of 1400, a S5M50 flame could be observed only with a constant external flame source keeping the fuel ignited. The flame could be described in colour as transparent blue with a faint, lighter blue flame cone within it. To the naked eye, the thin-walled flame cone appeared quite long and occupied a significant portion of the overall flame's apparent volume.

The 10 mm burner allowed for an easily ignitable flame, although the Reynolds number was reduced to 1000 in order to reduce instabilities as the flame was susceptible to flicker. Measurements were taken at 10% and 20% of the flame's height as the stability of the lower region of the flame was the most satisfactory.

Under the new operating conditions, the flame's colour is unchanged (again, a transparent blue). However, there is no visible evidence of a flame cone in this scenario. The length and girth of the flame fluctuates often under these conditions; measurements were repeated several times before the flame remained relatively still over the time required to take the measurements.

3.4.1.2 Quantitative Results and Analysis

The temperature profile clearly indicates that, at low z* values, the flame's central axis is composed of unburned fuel close to ambient temperature. At z*=10%, this occurs within 3 mm of the flame's central axis before the temperature begins to increase with increasing radial distance, as seen in Figure 3.10. At z*=20%, the unburned gas region is narrower, occupying roughly a 1 mm radius before the temperature clearly increases as the radial distance from the center increases. In both cases, the maximum temperature is attained between 6 and 7 mm in radial distance from the flame's center.

With relatively low amounts of H_2 in the S5M50 gaseous mixture, it follows suit that only trace levels of H_2 were measured by z*=10%. This indicates that hydrogen reacts early in the

combustion process and is almost untraceable beyond the first 10% of the flame's height. The data suggests that hydrogen reacts before the carbon monoxide since, at z*=10%, there still remains almost half of the initial CO concentration and virtually no H_2, despite both molecules having equivalent initial concentrations. In both scenarios (H_2 and CO), it appears as though there is a very slight increase in concentration from z*=10% to 20%. Although the generally expected trend is for these species to decrease in concentration as the z* increases, it should be considered that both of these species are present in the steps of the CH_4 combustion process. Thus, through the dissociation of CH_4, it is possible that increases in H_2 and CO concentration can be measured. However, it cannot be proven that these slight increases in concentration are due to anything other than measurement inaccuracies since the CH_4 concentration at z/HT=10% matches its initial value at burner exit (roughly 18%). This suggests that CH_4 has not started to react. The reaction of CH_4 appears to begin somewhere between z*=10% and z*=20% since its concentration decreases along the central axis. This happens to coincide with the very slight increases in concentration of H_2 and CO.

At z*=10% and 20%, high levels of H_2O are measured along the flame's central axis, which is expected given the degree in which H_2 has already reacted. However, the experimental concentration of H_2O at z*=10% is already approximately equal to its stoichiometric value and remains more or less the same at z*=20%, despite the fact that there remains significant amounts of methane in the unburned fuel. The dissociation of methane cannot account for these higher than expected concentrations of H_2O since CH_4 does not appear to even begin reacting yet at z*=10%. Therefore, the high level of H_2O is likely attributable to inaccuracies. The maximum concentration of H_2O does not occur along the flame's central axis, but rather at an approximate 5 mm radius, which coincides with the radial location of maximum temperature.

The concentration of CO_2 increases, as expected, with increasing z*. However, the stoichiometric value is not attained at either z*=10% or 20%, suggesting that it is attained at a higher elevation. This is supported by the significant quantities of CO and CH_4 remaining in the unburned fuel mixture at the two test heights. At z*=10%, the concentration of CO_2

along the flame's central axis does not exceed its initial concentration (at the burner exit), which offers further evidence that the CO and CH_4 reactions have not initiated. As z* increases to 20%, the concentration of CO2 increases both at the central axis and at the location of maximum concentration. The maximum concentration occurs at a radius of approximately 4 mm for both test heights. This is more or less consistent with the flame boundaries that can be loosely determined from the N_2 and O_2 radial profiles.

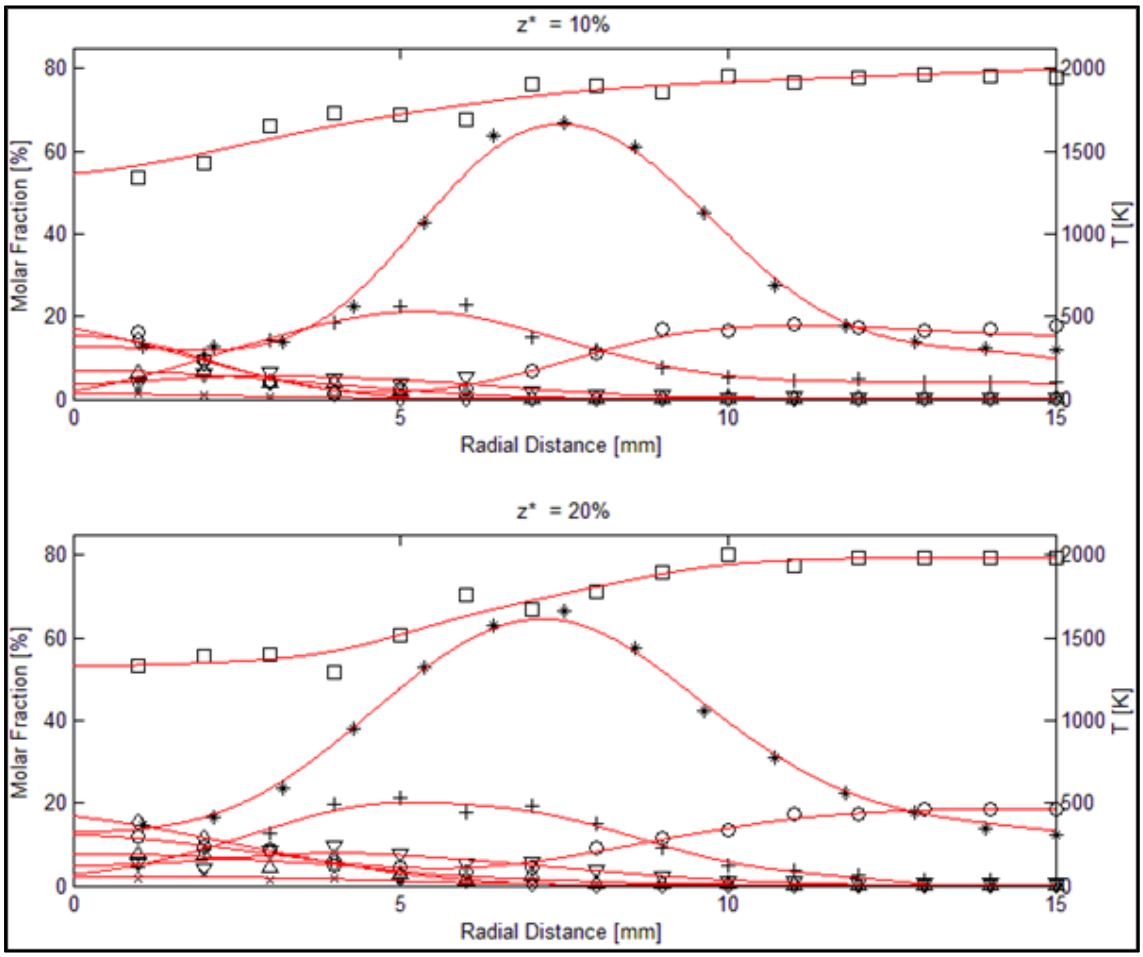

Figure 3.10 Radial profile of species concentration and flame temperature of S5M50 flame (×=H_2, Δ=CO, ◊=CH_4, +=H_2O, ∇=CO_2, □=N_2, ○=O_2, ∗=Temp)

3.4.2 S5M25 – 28.125CO/28.125H_2/28.75CH_4/15CO_2

3.4.2.1 Qualitative Observations

The S5M25 flame is very similar in colour but less transparent than the S5M50 flame. It has a slight colour gradient whereby the apex of the flame transitions from the blue body of the flame to a faint orange colour. There is a large flame cone (almost half the height of the overall flame) with thin, light blue edges located at the exit of the burner. The flame cone is quite noticeably rounded at its peak.

There were difficulties stabilizing the flame but the reasons for which are unclear from a visual standpoint. The flowmeters did not indicate that there were any difficulties in regulating the flows of the reactants, nor were there any difficulties with fuel ignition. Extra care was also taken to ensure that the flame was isolated from possible air flow variations in the room. However, the dimensions (particularly the length) of the flame fluctuated considerably. After several minutes, the flame generally appeared to stabilize. Therefore measurements were taken after a waiting period of roughly 3 minutes after flame ignition.

3.4.2.2 Quantitative Results and Analysis

The first S5M25 temperature profile displays a region along the flame's central axis where unburned fuel is measured at close to ambient temperature. This region corresponds to the inner volume of the flame cone described in section 3.4.2.1, and is consistent with the observation that the flame cone occupies the lower, inner portion of the flame's volume. Based on the measurements, it is suggested that the flame cone height is approximately equal to 40% of the flame's visible height since the temperature profile at z*=40% reveals a very slight decrease in temperature radially inward toward the flame's central axis. As expected, the tendency along the central axis is for the temperature to increase as z* increases. As well, the maximum temperature at each test height is located at the same approximate radial distance (between 3 and 4 mm). This provides insight into where the reaction boundary is located spatially. The location of this boundary is further supported in the CO and CH_4

profiles, where species concentrations decrease toward zero at an approximate radial distance of 4 to 5 mm. This signals the return to ambient air following the reaction of the fuel as the observer moves radially outward from the flame's central axis. In the case of CH_4, the concentration along the central axis at z*=10% indicates a 3% decrease from its initial value at the burner exit. This suggests that CH_4 has begun the oxidation process and by z*=20%, only a very small quantity remains. The dissociation of CH_4 can be a reason for this observation and it is supported by the CO and H_2 profiles. The concentration of CO at z*=10% is superior to the initial value at burner exit and the z*=20% concentration is equivalent to the initial value at burner exit, which suggests that there is an apparent "production" of CO early in the combustion process. A similar scenario is observed with hydrogen. At z*=10%, it appears that the majority of hydrogen has already reacted, reaching less than 1% molar fraction (down from roughly 12% initially at the burner exit). The concentration increases thereafter as z* increases, likely due to the dissociation of CH_4. The chemical kinetics of CH_4 combustion reveals that H_2 and CO are both integral components in the steps of reaction.

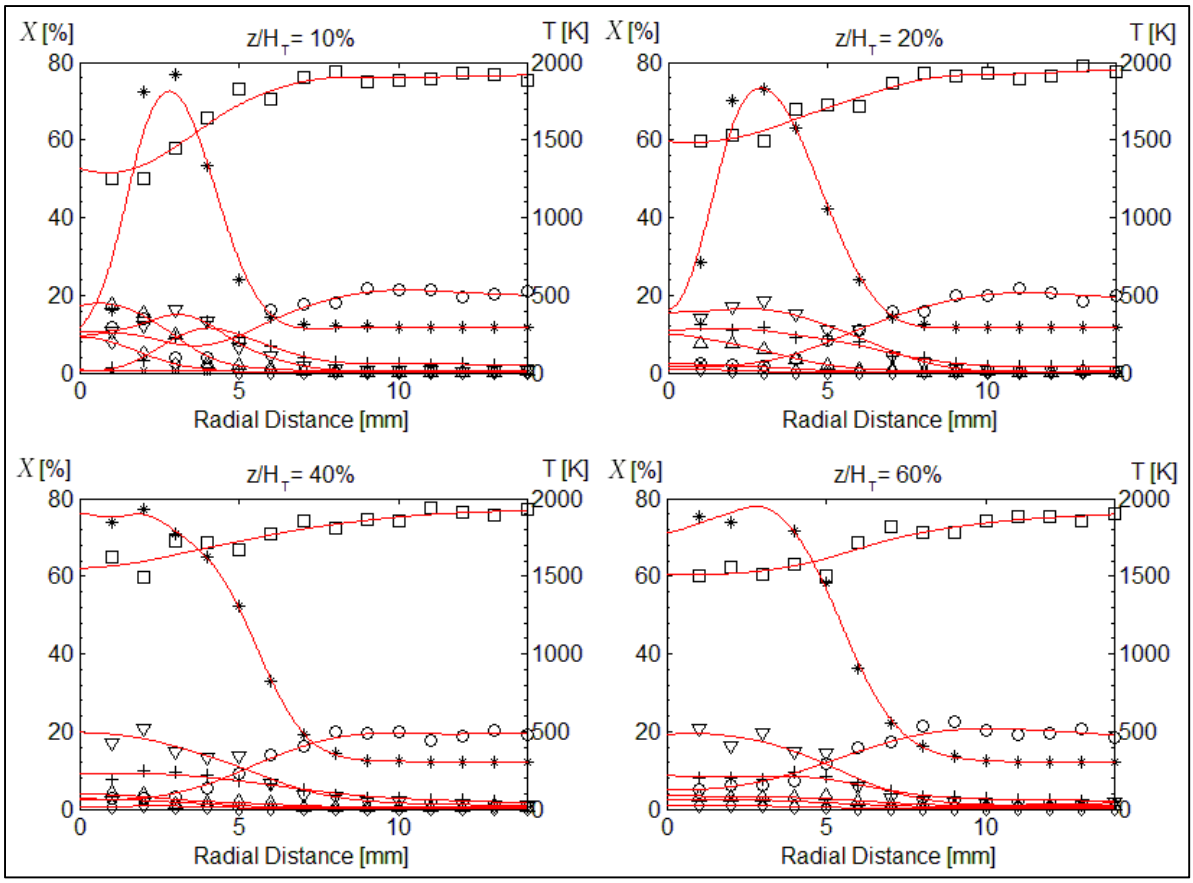

Figure 3.11 Radial profile of species concentration and flame temperature of S5M25 flame (×=H_2, Δ=CO, ◊=CH_4, +=H_2O, ∇=CO_2, □=N_2, ○=O_2, ∗=Temp)

The early oxidation of H_2 should in theory be complemented by an early increase in H_2O. Figure 3.11 reflects this exact notion at z*=10%, displaying a concentration of almost nil along the central axis and a rise in H_2O concentration moving radially outward. The maximum H_2O concentration is located at a radial distance of approximately 4 mm, which is consistent with the measured reaction boundary previously discussed. At this elevation, the maximum H_2O concentration does not coincide with the theoretical stoichiometric value, which is expected due to the remaining CH_4 yet to be oxidized. The H_2O concentration never quite reaches the stoichiometric value, even at higher elevations. It is likely that this occurs somewhere between z*=10% and z*=20%, where the maximum concentration remains the same but the concentration along the central axis has risen considerably. Somewhere between these two elevations is where both H_2 and CH_4 concentrations are close to zero, and therefore

it can be assumed that H2O concentration will be closest to the stoichiometric value. However, the presence of several different reacting species combined with their varying burning rates makes it quite difficult to predict or pinpoint where stoichiometric products of combustion will be observed. In the case of CO_2, which is both a diluent and a product of combustion for CO and CH4, it is particularly difficult to categorize its behaviour and origin in the combustion process. At low elevations (z*=10% and 20%), there is clearly an increase in CO2 concentration from its initial value at the burner exit. The concentration increases along the central axis with increasing z* while the maximum concentration is located at a radial distance of 3 mm. Above z*=20%, the mixture appears to be dominated by the inert gases N_2 and CO_2. This might explain the apparent inability of the remaining reactants to fully oxidize (referring to the remaining concentrations of CO and H_2 at z*=40% and 60%).

In Figure 3.11, the O_2 profile indicates that the oxidation largely takes place at the reaction boundary. This is evidenced by the higher concentration of O2 along the flame's central axis at z*=10%, which is close to the initial concentration at the burner exit. Moving radially outward from the central axis, the concentration of O_2 decreases and reaches a minimum between 3 and 4 mm, which coincides with the reaction boundary. Beyond this boundary, the O_2 concentration increases, gradually returning to ambient air conditions. At z*=20% and above, the concentration along the central axis is closer to zero and increases slowly as z* increases. However, at z*=20% and 40%, the concentration decreases slightly from the central axis and reaches a minimum at a radial distance of 3 mm. This further corroborates the notion that the flame cone height slightly surpasses 40% of the visible flame height.

3.5 Conclusion

In summary, the main objective of this study was to measure the flame temperature and the major species concentrations (H_2, CO, CH_4, H_2O, CO_2, O_2, N_2) via Raman laser spectroscopy for a collection of flames of syngas and biogas mixtures with CO_2 dilution. In addition to this main objective are several sub-objectives, which include an analysis of the effects of H_2/CO ratio as well as the effects of CO_2 addition on the flame structure of syngas flames with CO_2

dilution. Furthermore, the scope included an examination of the visible characteristics of each flame. The aim was to achieve flame ignition at target operating conditions of φ=3 and Re=1400 with a 3.175 diameter Bunsen burner at room temperature and pressure.

The B1 biogas mixture's flame was measured with a 10 mm Bunsen burner at Re=1000 in order to improve stability. It was discovered that the radial location at which CH_4 reaches zero corresponds to the radial location where H_2O reaches its maximum concentration. This also coincides with the minimum concentration of O_2. The maximum flame temperature is achieved before reaching z*=20% and is located along the flame's reaction boundary. However, at this elevation, the temperature of the unburned gas along the central axis remains ambient.

Syngas with 25% CO_2 dilution produced flames that allowed for an analysis of the effects of H_2/CO ratio and CO_2 addition on flame structure. It was shown that a decrease in H_2/CO ratio causes a decrease in flame temperature due to a rise in radiative heat loss from the increase in CO_2 production. A decrease in H_2/CO ratio can also be linked to longer flame cones stemming from a decrease in laminar burning velocity. On the other hand, higher H_2/CO ratios produce higher levels of H_2O and faster laminar burning rates. The analysis of CO_2 addition demonstrated that central axis temperature decreases in conjunction with CO_2 addition. The maximum flame temperature and laminar burning velocity also decrease with higher CO_2 dilution levels. CO_2 dilution caused a decrease in flame size as well.

The scope of the study included an investigation of syngas mixtures with 5% CH_4 and 20% CO_2 dilution. It was shown that the 5% of CH_4 reacts and/or dissociates early, within 10% of the flame's visible height. Higher H_2/CO ratios resulted in shorter flame cones, suggesting faster laminar burning velocities. This finding was supported by the predisposition of the central axis temperature to increase with z* at a faster rate than for lower H_2/CO ratios. However, H_2 addition can increase laminar burning velocities of such mixtures through chemical effects without necessarily increasing the adiabatic flame temperature.

The methane-syngas mixtures with CO_2 dilution exhibited relatively high flame cones, sometimes occupying nearly half of the visible flame's height. The species concentration results provided evidence of CH_4 dissociation, which was apparent as "increases" in measured concentrations of H_2 and CO species. Increases in H_2 and CO concentrations were recorded at lower values of z*. The maximum concentration of H_2O occurred at the same radial location as the maximum temperature.

It was generally witnessed amongst all flames that the reaction boundaries of laminar, partially premixed flames of syngas and biogas mixtures could be identified by a decrease in the concentrations of the unburned reactants and an increase in the concentrations of H_2O and CO_2. The reaction boundary is also characterized by an increase in O_2 and N_2 concentrations, which represents the diffusion of ambient air into the flame. The flame temperature reduces to room temperature beyond this reaction boundary as well.

CONCLUSION

The main objective of this study was to characterize the flames of several gaseous syngas and biofuel mixtures through experimental means. The gaseous mixtures are comprised of some or all of H_2, CO, CH_4 and CO_2 and the experiment consists of measuring the flame temperatures and concentrations of major species at various elevations of the flame through laser diagnostic techniques as well as visible flame length by direct digital photography.

First, the experimental method was validated with measurements of a partially premixed CH_4 flame that was successfully compared to the literature. The uncertainty analysis has shown that the flame height, equivalence ratio and flame temperature all have ranges of uncertainty below 10%, which is favourable and under the typical Rayleigh method value of 10%.

Both qualitative and quantitative results are provided for all biofuel, syngas and methane-syngas partially premixed flames. The qualitative results describe the visual characteristics of each flame, from which the following can be observed: an increase of the H_2/CO ratio or the addition of CO_2 or CH_4 increases flame length. Quantitative results portray temperature and species concentration profiles at 10%, 20%, 40% and 60% of each flame's visible height. The experimental results provide the opportunity to analyse the effects of H_2/CO ratio on flame structure as well as the effects of CO_2 dilution. In summary, increasing the H_2/CO ratio increases the production of H_2O and decreases the production of CO_2. It also has the effect of increasing the flame temperature particularly along the central axis. The addition of CO_2 has the effect of decreasing the flame temperature and decreasing the production of H_2O. Although the effects of CH_4 addition were largely inconclusive, results suggest that CH_4 has a tendency to react or dissociate at early stages of combustion.

RECOMMENDATIONS

Despite the fact that this project involved the research of a particular collection of fuels, future studies can highly benefit from a more controlled selection of test fuels. The purpose of this would be to establish a range of mixtures that would allow the experimental data to isolate the effect of each constituent. This would simplify the analysis by emphasizing the effect of the variable under investigation. For instance, future studies could improve the understanding of CH_4 addition to H_2/CO mixtures by studying a collection of fuels with varying concentrations of CH_4 at fixed H_2/CO ratios. By parametrizing the variable of interest, the experimental results provide a clearer illustration of the variable's effects. Furthermore, in the process of selecting the test fuels, it is worthwhile to invest some time in making sure that each fuel can be ignited with adequate stability at the same operating conditions. This would improve the analysis of the experimental results simply by allowing more flames to be compared.

Although the effects of H_2/CO ratio with CO_2 dilution have been investigated in this study, the analysis covered a very slim range of H_2/CO ratios and CO_2 dilution levels. In future studies, the effects of H_2/CO ratio could be studied under varying levels of CO_2 dilution. As well, the study could cover a broader range of H_2/CO ratios in order to characterize a wider variety of syngas flames. Such a study could be performed in the existing laboratory and results could then be compared to numerical simulations in order to validate various CFD models.

A nice addition to this study would be to include an experimental analysis of the laminar flame speed of each test flame. Such an endeavor could be performed with very little modification to the existing laboratory. A simple chemiluminescence filter or Schieren camera could effectively capture the flame cone edge with sufficient accuracy to calculate the laminar flame speed. The results could then be compared to numerical simulations to determine whether the combustion mechanisms satisfactorily approximate the true flame speeds.

APPENDIX I

RADIAL PROFILES OF SPECIES CONCENTRATION AND FLAME TEMPERATURE COMPLIMENTARY TO CHAPTER 3

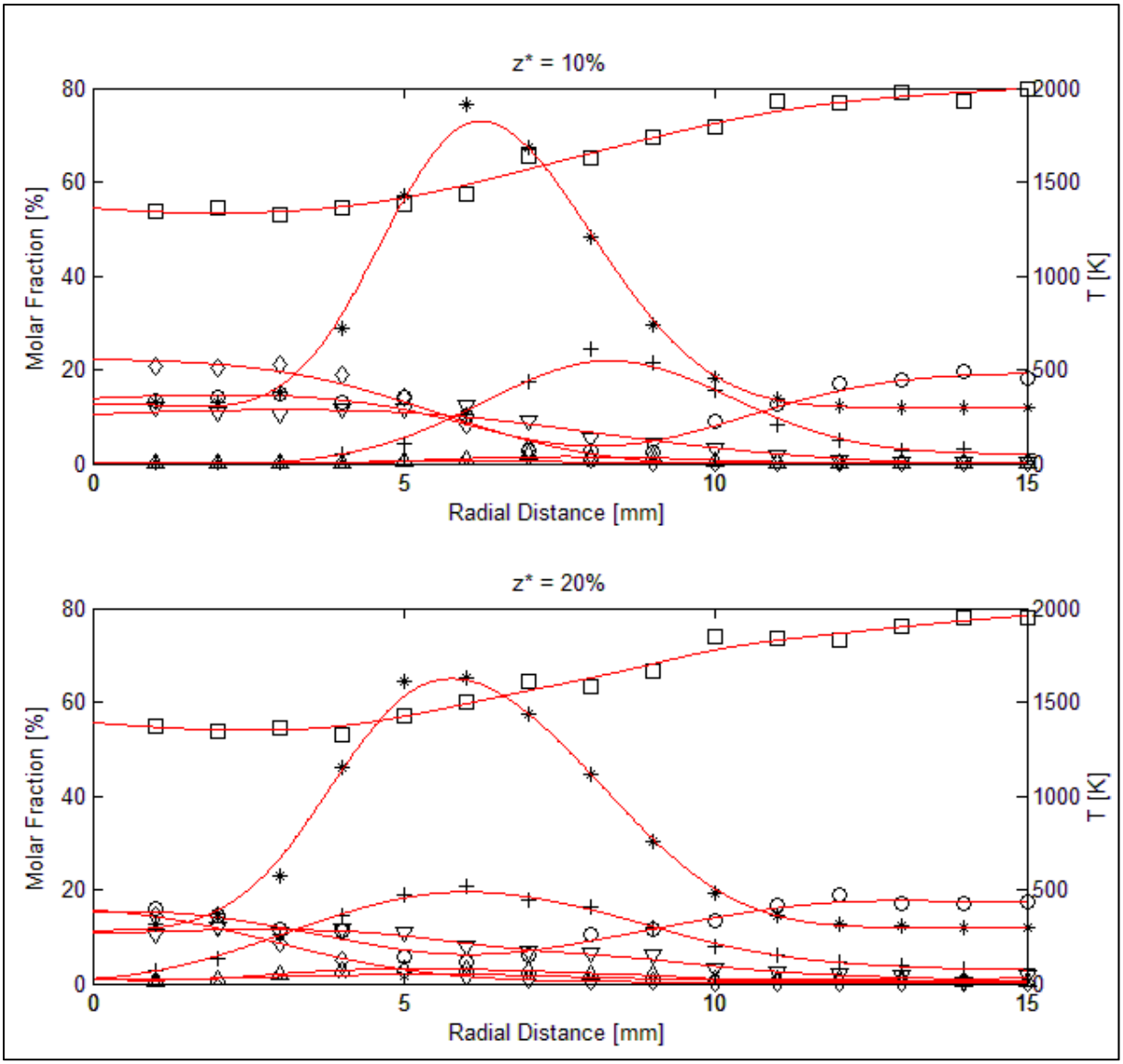

Figure-A I-1 Radial profile of B1 flame
(×=H_2, Δ=CO, +=H_2O, ∇=CO_2, □=N_2, ○=O_2, ∗=Temp)

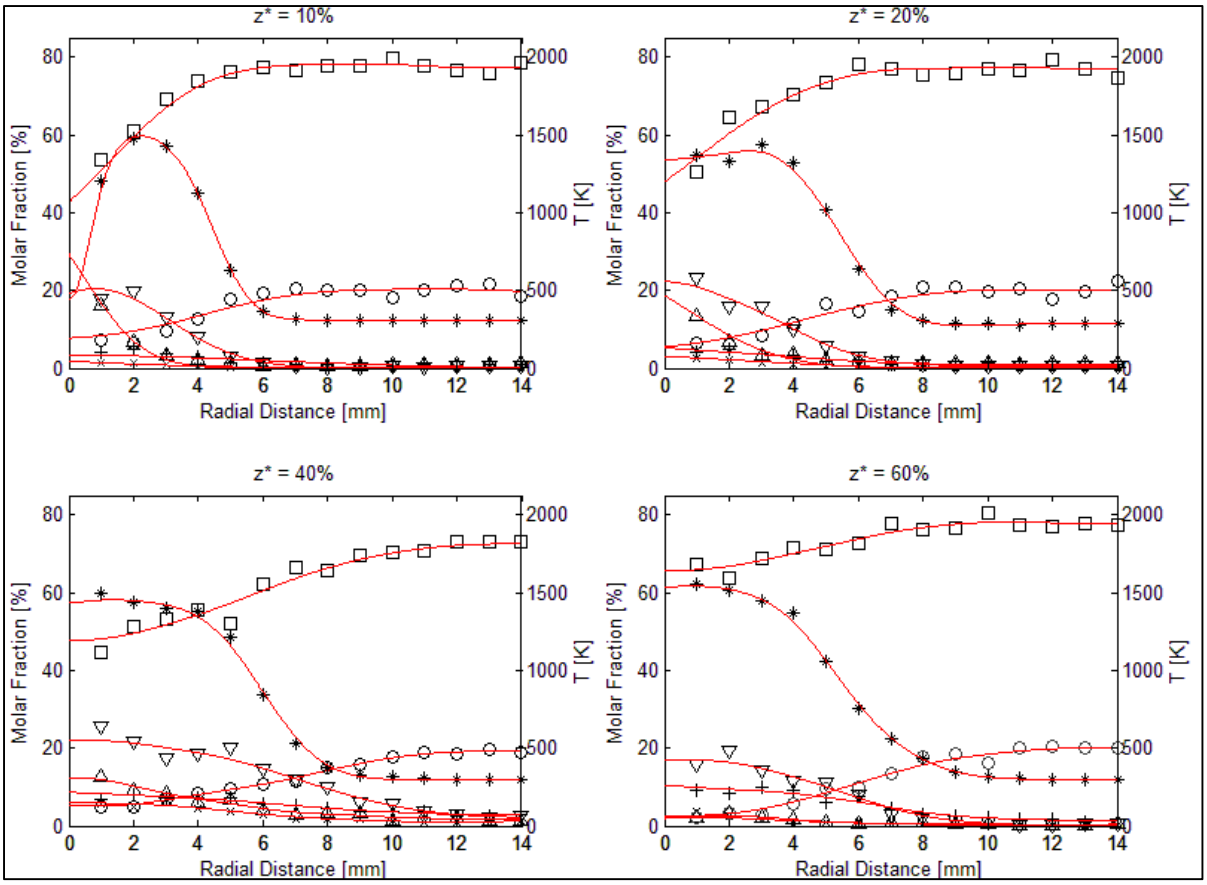

Figure-A I-2 Radial profile of S1 flame
(×=H_2, Δ=CO, +=H_2O, ∇=CO_2, □=N_2, ○=O_2, ∗=Temp)

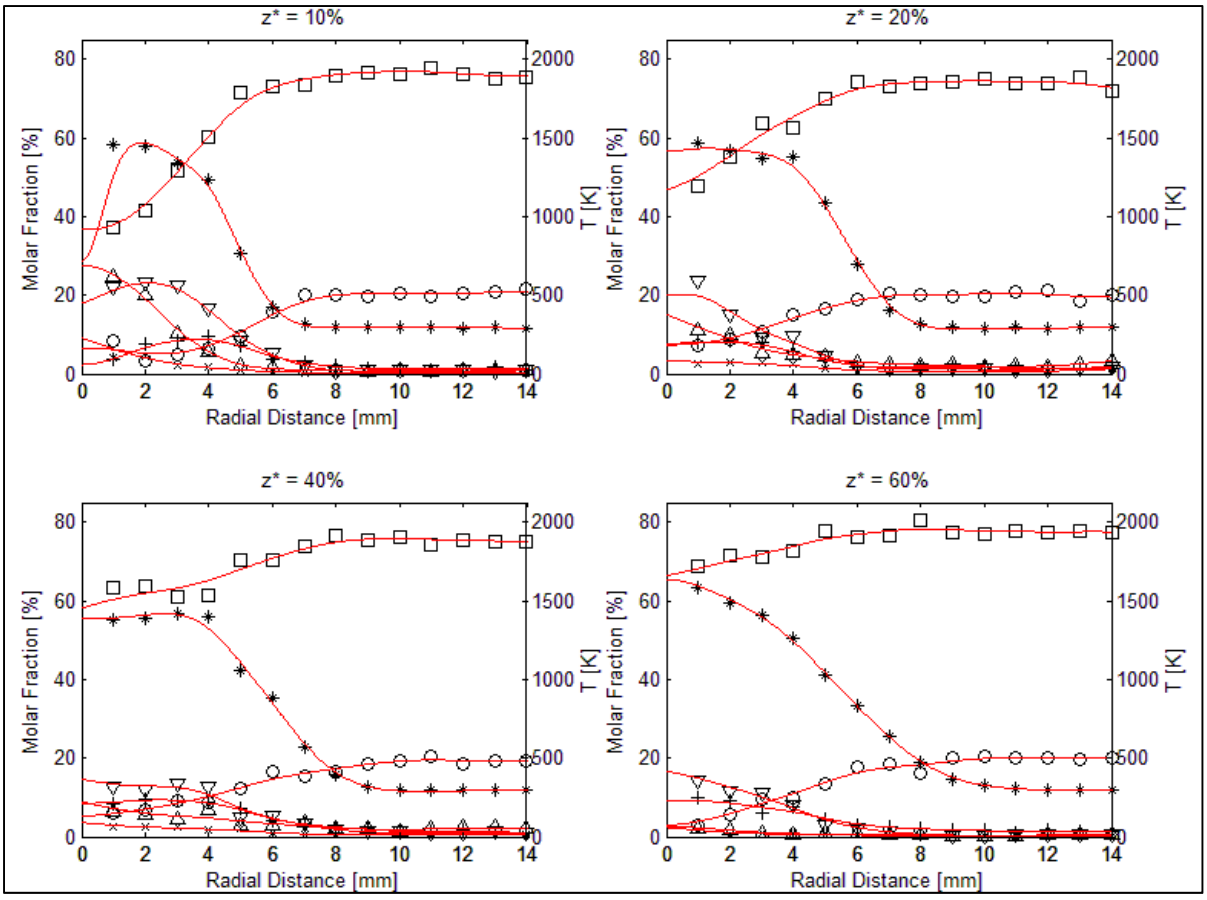

Figure-A I-3 Radial profile of S2 flame
(×=H_2, Δ=CO, +=H_2O, ∇=CO_2, □=N_2, ○=O_2, ∗=Temp)

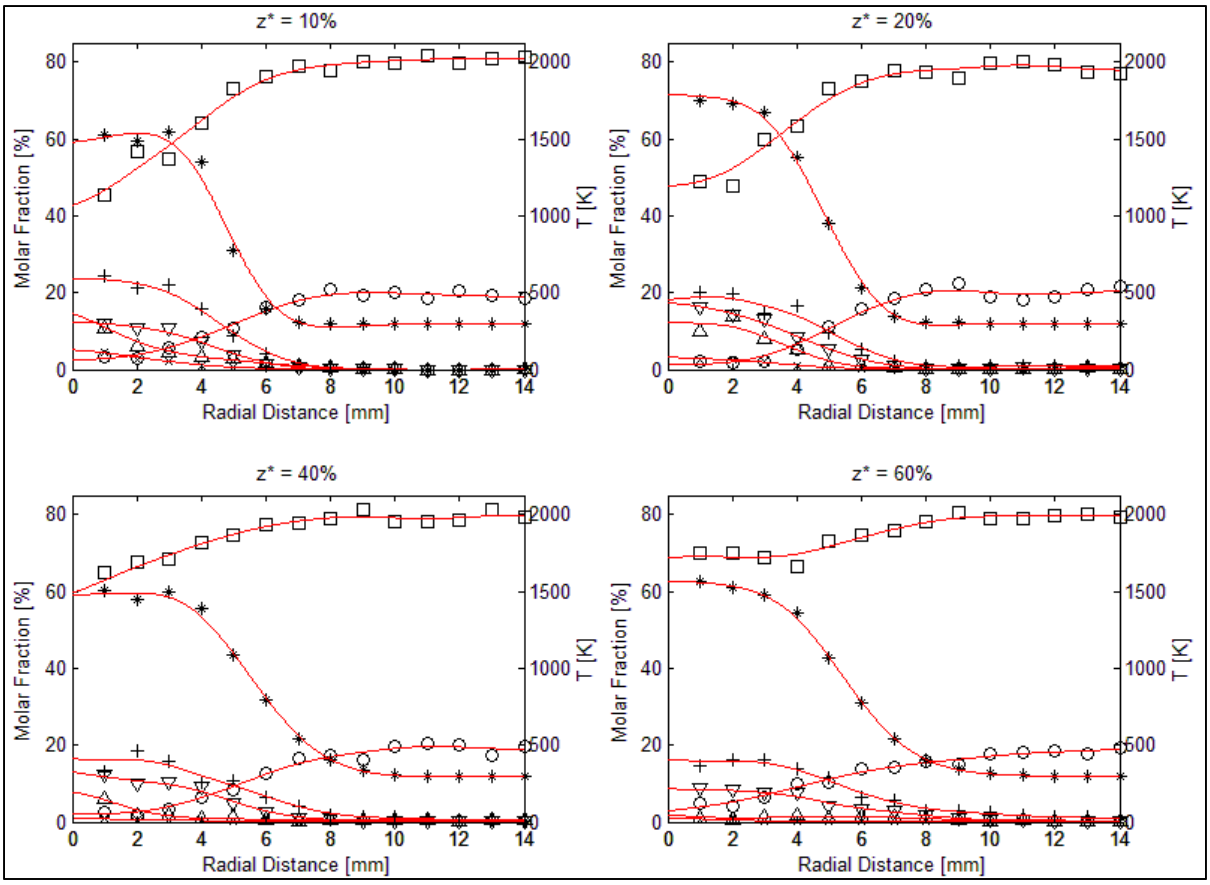

Figure-A I-4 Radial profile of S3 flame
(×=H_2, Δ=CO, +=H_2O, ∇=CO_2, □=N_2, ○=O_2, ∗=Temp)

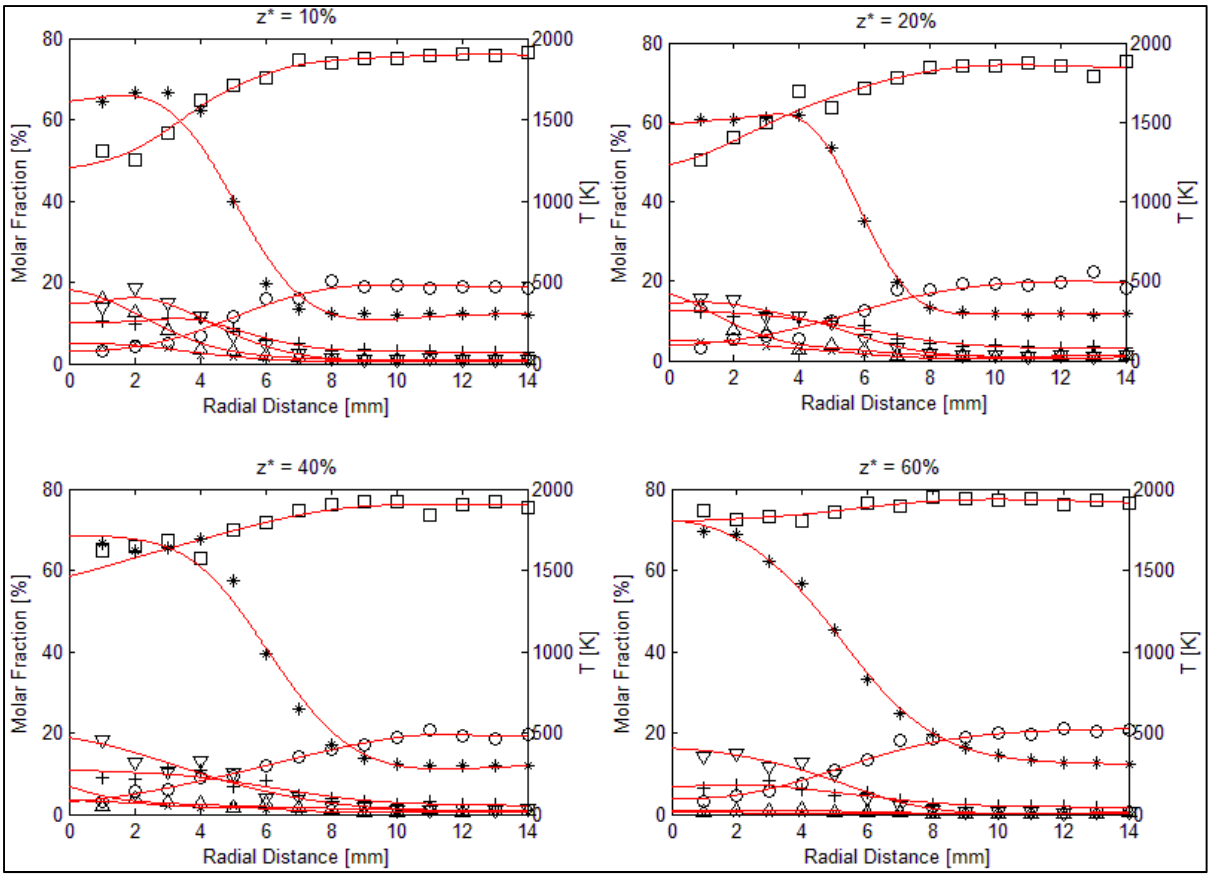

Figure-A I-5 Radial profile of S14 flame
(×=H_2, Δ=CO, +=H_2O, ∇=CO_2, □=N_2, ○=O_2, ∗=Temp)

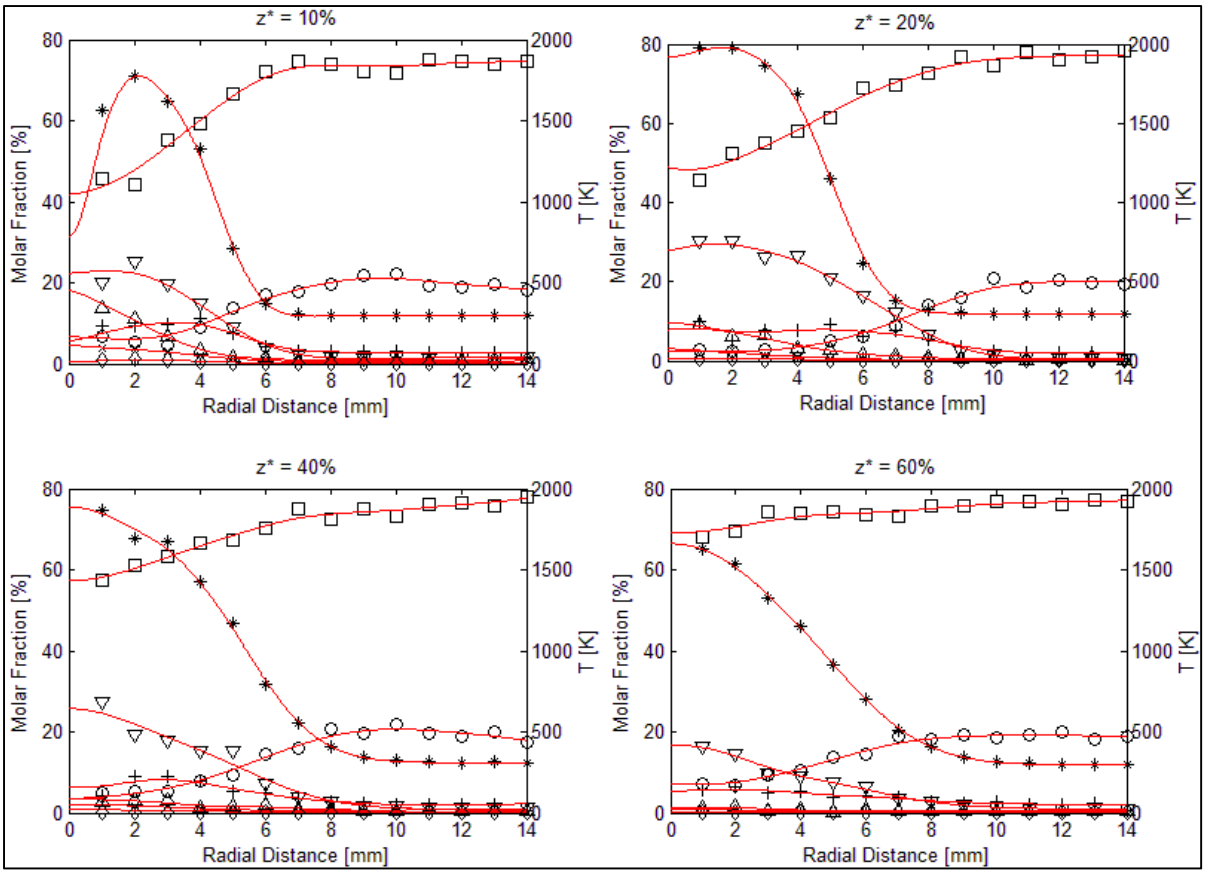

Figure-A I-6 Radial profile of S5 flame
(×=H_2, Δ=CO, ◊=CH_4, +=H_2O, ∇=CO_2, □=N_2, ○=O_2, ∗=Temp)

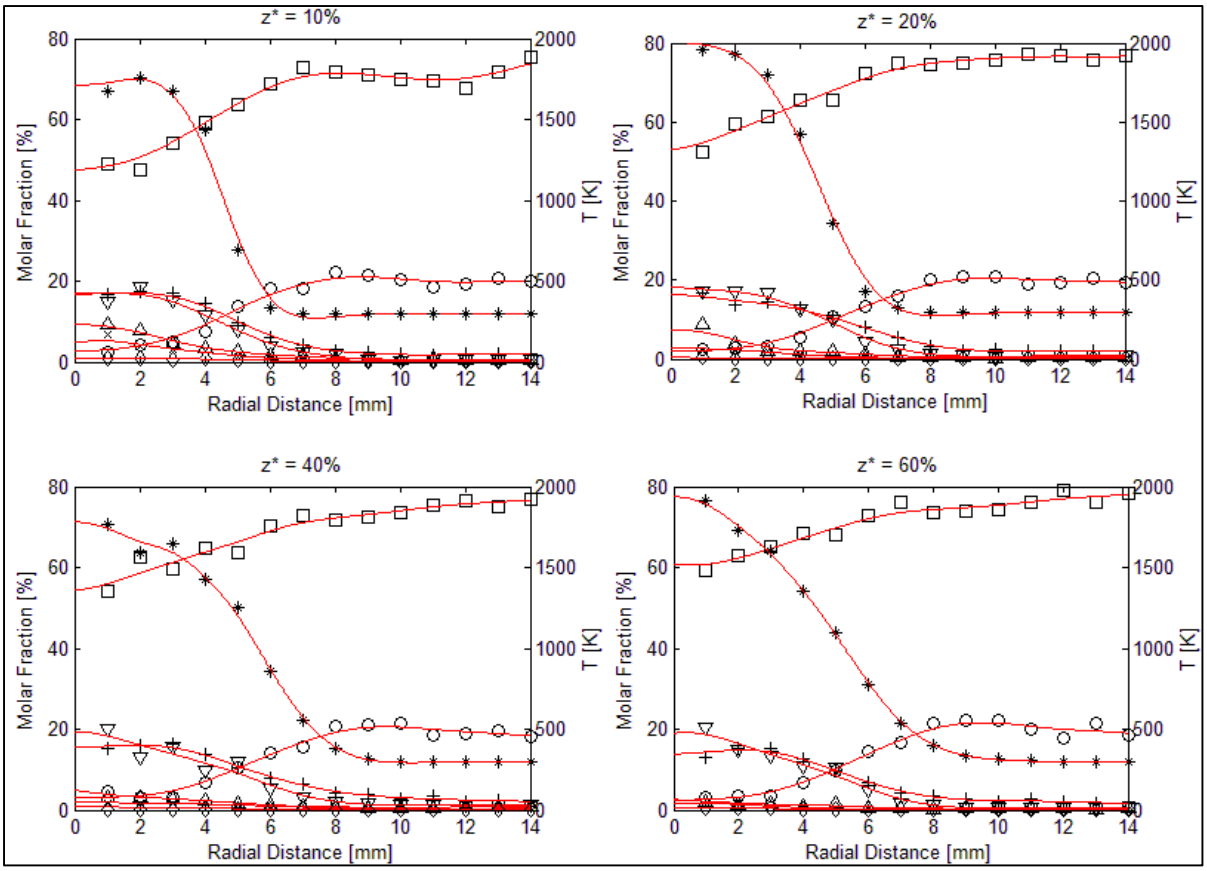

Figure-A I-7 Radial profile of S6 flame
(×=H_2, Δ=CO, ◊=CH_4, +=H_2O, ∇=CO_2, □=N_2, ○=O_2, ∗=Temp)

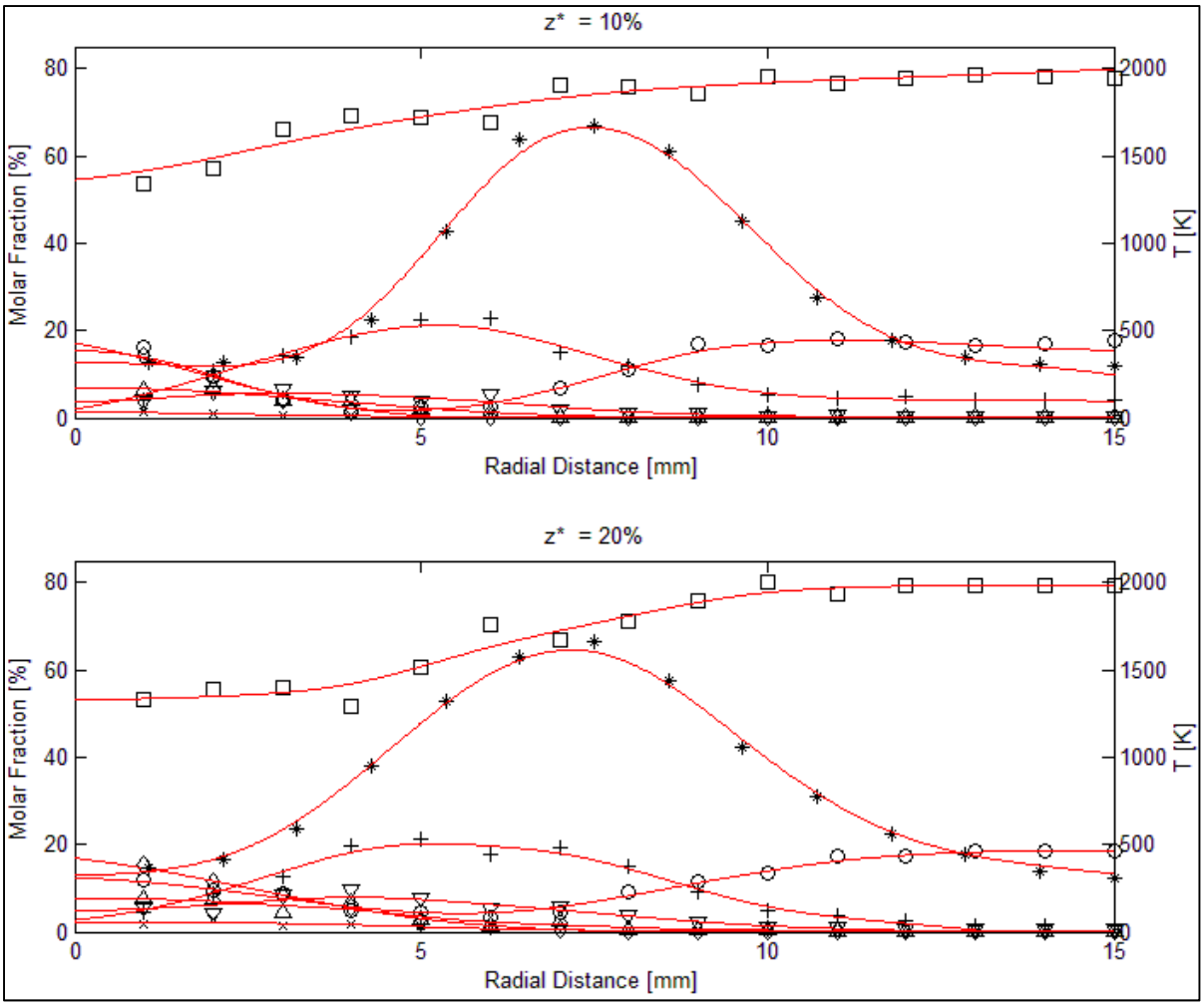

Figure-A I-8 Radial profile of S5M50 flame
(×=H_2, Δ=CO, ◊=CH_4, +=H_2O, ∇=CO_2, □=N_2, ○=O_2, ∗=Temp)

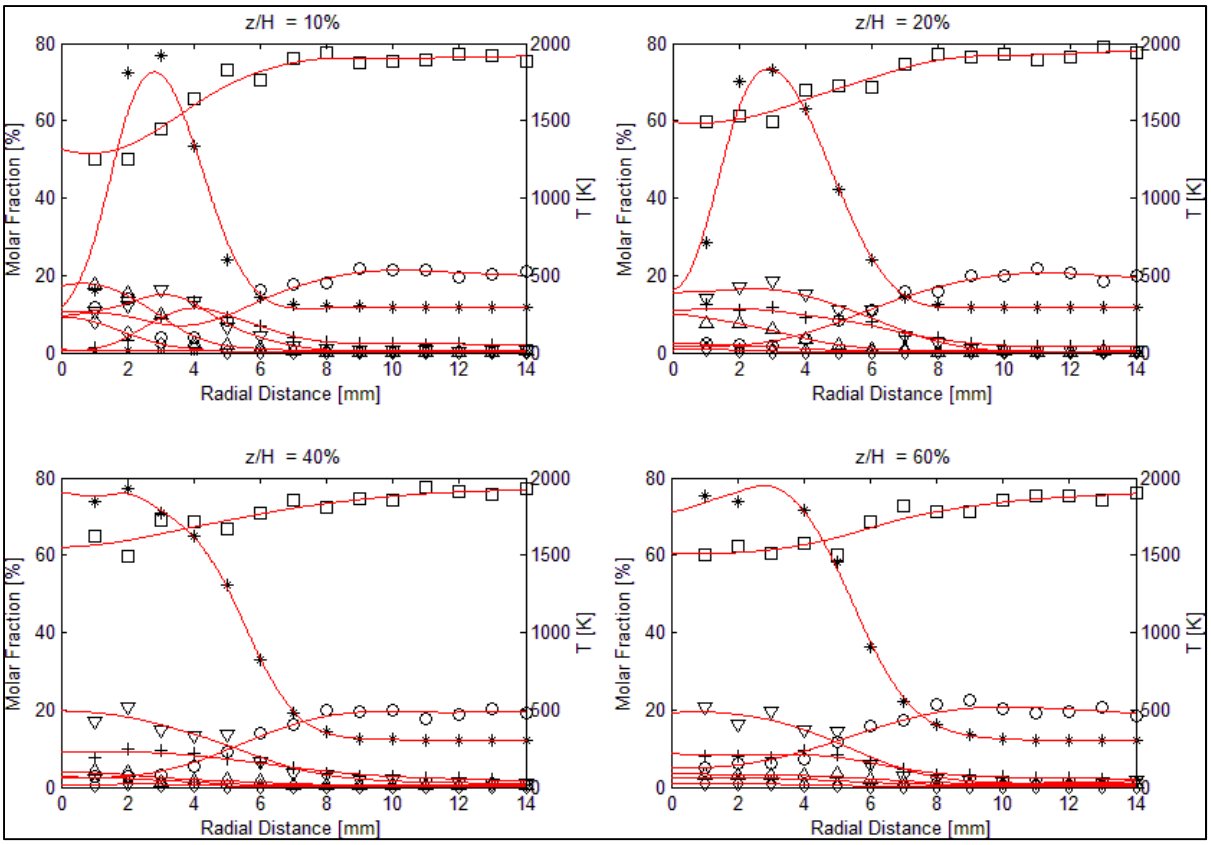

Figure-A I-9 Radial profile of S5M25 flame

(×=H_2, Δ=CO, ◊=CH_4, +=H_2O, ∇=CO_2, □=N_2, ○=O_2, ∗=Temp)

APPENDIX II

UNCERTAINTY ANALYSIS

Table-A II-1 Uncertainty estimation of the B1 temperature measurements

	z* = 10%		**z* = 20%**	
Radial Distance [mm]	**T [K]**	**U [%]**	**T [K]**	**U [%]**
0	322	4.01	310	3.30
1	325	4.01	313	3.30
2	325	4.01	374	3.24
3	379	3.96	573	3.10
4	717	3.74	1151	2.86
5	1425	3.51	1611	2.75
6	1909	3.42	1624	2.75
7	1685	3.46	1439	2.79
8	1203	3.57	1114	2.87
9	741	3.73	756	3.00
10	455	3.90	484	3.15
11	343	3.99	359	3.25
12	309	4.03	315	3.30
13	303	4.03	303	3.31
14	298	4.04	301	3.31
15	297	4.04	298	3.32

Table-A II-2 Uncertainty estimation of the S1 temperature measurements

	z* = 10%		z* = 20%		z* = 40%		z* = 60%	
Radial Distance [mm]	**T [K]**	**U [%]**	**T [K]**	**U [%]**	**T [K]**	**U [%]**	**T [K]**	**U [%]**
0	346	7.46	1304	6.36	1359	6.14	1502	6.07
1	1206	7.03	1373	6.34	1499	6.10	1554	6.06
2	1472	6.96	1326	6.35	1434	6.12	1514	6.07
3	1427	6.97	1435	6.33	1394	6.13	1450	6.09
4	1125	7.05	1323	6.35	1377	6.13	1372	6.10
5	630	7.26	1022	6.44	1218	6.17	1056	6.19
6	367	7.44	639	6.61	846	6.30	753	6.31
7	318	7.49	378	6.79	533	6.46	561	6.40
8	307	7.50	306	6.86	374	6.58	431	6.49
9	306	7.51	289	6.88	325	6.63	346	6.57
10	309	7.50	288	6.88	312	6.64	319	6.59
11	307	7.50	282	6.89	303	6.65	305	6.61
12	307	7.50	288	6.88	295	6.66	299	6.62
13	305	7.51	287	6.88	298	6.66	297	6.62
14	307	7.50	285	6.88	298	6.66	296	6.62

Table-A II-3 Uncertainty estimation of the S2 temperature measurements

	z* = 10%		z* = 20%		z* = 40%		z* = 60%	
Radial Distance [mm]	**T [K]**	**U [%]**	**T [K]**	**U [%]**	**T [K]**	**U [%]**	**T [K]**	**U [%]**
0	393	6.96	1365	6.33	1405	6.21	1685	6.10
1	1459	6.19	1465	6.28	1375	6.22	1585	6.14
2	1443	6.19	1416	6.30	1393	6.21	1484	6.18
3	1338	6.24	1366	6.33	1416	6.20	1413	6.21
4	1234	6.29	1380	6.32	1395	6.21	1260	6.27
5	770	6.56	1085	6.46	1058	6.38	1033	6.39
6	421	6.92	700	6.72	877	6.49	833	6.52
7	315	7.09	405	7.04	575	6.74	640	6.67
8	299	7.12	315	7.19	392	6.96	470	6.86
9	297	7.13	296	7.23	318	7.08	370	7.00
10	293	7.13	290	7.24	298	7.12	331	7.06
11	293	7.13	294	7.23	295	7.13	310	7.10
12	292	7.14	288	7.24	293	7.13	300	7.12
13	294	7.13	295	7.23	296	7.13	293	7.13
14	289	7.14	293	7.23	296	7.13	296	7.13

Table-A II-4 Uncertainty estimation of the S3 temperature measurements

	z* = 10%		z* = 20%		z* = 40%		z* = 60%	
Radial Distance [mm]	**T [K]**	**U [%]**	**T [K]**	**U [%]**	**T [K]**	**U [%]**	**T [K]**	**U [%]**
0	1425	6.11	1802	6.68	1439	6.01	1556	5.99
1	1525	6.06	1754	6.69	1511	6.00	1561	5.99
2	1491	6.08	1735	6.69	1445	6.01	1523	6.00
3	1547	6.06	1676	6.70	1495	6.00	1476	6.00
4	1354	6.14	1375	6.75	1385	6.02	1362	6.02
5	772	6.48	949	6.84	1089	6.06	1069	6.07
6	390	6.89	530	6.98	794	6.13	770	6.14
7	308	7.03	342	7.08	544	6.21	538	6.21
8	300	7.05	306	7.11	402	6.27	408	6.26
9	296	7.05	303	7.11	333	6.31	342	6.30
10	297	7.05	300	7.11	311	6.32	317	6.32
11	295	7.06	298	7.12	298	6.33	304	6.32
12	295	7.06	301	7.11	293	6.33	299	6.33
13	293	7.06	300	7.11	295	6.33	298	6.33
14	293	7.06	300	7.11	295	6.33	298	6.33

Table-A II-5 Uncertainty estimation of the S14 temperature measurements

	z* = 10%		z* = 20%		z* = 40%		z* = 60%	
Radial Distance [mm]	**T [K]**	**U [%]**	**T [K]**	**U [%]**	**T [K]**	**U [%]**	**T [K]**	**U [%]**
0	1497	4.64	1470	4.45	1770	4.28	1819	4.26
1	1610	4.61	1517	4.44	1669	4.30	1741	4.28
2	1667	4.59	1517	4.44	1621	4.31	1722	4.29
3	1666	4.59	1523	4.44	1634	4.31	1553	4.33
4	1559	4.62	1547	4.43	1694	4.29	1416	4.37
5	995	4.81	1338	4.49	1431	4.36	1135	4.46
6	491	5.10	877	4.67	985	4.52	833	4.59
7	335	5.26	492	4.90	650	4.69	623	4.71
8	307	5.29	337	5.06	431	4.86	488	4.81
9	304	5.30	305	5.10	343	4.95	412	4.88
10	301	5.30	295	5.12	310	5.00	363	4.93
11	305	5.30	291	5.12	302	5.01	336	4.96
12	303	5.30	295	5.12	300	5.01	321	4.98
13	305	5.30	290	5.12	300	5.01	317	4.99
14	302	5.30	295	5.12	300	5.01	310	5.00

Table-A II-6 Uncertainty estimation of the S5 temperature measurements

	z* = 10%		z* = 20%		z* = 40%		z* = 60%	
Radial Distance [mm]	**T [K]**	**U [%]**	**T [K]**	**U [%]**	**T [K]**	**U [%]**	**T [K]**	**U [%]**
0	467	7.33	1863	6.70	1893	6.70	1661	6.76
1	1564	6.71	1976	6.67	1869	6.70	1626	6.77
2	1775	6.65	1980	6.67	1694	6.75	1533	6.80
3	1621	6.69	1861	6.70	1677	6.76	1327	6.87
4	1324	6.80	1685	6.75	1422	6.84	1155	6.94
5	711	7.12	1153	6.95	1171	6.94	917	7.06
6	369	7.45	616	7.26	797	7.13	701	7.19
7	309	7.54	380	7.50	552	7.31	512	7.35
8	298	7.56	327	7.58	408	7.47	405	7.47
9	295	7.57	303	7.62	347	7.55	346	7.55
10	296	7.57	299	7.62	326	7.58	315	7.60
11	294	7.57	298	7.63	312	7.60	304	7.61
12	296	7.57	295	7.63	310	7.61	298	7.62
13	294	7.57	295	7.63	312	7.60	294	7.63
14	295	7.57	295	7.63	305	7.61	295	7.63

Table-A II-7 Uncertainty estimation of the S6 temperature measurements

	z* = 10%		z* = 20%		z* = 40%		z* = 60%	
Radial Distance [mm]	**T [K]**	**U [%]**	**T [K]**	**U [%]**	**T [K]**	**U [%]**	**T [K]**	**U [%]**
0	1730	8.41	1994	8.35	1793	8.39	1930	8.36
1	1678	8.42	1961	8.35	1765	8.40	1915	8.36
2	1760	8.40	1928	8.36	1592	8.44	1727	8.41
3	1677	8.42	1799	8.39	1649	8.42	1597	8.44
4	1432	8.48	1418	8.49	1424	8.49	1353	8.51
5	690	8.78	860	8.69	1253	8.54	1101	8.59
6	337	9.08	427	8.98	859	8.69	772	8.74
7	302	9.13	320	9.10	557	8.87	539	8.89
8	299	9.13	298	9.13	385	9.03	403	9.01
9	299	9.13	294	9.14	316	9.11	339	9.08
10	299	9.13	295	9.14	301	9.13	317	9.11
11	300	9.13	296	9.13	297	9.13	303	9.12
12	297	9.13	293	9.14	299	9.13	302	9.13
13	297	9.13	294	9.14	297	9.13	297	9.13
14	296	9.13	295	9.14	298	9.13	298	9.13

Table-A II-8 Uncertainty estimation of the S5M50 temperature measurements

	z* = 10%		**z* = 20%**	
Radial Distance [mm]	**T [K]**	**U [%]**	**T [K]**	**U [%]**
0	328	5.32	345	5.30
1	318	5.33	362	5.29
2	313	5.34	410	5.24
3	341	5.31	592	5.12
4	561	5.14	947	4.96
5	1071	4.92	1319	4.85
6	1591	4.79	1579	4.79
7	1676	4.77	1663	4.77
8	1528	4.80	1440	4.82
9	1129	4.90	1062	4.93
10	688	5.07	774	5.03
11	446	5.22	555	5.14
12	341	5.31	446	5.22
13	308	5.34	391	5.26
14	300	5.35	341	5.31
15	296	5.35	330	5.32

Table-A II-9 Uncertainty estimation of the S5M25 temperature measurements

	z* = 10%		z* = 20%		z* = 40%		z* = 60%	
Radial Distance [mm]	**T [K]**	**U [%]**	**T [K]**	**U [%]**	**T [K]**	**U [%]**	**T [K]**	**U [%]**
0	350	8.54	311	8.56	1936	8.33	1718	8.35
1	401	8.53	715	8.45	1843	8.34	1883	8.34
2	1806	8.34	1755	8.34	1929	8.33	1849	8.34
3	1916	8.33	1830	8.34	1771	8.34	2004	8.33
4	1338	8.38	1580	8.36	1623	8.35	1788	8.34
5	601	8.48	1059	8.41	1311	8.38	1451	8.37
6	363	8.54	598	8.48	819	8.44	903	8.43
7	313	8.56	360	8.54	479	8.50	552	8.49
8	300	8.56	307	8.56	357	8.54	409	8.52
9	299	8.56	294	8.56	316	8.56	341	8.55
10	296	8.56	295	8.56	310	8.56	315	8.56
11	297	8.56	291	8.57	303	8.56	306	8.56
12	294	8.56	291	8.57	303	8.56	306	8.56
13	296	8.56	290	8.57	304	8.56	304	8.56
14	295	8.56	295	8.56	303	8.56	303	8.56

APPENDIX III

SPECIES CONCENTRATION STANDARD DEVIATION

The following tables include the standard deviation readings for each of the species concentration measurements. Standard deviations were calculated using tools in the Davis 7.2 software (LaVision, 2007).

Table-A III-1 Standard deviation of species concentration measurements for the B1 flame

	z* = 10%						**z* = 20%**					
Distance [mm]	CO [%]	CO_2 [%]	H_2 [%]	H_2O [%]	O_2 [%]	N_2 [%]	CO [%]	CO_2 [%]	H_2 [%]	H_2O [%]	O_2 [%]	N_2 [%]
0	0.01	0.34	0.09	0.00	0.23	1.02	0.11	0.42	0.10	0.03	0.31	1.03
1	0.02	0.67	0.11	0.00	0.33	0.96	0.11	0.95	0.20	0.07	0.34	1.02
2	0.01	0.61	0.07	0.00	0.30	0.82	0.07	0.92	0.08	0.15	0.27	0.99
3	0.01	0.48	0.13	0.01	0.22	0.97	0.15	0.70	0.14	0.36	0.25	1.22
4	0.04	0.50	0.06	0.11	0.23	0.86	0.13	0.77	0.08	0.44	0.30	0.95
5	0.05	0.66	0.07	0.20	0.20	0.92	0.15	0.95	0.06	0.60	0.21	1.15
6	0.09	0.61	0.19	0.46	0.14	0.99	0.09	1.08	0.17	0.62	0.22	1.19
7	0.07	0.39	0.18	0.87	0.07	1.18	0.09	0.42	0.22	0.53	0.19	1.08
8	0.19	0.24	0.11	1.37	0.19	1.15	0.08	0.26	0.17	0.49	0.24	1.05
9	0.13	0.20	0.12	1.15	0.13	1.00	0.13	0.23	0.23	0.34	0.16	1.42
10	0.11	0.15	0.07	0.88	0.17	1.01	0.06	0.20	0.06	0.22	0.21	1.45
11	0.03	0.07	0.18	0.42	0.16	1.30	0.07	0.07	0.28	0.18	0.31	1.44
12	0.03	0.03	0.16	0.22	0.25	1.07	0.04	0.06	0.24	0.11	0.28	1.25
13	0.01	0.03	0.12	0.14	0.21	1.01	0.06	0.04	0.15	0.12	0.27	1.45
14	0.01	0.01	0.14	0.17	0.31	1.00	0.04	0.01	0.20	0.21	0.29	1.77
15	0.02	0.01	0.09	0.11	0.21	1.44	0.04	0.01	0.11	0.15	0.21	1.39

Table-A III-2 Standard deviation of species concentration measurements for the S1 flame

	z* = 10%						**z* = 20%**					
Distance [mm]	CO [%]	CO_2 [%]	H_2 [%]	H_2O [%]	O_2 [%]	N_2 [%]	CO [%]	CO_2 [%]	H_2 [%]	H_2O [%]	O_2 [%]	N_2 [%]
0	0.80	0.52	0.03	0.43	0.49	0.57	0.59	0.33	0.21	0.33	0.18	0.70
1	0.66	0.57	0.06	0.34	0.42	0.86	0.40	0.62	0.17	0.24	0.34	0.76
2	0.44	0.74	0.16	0.25	0.43	1.00	0.39	0.56	0.09	0.31	0.23	0.94
3	0.34	0.44	0.23	0.35	0.48	0.95	0.23	0.88	0.10	0.23	0.41	0.85
4	0.23	0.43	0.05	0.26	0.41	1.26	0.33	0.43	0.04	0.13	0.62	1.16
5	0.14	0.39	0.09	0.08	0.63	1.17	0.21	0.64	0.01	0.10	0.78	0.92
6	0.07	0.25	0.03	0.10	0.97	1.41	0.13	0.29	0.04	0.34	0.52	1.02
7	0.11	0.11	0.04	0.04	0.76	0.99	0.10	0.30	0.03	0.06	0.57	1.00
8	0.08	0.12	0.03	0.04	0.80	1.42	0.11	0.20	0.03	0.08	0.88	1.17
9	0.08	0.11	0.03	0.07	1.10	1.31	0.12	0.12	0.04	0.20	1.26	1.09
10	0.12	0.14	0.02	0.04	0.64	1.03	0.14	0.15	0.02	0.06	0.63	0.95
11	0.10	0.11	0.01	0.13	0.73	1.20	0.10	0.08	0.02	0.09	0.84	1.23
12	0.10	0.11	0.02	0.03	1.21	0.99	0.09	0.12	0.02	0.07	0.69	1.41
13	0.07	0.17	0.04	0.04	1.00	1.01	0.14	0.07	0.02	0.04	0.73	1.15
14	0.11	0.11	0.03	0.05	0.78	0.88	0.15	0.08	0.01	0.11	0.85	1.02
	z* = 40%						**z* = 60%**					
Distance [mm]	CO [%]	CO_2 [%]	H_2 [%]	H_2O [%]	O_2 [%]	N_2 [%]	CO [%]	CO_2 [%]	H_2 [%]	H_2O [%]	O_2 [%]	N_2 [%]
0	0.29	0.21	0.10	1.24	0.26	0.72	0.18	0.88	0.16	1.00	1.12	0.99
1	0.25	0.20	0.31	0.31	0.29	0.82	0.23	0.99	0.20	0.52	0.70	1.23
2	0.28	0.21	0.09	0.35	0.31	0.91	0.41	0.42	0.44	0.76	0.62	0.97
3	0.30	0.30	0.20	0.41	0.36	1.01	0.30	0.71	0.21	0.72	0.55	0.87
4	0.18	0.16	0.23	0.72	0.44	0.87	0.36	0.59	0.05	0.37	0.61	1.02
5	0.26	0.27	0.32	0.31	0.54	0.88	0.23	0.74	0.27	0.66	0.34	1.07
6	0.18	0.18	0.08	0.78	0.41	0.86	0.15	0.67	0.41	0.79	0.60	0.94
7	0.15	0.35	0.09	0.27	0.70	1.08	0.16	0.20	0.30	0.40	0.41	1.09
8	0.19	0.32	0.11	0.56	0.97	1.11	0.26	0.33	0.10	0.37	0.29	1.19
9	0.15	0.23	0.10	0.16	0.57	1.14	0.17	0.28	0.04	0.14	0.46	0.94
10	0.09	0.21	0.11	0.37	0.89	1.12	0.15	0.18	0.14	0.28	0.41	1.36
11	0.14	0.23	0.09	0.68	0.90	1.34	0.08	0.15	0.15	0.10	0.34	1.10
12	0.13	0.11	0.07	0.17	0.76	1.06	0.10	0.09	0.06	0.18	0.31	1.12
13	0.09	0.16	0.09	0.19	0.94	0.97	0.07	0.12	0.04	0.05	0.26	1.23
14	0.10	0.07	0.04	0.12	0.75	1.12	0.09	0.16	0.03	0.12	0.39	1.14

Table-A III-3 Standard deviation of species concentration measurements for the S2 flame

	z* = 10%						**z* = 20%**					
Distance [mm]	CO [%]	CO_2 [%]	H_2 [%]	H_2O [%]	O_2 [%]	N_2 [%]	CO [%]	CO_2 [%]	H_2 [%]	H_2O [%]	O_2 [%]	N_2 [%]
0	0.96	0.54	0.67	0.04	0.82	0.90	0.51	0.41	0.59	0.62	0.34	0.87
1	1.25	0.59	0.59	0.27	0.63	0.59	0.59	0.54	0.25	0.47	0.47	0.85
2	1.35	0.46	0.77	0.30	0.22	0.55	0.47	0.73	0.21	0.86	0.75	1.42
3	0.82	0.69	0.58	0.30	0.33	1.00	0.29	0.72	0.45	0.76	0.32	1.25
4	1.38	0.91	0.67	0.98	0.30	1.62	0.19	0.84	0.32	0.34	0.46	0.98
5	0.23	0.36	0.44	0.58	0.34	0.92	0.18	0.67	0.27	0.21	0.64	1.15
6	0.33	0.58	0.15	0.39	0.82	1.03	0.19	0.24	0.17	0.11	0.74	0.76
7	0.17	0.40	0.15	0.41	1.09	1.49	0.19	0.19	0.16	0.22	0.89	1.62
8	0.13	0.29	0.22	0.14	0.65	1.08	0.26	0.11	0.13	0.16	1.61	1.75
9	0.14	0.13	0.14	0.10	0.86	1.35	0.27	0.23	0.08	0.22	0.91	0.75
10	0.09	0.20	0.12	0.15	1.29	1.46	0.11	0.21	0.26	0.29	1.17	1.60
11	0.14	0.20	0.05	0.15	0.97	1.48	0.22	0.12	0.13	0.25	0.75	1.38
12	0.11	0.22	0.09	0.27	0.81	0.88	0.14	0.10	0.11	0.12	0.66	1.17
13	0.07	0.07	0.14	0.24	1.04	1.22	0.17	0.12	0.17	0.23	0.96	1.70
14	0.18	0.13	0.10	0.17	0.67	1.54	0.17	0.20	0.16	0.10	1.00	1.33
	z* = 40%						**z* = 60%**					
Distance [mm]	CO [%]	CO_2 [%]	H_2 [%]	H_2O [%]	O_2 [%]	N_2 [%]	CO [%]	CO_2 [%]	H_2 [%]	H_2O [%]	O_2 [%]	N_2 [%]
0	0.46	0.73	0.63	0.33	0.31	1.63	0.11	0.84	0.33	0.75	0.11	1.77
1	0.25	0.33	0.24	0.21	0.38	1.31	0.41	0.35	0.54	0.27	0.30	1.38
2	0.48	0.74	0.43	0.40	0.47	0.76	0.30	0.34	0.15	0.45	0.24	1.02
3	0.29	0.58	0.78	0.72	0.31	0.76	0.66	0.50	0.15	0.83	0.41	1.65
4	0.53	0.72	0.16	0.63	0.42	1.03	0.22	0.85	0.22	0.39	0.46	1.11
5	0.16	0.45	0.47	0.77	0.37	1.62	0.20	0.45	0.05	0.65	0.51	1.23
6	0.30	0.40	0.20	0.20	0.56	2.02	0.29	0.37	0.09	0.29	0.76	2.15
7	0.19	0.28	0.24	0.42	0.63	1.04	0.22	0.45	0.05	0.31	1.09	0.87
8	0.13	0.35	0.13	0.35	0.96	1.98	0.12	0.18	0.03	0.15	0.73	1.23
9	0.16	0.26	0.20	0.20	0.97	1.81	0.29	0.10	0.07	0.18	0.80	1.55
10	0.12	0.14	0.13	0.19	0.76	1.23	0.10	0.15	0.06	0.17	0.46	1.00
11	0.27	0.15	0.14	0.18	0.77	1.57	0.09	0.19	0.04	0.23	0.52	0.94
12	0.10	0.08	0.18	0.23	1.25	1.45	0.16	0.20	0.04	0.13	0.69	1.15
13	0.32	0.11	0.10	0.14	1.04	0.86	0.15	0.24	0.01	0.11	1.22	1.27
14	0.11	0.04	0.06	0.11	0.89	1.53	0.21	0.09	0.03	0.24	0.81	1.39

Table-A III-4 Standard deviation of species concentration measurements for the S3 flame

	z* = 10%						**z* = 20%**					
Distance [mm]	CO [%]	CO_2 [%]	H_2 [%]	H_2O [%]	O_2 [%]	N_2 [%]	CO [%]	CO_2 [%]	H_2 [%]	H_2O [%]	O_2 [%]	N_2 [%]
0	0.63	1.02	0.82	0.79	0.08	0.85	0.65	0.56	0.44	0.71	0.12	1.12
1	0.60	0.68	1.20	0.77	0.17	1.13	0.40	0.58	0.66	1.13	0.08	1.24
2	0.84	1.10	1.13	0.73	0.10	0.51	1.54	0.76	0.62	0.98	0.12	0.70
3	0.58	1.13	0.36	0.89	0.18	0.70	1.15	1.03	0.36	0.77	0.10	1.33
4	0.52	1.04	0.30	1.02	0.29	0.81	1.33	1.18	0.30	1.43	0.29	1.41
5	0.16	0.80	0.23	0.48	0.39	1.64	0.33	1.37	0.23	1.24	0.70	1.28
6	0.20	0.54	0.02	0.84	0.99	1.04	0.44	1.03	0.02	0.56	1.04	1.24
7	0.23	0.29	0.09	0.24	1.44	1.06	0.26	0.75	0.09	0.49	0.64	1.19
8	0.13	0.35	0.04	0.20	1.24	1.51	0.10	0.19	0.04	0.25	1.04	0.93
9	0.16	0.08	0.01	0.22	0.78	0.97	0.21	0.09	0.01	0.24	1.17	1.36
10	0.10	0.20	0.02	0.17	0.77	0.90	0.10	0.13	0.02	0.19	1.12	1.93
11	0.10	0.15	0.02	0.31	1.23	1.41	0.19	0.25	0.02	0.13	1.10	1.36
12	0.11	0.17	0.04	0.29	0.64	1.10	0.18	0.11	0.04	0.30	1.07	1.24
13	0.24	0.12	0.03	0.16	0.86	1.22	0.27	0.06	0.03	0.19	1.02	1.49
14	0.20	0.15	0.01	0.21	1.09	1.97	0.11	0.11	0.01	0.13	0.86	1.49
	z* = 40%						**z* = 60%**					
Distance [mm]	CO [%]	CO_2 [%]	H_2 [%]	H_2O [%]	O_2 [%]	N_2 [%]	CO [%]	CO_2 [%]	H_2 [%]	H_2O [%]	O_2 [%]	N_2 [%]
0	0.61	0.41	0.95	0.51	0.19	0.97	0.33	0.34	0.21	0.65	0.26	1.13
1	0.92	0.72	1.10	0.44	0.14	0.83	0.34	0.81	0.57	0.26	0.12	1.34
2	0.40	0.74	0.48	0.33	0.12	1.17	0.22	1.14	0.11	0.48	0.27	1.07
3	0.58	0.80	0.36	0.85	0.21	1.10	0.31	0.83	0.02	0.28	0.42	1.29
4	0.15	0.88	0.30	0.44	0.34	1.37	0.34	1.11	0.05	0.24	0.30	1.62
5	0.39	0.56	0.23	0.46	0.57	1.72	0.28	0.31	0.07	0.48	0.44	1.75
6	0.11	0.23	0.02	0.55	0.77	1.03	0.17	0.55	0.05	0.21	0.67	1.05
7	0.04	0.27	0.03	0.37	0.74	1.35	0.37	0.53	0.04	0.26	0.92	1.11
8	0.35	0.31	0.01	0.15	0.99	0.82	0.13	0.25	0.06	0.34	0.70	0.97
9	0.29	0.09	0.02	0.46	1.03	1.70	0.29	0.14	0.03	0.15	0.78	1.68
10	0.21	0.03	0.01	0.51	1.09	1.29	0.09	0.08	0.06	0.24	0.52	0.91
11	0.15	0.05	0.02	0.45	0.68	1.53	0.14	0.13	0.04	0.22	0.86	0.98
12	0.12	0.05	0.00	0.40	1.44	1.30	0.07	0.18	0.01	0.15	0.77	1.52
13	0.11	0.04	0.01	0.12	0.75	1.33	0.12	0.16	0.01	0.40	0.60	0.97
14	0.07	0.08	0.01	0.12	0.73	0.85	0.14	0.04	0.01	0.17	0.64	1.03

Table-A III-5 Standard deviation of species concentration measurements for the S14 flame

	z* = 10%						**z* = 20%**					
Distance [mm]	CO [%]	CO_2 [%]	H_2 [%]	H_2O [%]	O_2 [%]	N_2 [%]	CO [%]	CO_2 [%]	H_2 [%]	H_2O [%]	O_2 [%]	N_2 [%]
0	0.54	0.41	0.41	0.31	0.23	0.90	0.62	0.65	0.32	0.49	0.22	1.03
1	0.57	0.45	0.22	0.37	0.22	1.02	0.72	0.56	0.29	0.19	0.19	0.73
2	0.64	0.49	0.42	0.32	0.24	0.87	0.34	0.57	0.45	0.35	0.53	1.12
3	0.40	0.72	0.61	0.38	0.22	1.43	0.86	0.28	0.35	0.19	0.21	1.06
4	0.20	0.42	0.40	0.27	0.34	0.81	0.24	1.04	0.12	0.65	0.31	2.11
5	0.33	0.43	0.37	0.36	0.75	1.62	0.82	0.51	0.22	0.35	0.55	1.20
6	0.34	0.49	0.11	0.19	1.08	0.91	0.54	0.50	0.45	0.59	0.37	1.13
7	0.40	0.48	0.07	0.24	0.70	1.77	0.10	0.69	0.04	0.23	0.67	0.97
8	0.16	0.18	0.11	0.27	0.64	1.03	0.10	0.26	0.13	0.26	0.64	1.45
9	0.18	0.19	0.08	0.21	0.73	1.05	0.13	0.26	0.11	0.14	0.90	1.18
10	0.09	0.21	0.04	0.14	1.02	0.73	0.10	0.14	0.04	0.24	0.75	1.18
11	0.07	0.23	0.04	0.09	0.67	0.81	0.12	0.24	0.08	0.19	1.04	1.41
12	0.21	0.15	0.03	0.18	1.00	2.20	0.08	0.20	0.04	0.22	0.93	1.35
13	0.08	0.18	0.07	0.15	1.07	1.40	0.11	0.15	0.05	0.09	1.38	1.99
14	0.06	0.16	0.10	0.14	0.66	1.05	0.28	0.15	0.16	0.20	0.78	1.13
	z* = 40%						**z* = 60%**					
Distance [mm]	CO [%]	CO_2 [%]	H_2 [%]	H_2O [%]	O_2 [%]	N_2 [%]	CO [%]	CO_2 [%]	H_2 [%]	H_2O [%]	O_2 [%]	N_2 [%]
0	0.61	0.55	0.21	0.24	0.26	1.10	0.39	0.61	0.10	0.24	0.26	1.21
1	0.11	0.41	0.21	0.19	0.28	1.00	0.21	0.33	0.19	0.35	0.17	1.22
2	0.44	0.41	0.48	0.19	0.44	1.06	0.31	0.43	0.07	0.37	0.26	1.04
3	0.22	0.71	0.30	0.29	0.33	1.27	0.41	0.60	0.04	0.52	0.39	0.96
4	0.23	0.63	0.15	0.30	0.37	0.71	0.69	0.91	0.05	0.46	0.62	1.43
5	0.26	0.30	0.09	0.41	0.54	1.17	0.37	1.68	0.08	0.32	0.59	1.52
6	0.37	0.52	0.13	0.42	0.82	1.11	0.55	0.75	0.03	0.36	1.06	0.82
7	0.46	0.69	0.15	0.29	0.86	1.04	0.21	0.27	0.03	0.33	1.25	1.28
8	0.26	0.17	0.23	0.15	0.90	1.03	0.10	0.13	0.04	0.30	1.10	0.89
9	0.06	0.12	0.09	0.34	1.38	1.79	0.11	0.31	0.02	0.18	0.78	1.09
10	0.08	0.14	0.06	0.18	0.84	1.04	0.18	0.10	0.03	0.19	0.89	1.29
11	0.23	0.13	0.08	0.33	0.49	0.97	0.16	0.13	0.01	0.19	1.14	1.70
12	0.12	0.29	0.06	0.21	0.62	1.63	0.13	0.16	0.01	0.15	0.82	0.83
13	0.08	0.12	0.14	0.24	0.89	1.18	0.08	0.23	0.03	0.16	1.03	1.21
14	0.25	0.19	0.11	0.21	0.67	1.74	0.17	0.21	0.05	0.17	0.86	1.53

Table-A III-6 Standard deviation of species concentration measurements for the S5 flame

	z* = 10%							**z* = 20%**						
Distance [mm]	CO [%]	CO_2 [%]	CH_4 [%]	H_2 [%]	H_2O [%]	O_2 [%]	N_2 [%]	CO [%]	CO_2 [%]	CH_4 [%]	H_2 [%]	H_2O [%]	O_2 [%]	N_2 [%]
0	0.63	0.57	0.04	0.15	0.13	0.82	0.82	0.67	0.47	0.08	0.40	0.43	0.45	0.54
1	0.41	0.22	0.23	0.17	0.17	0.53	1.00	0.45	0.54	0.14	0.31	0.55	0.22	1.18
2	0.49	0.72	0.05	0.45	0.23	0.39	0.91	0.40	0.43	0.11	0.53	0.20	0.18	0.63
3	0.74	0.87	0.31	0.13	0.24	0.29	0.96	0.74	0.73	0.15	0.36	0.23	0.17	1.42
4	0.62	0.89	0.12	0.28	0.64	0.49	0.82	0.30	1.18	0.26	0.24	0.22	0.10	1.18
5	0.38	0.43	0.05	0.10	0.25	0.48	0.89	0.37	0.82	0.14	0.12	0.42	0.29	1.78
6	0.22	0.22	0.04	0.09	0.24	0.94	1.26	0.54	0.45	0.20	0.13	0.15	0.36	1.97
7	0.14	0.27	0.07	0.07	0.33	0.81	1.64	0.23	1.11	0.19	0.13	0.45	0.46	1.25
8	0.12	0.25	0.02	0.07	0.28	0.59	0.91	0.22	0.36	0.13	0.12	0.37	0.45	0.92
9	0.15	0.13	0.04	0.01	0.30	0.95	1.08	0.32	0.37	0.03	0.02	0.33	0.48	1.38
10	0.11	0.21	0.03	0.07	0.25	1.57	1.36	0.07	0.32	0.04	0.02	0.22	0.89	1.32
11	0.20	0.20	0.03	0.05	0.17	0.66	1.60	0.09	0.37	0.09	0.03	0.13	0.98	1.58
12	0.11	0.12	0.02	0.09	0.20	1.13	0.90	0.12	0.20	0.03	0.04	0.15	1.26	1.47
13	0.14	0.17	0.05	0.07	0.08	1.07	1.32	0.36	0.32	0.04	0.03	0.21	0.77	1.32
14	0.14	0.16	0.02	0.04	0.19	1.00	1.02	0.08	0.16	0.01	0.02	0.07	1.00	1.93
	z* = 40%							**z* = 60%**						
Distance [mm]	CO [%]	CO_2 [%]	CH_4 [%]	H_2 [%]	H_2O [%]	O_2 [%]	N_2 [%]	CO [%]	CO_2 [%]	CH_4 [%]	H_2 [%]	H_2O [%]	O_2 [%]	N_2 [%]
0	0.70	0.40	0.09	0.05	0.41	0.29	0.83	0.19	0.06	0.03	0.08	0.19	0.39	1.33
1	0.28	0.79	0.09	0.07	0.17	0.30	1.11	0.20	0.46	0.09	0.14	0.27	0.29	0.86
2	0.32	0.50	0.13	0.05	0.34	0.49	1.03	0.46	0.55	0.03	0.11	0.18	0.51	0.83
3	0.51	0.68	0.10	0.14	0.46	0.45	0.83	0.50	0.31	0.18	0.23	0.25	0.48	1.86
4	0.33	0.62	0.05	0.05	0.54	0.41	0.91	0.23	0.52	0.07	0.06	0.21	0.35	1.16
5	0.47	0.83	0.04	0.20	0.22	0.28	1.66	0.23	0.21	0.15	0.06	0.37	0.89	1.43
6	0.40	0.61	0.06	0.06	0.31	0.55	0.89	0.06	0.35	0.07	0.02	0.29	0.56	1.59
7	0.14	0.52	0.06	0.10	0.18	0.89	1.30	0.26	0.26	0.08	0.05	0.26	0.38	1.44
8	0.18	0.21	0.03	0.08	0.28	1.76	1.80	0.25	0.22	0.07	0.05	0.27	0.56	0.99
9	0.19	0.13	0.01	0.10	0.20	0.67	0.93	0.07	0.27	0.01	0.04	0.21	1.17	1.48
10	0.27	0.23	0.05	0.08	0.24	0.91	1.12	0.26	0.43	0.02	0.04	0.09	1.33	1.17
11	0.14	0.09	0.04	0.02	0.10	1.06	0.99	0.18	0.10	0.01	0.05	0.19	0.67	1.23
12	0.11	0.28	0.06	0.10	0.11	0.81	1.95	0.12	0.22	0.05	0.02	0.08	0.61	1.22
13	0.09	0.19	0.03	0.05	0.13	0.67	1.45	0.19	0.18	0.01	0.08	0.20	0.78	1.68
14	0.15	0.18	0.01	0.09	0.24	0.76	1.11	0.16	0.13	0.03	0.06	0.17	1.35	1.25

Table-A III-7 Standard deviation of species concentration measurements for the S6 flame

	z* = 10%							**z* = 20%**						
Distance [mm]	CO [%]	CO_2 [%]	CH_4 [%]	H_2 [%]	H_2O [%]	O_2 [%]	N_2 [%]	CO [%]	CO_2 [%]	CH_4 [%]	H_2 [%]	H_2O [%]	O_2 [%]	N_2 [%]
0	0.86	0.71	0.02	0.16	0.18	0.63	0.72	0.76	0.88	0.10	0.35	0.44	0.12	1.61
1	0.61	0.58	0.10	0.34	0.40	0.24	0.71	1.63	0.44	0.18	0.06	0.55	0.10	0.79
2	1.03	1.16	0.17	0.29	0.40	0.33	0.92	0.58	0.55	0.18	0.25	0.19	0.18	0.83
3	0.51	0.77	0.11	0.32	0.43	0.39	1.08	0.20	0.79	0.18	0.11	0.62	0.19	0.93
4	0.26	0.33	0.06	0.20	0.45	0.60	1.25	0.45	0.82	0.19	0.10	0.79	0.21	1.87
5	0.18	0.85	0.06	0.06	0.48	0.89	1.41	0.29	0.73	0.20	0.10	0.38	0.86	0.68
6	0.23	0.43	0.05	0.12	0.34	0.78	1.45	0.50	0.26	0.15	0.03	0.27	0.98	1.42
7	0.27	0.40	0.04	0.07	0.15	1.02	1.05	0.12	0.35	0.12	0.07	0.45	0.64	1.15
8	0.08	0.12	0.06	0.02	0.13	0.64	1.46	0.27	0.22	0.06	0.06	0.38	0.94	1.74
9	0.12	0.10	0.02	0.01	0.16	1.15	1.12	0.11	0.37	0.06	0.03	0.18	1.39	1.38
10	0.09	0.14	0.06	0.02	0.12	1.76	1.02	0.06	0.19	0.03	0.05	0.37	1.20	1.09
11	0.14	0.10	0.01	0.02	0.23	1.01	1.15	0.12	0.31	0.03	0.05	0.18	0.93	1.75
12	0.12	0.12	0.06	0.01	0.22	0.95	1.35	0.28	0.11	0.02	0.03	0.26	0.70	1.65
13	0.18	0.27	0.05	0.04	0.12	1.35	1.05	0.12	0.15	0.02	0.04	0.21	1.17	1.27
14	0.17	0.20	0.02	0.02	0.22	0.74	1.28	0.09	0.26	0.01	0.04	0.15	0.53	1.26
	z* = 40%							**z* = 60%**						
Distance [mm]	CO [%]	CO_2 [%]	CH_4 [%]	H_2 [%]	H_2O [%]	O_2 [%]	N_2 [%]	CO [%]	CO_2 [%]	CH_4 [%]	H_2 [%]	H_2O [%]	O_2 [%]	N_2 [%]
0	0.55	0.67	0.13	0.07	0.21	0.22	0.83	0.58	0.55	0.12	0.36	0.27	0.27	0.99
1	0.29	0.77	0.07	0.06	0.36	0.23	1.42	0.67	0.51	0.08	0.31	0.23	0.36	0.90
2	0.39	0.75	0.02	0.06	0.23	0.28	1.05	0.48	0.46	0.15	0.09	0.33	0.18	0.53
3	0.38	0.92	0.12	0.26	0.59	0.15	1.23	0.48	1.07	0.14	0.20	0.35	0.12	0.61
4	0.28	0.44	0.24	0.18	0.70	0.34	1.35	0.20	0.76	0.15	0.05	0.36	0.50	0.46
5	0.22	0.75	0.16	0.10	0.34	0.82	1.01	0.64	0.55	0.16	0.21	0.39	0.65	0.80
6	0.34	0.38	0.06	0.06	0.26	0.95	1.17	0.25	0.47	0.06	0.12	0.43	0.43	1.27
7	0.17	0.33	0.04	0.21	0.30	0.81	0.98	0.35	0.21	0.12	0.04	0.49	0.55	0.80
8	0.26	0.20	0.06	0.11	0.26	1.15	0.86	0.07	0.23	0.04	0.07	0.42	1.05	1.22
9	0.17	0.22	0.01	0.08	0.28	0.86	1.41	0.16	0.28	0.02	0.03	0.13	0.84	1.47
10	0.13	0.18	0.02	0.11	0.18	1.03	0.94	0.21	0.31	0.02	0.04	0.13	0.74	0.79
11	0.28	0.22	0.07	0.06	0.33	1.25	1.25	0.27	0.23	0.04	0.03	0.22	0.62	0.52
12	0.21	0.26	0.03	0.05	0.13	0.54	0.88	0.14	0.22	0.02	0.01	0.23	0.72	1.50
13	0.10	0.11	0.03	0.05	0.31	1.59	1.15	0.08	0.10	0.03	0.03	0.17	0.72	0.96
14	0.19	0.19	0.03	0.05	0.19	0.67	0.78	0.32	0.17	0.01	0.06	0.17	0.88	1.71

Table-A III-8 Standard deviation of species concentration measurements for the S5M50 flame

	z* = 10%							**z* = 20%**						
Distance [mm]	CO [%]	CO_2 [%]	CH_4 [%]	H_2 [%]	H_2O [%]	O_2 [%]	N_2 [%]	CO [%]	CO_2 [%]	CH_4 [%]	H_2 [%]	H_2O [%]	O_2 [%]	N_2 [%]
0	0.20	0.06	0.26	0.15	0.04	0.85	0.55	0.23	0.16	0.08	0.11	0.04	0.41	0.86
1	0.30	0.18	0.16	0.22	0.07	0.80	0.48	0.51	0.20	0.55	0.15	0.07	0.50	0.95
2	0.33	0.25	0.84	0.33	0.19	0.47	0.91	0.64	0.16	0.12	0.35	0.16	0.89	0.76
3	0.53	0.48	0.91	0.11	0.32	0.24	0.83	0.77	0.18	0.50	0.06	0.10	0.59	0.82
4	0.69	0.22	0.20	0.05	0.38	0.06	0.55	0.91	0.33	0.16	0.25	0.17	0.19	0.54
5	0.15	0.21	0.04	0.01	0.29	0.09	0.77	0.83	0.40	0.23	0.07	0.31	0.22	0.98
6	0.31	0.45	0.02	0.04	0.54	0.11	0.60	0.25	0.51	0.24	0.08	0.60	0.12	0.90
7	0.08	0.34	0.01	0.04	0.25	0.38	1.03	0.61	0.27	0.13	0.12	0.61	0.16	0.88
8	0.11	0.11	0.01	0.02	0.64	0.45	1.05	0.58	0.54	0.07	0.16	0.24	0.41	0.49
9	0.11	0.20	0.01	0.01	0.34	0.46	0.93	0.56	0.51	0.05	0.25	0.41	0.42	0.82
10	0.03	0.04	0.01	0.01	0.28	0.67	1.09	0.20	0.19	0.02	0.04	0.16	0.33	1.15
11	0.02	0.07	0.01	0.03	0.19	0.65	1.02	0.27	0.21	0.02	0.13	0.14	0.86	1.36
12	0.05	0.06	0.00	0.01	0.21	0.64	1.26	0.59	0.19	0.01	0.04	0.25	0.91	1.01
13	0.02	0.05	0.00	0.01	0.12	0.60	0.74	0.24	0.16	0.02	0.01	0.14	0.59	1.05
14	0.03	0.05	0.00	0.01	0.11	0.50	0.62	0.16	0.14	0.02	0.04	0.28	0.65	1.00
15	0.02	0.04	0.01	0.02	0.27	0.77	0.53	0.06	0.03	0.01	0.02	0.11	0.33	0.81

Table-A III-9 Standard deviation of species concentration measurements for the S5M25 flame

	z* = 10%							**z* = 20%**						
Distance [mm]	CO [%]	CO_2 [%]	CH_4 [%]	H_2 [%]	H_2O [%]	O_2 [%]	N_2 [%]	CO [%]	CO_2 [%]	CH_4 [%]	H_2 [%]	H_2O [%]	O_2 [%]	N_2 [%]
0	0.61	0.61	0.46	0.13	0.02	0.69	0.44	0.56	0.32	0.07	0.25	0.28	0.13	0.67
1	0.87	0.47	0.38	0.12	0.08	0.62	0.60	0.60	0.52	0.18	0.17	0.49	0.07	0.96
2	0.56	0.80	0.52	0.18	0.10	0.90	0.37	0.96	0.66	0.24	0.10	0.39	0.07	0.86
3	0.62	1.09	0.49	0.44	0.46	0.13	0.54	0.62	0.66	0.13	0.09	0.30	0.05	0.60
4	0.68	0.72	0.33	0.17	0.38	0.12	1.26	0.65	0.33	0.08	0.04	0.21	0.10	1.09
5	0.48	0.70	0.03	0.26	0.49	0.71	1.04	0.40	0.12	0.04	0.03	0.74	0.26	0.73
6	0.49	0.86	0.16	0.08	0.26	0.85	0.72	0.17	0.64	0.01	0.02	0.61	0.42	1.16
7	0.23	0.53	0.03	0.05	0.32	0.76	0.73	0.23	0.38	0.01	0.08	0.16	0.41	0.79
8	0.17	0.19	0.09	0.08	0.22	0.56	1.71	0.15	0.57	0.02	0.11	0.23	0.62	0.81
9	0.14	0.13	0.02	0.04	0.18	0.62	1.06	0.09	0.26	0.03	0.02	0.28	0.78	0.95
10	0.16	0.12	0.02	0.03	0.20	0.77	1.11	0.13	0.16	0.01	0.03	0.14	0.54	0.86
11	0.11	0.10	0.02	0.02	0.14	0.35	1.14	0.13	0.32	0.01	0.03	0.18	0.83	0.46
12	0.09	0.09	0.01	0.02	0.20	0.52	0.76	0.16	0.12	0.02	0.04	0.24	0.55	0.65
13	0.17	0.10	0.02	0.03	0.12	0.22	1.26	0.09	0.10	0.02	0.02	0.20	0.49	0.55
14	0.19	0.15	0.02	0.01	0.19	0.80	1.39	0.07	0.17	0.01	0.02	0.14	0.57	0.76
	z* = 40%							**z* = 60%**						
Distance [mm]	CO [%]	CO_2 [%]	CH_4 [%]	H_2 [%]	H_2O [%]	O_2 [%]	N_2 [%]	CO [%]	CO_2 [%]	CH_4 [%]	H_2 [%]	H_2O [%]	O_2 [%]	N_2 [%]
0	0.51	0.56	0.10	0.19	0.54	0.16	0.53	0.35	0.34	0.04	0.11	0.31	0.36	1.20
1	0.38	0.53	0.06	0.26	0.27	0.09	0.97	0.28	0.77	0.10	0.04	0.30	0.22	0.64
2	0.34	0.37	0.08	0.22	0.18	0.09	1.05	0.31	0.24	0.13	0.22	0.48	0.23	0.68
3	0.16	0.80	0.17	0.23	0.45	0.09	0.56	0.15	0.53	0.18	0.18	0.51	0.34	0.79
4	0.15	0.64	0.19	0.23	0.42	0.15	0.96	0.30	0.33	0.08	0.22	0.38	0.27	1.07
5	0.24	0.59	0.04	0.13	0.27	0.43	1.19	0.41	1.01	0.03	0.19	0.70	0.26	0.80
6	0.30	0.36	0.09	0.11	0.45	0.42	1.14	0.16	0.67	0.06	0.10	0.28	0.60	1.15
7	0.14	0.41	0.02	0.09	0.22	0.61	1.02	0.38	0.38	0.05	0.10	0.29	0.86	1.33
8	0.21	0.30	0.03	0.03	0.17	0.68	1.22	0.11	0.40	0.03	0.05	0.22	0.63	0.79
9	0.11	0.31	0.04	0.02	0.24	0.69	1.10	0.24	0.09	0.01	0.05	0.23	0.83	1.26
10	0.17	0.20	0.01	0.08	0.39	0.61	1.25	0.16	0.19	0.02	0.03	0.29	0.69	1.06
11	0.12	0.26	0.02	0.05	0.21	0.75	1.37	0.14	0.16	0.05	0.04	0.21	0.45	0.64
12	0.07	0.17	0.02	0.04	0.40	0.48	0.83	0.12	0.13	0.01	0.01	0.16	0.56	0.96
13	0.15	0.28	0.01	0.03	0.14	0.78	0.75	0.14	0.26	0.04	0.02	0.19	0.43	0.88
14	0.08	0.19	0.04	0.01	0.18	0.73	0.84	0.09	0.13	0.03	0.03	0.25	0.39	0.56

APPENDIX IV

LAMINAR FLAME SPEED SIMULATION

The following is a collection of data concerning laminar flame speed from the project's original scope. The numerical and experimental investigation of laminar flame speed of the ten fuels was dropped from the study after these results were obtained. Numerical combustion simulations were conducted with CHEMKIN III, a software that solves complex chemical kinetics by using mechanisms of elementary chemical reactions and rate constant expressions. The Gri-MECH 3.0 mechanism, the H2-CO mechanism, and the Rolls Royce Canada in-house mechanism were used to solve the chemical kinetics problems. The H2-CO mechanism was used for syngas mixtures without CH_4 addition, whereas the Gri-MECH 3.0 mixture was used for all mixtures containing CH_4.

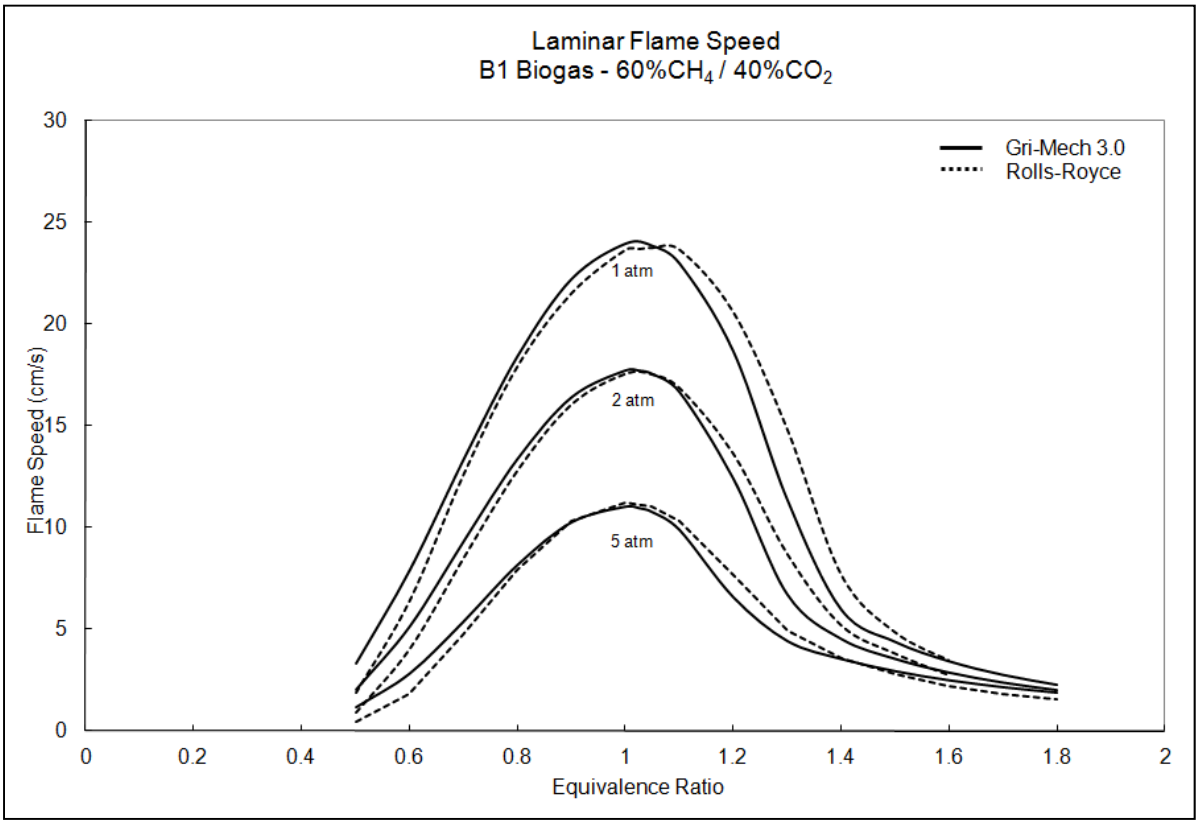

Figure-A IV- 1 Laminar flame speed with respect to equivalence ratio of B1 flame

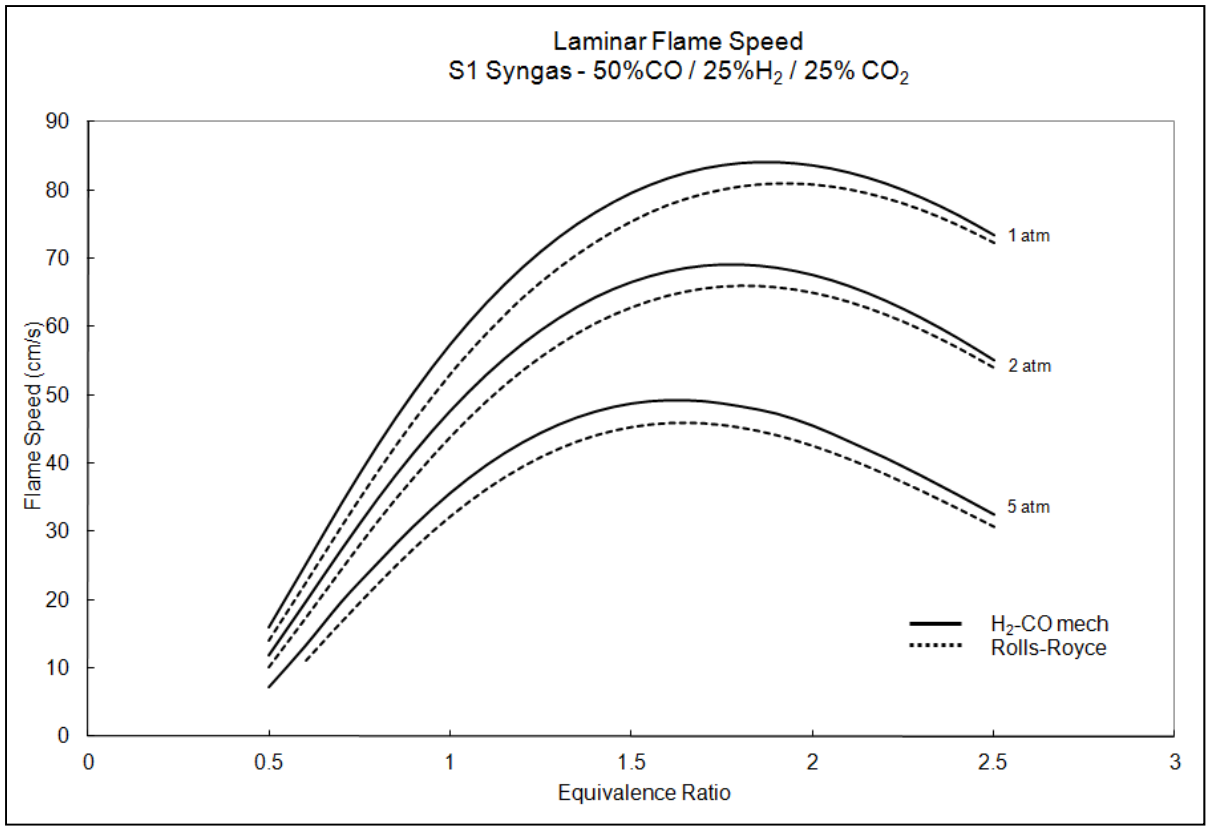

Figure-A IV- 2 Laminar flame speed with respect to equivalence ratio of S1 flame

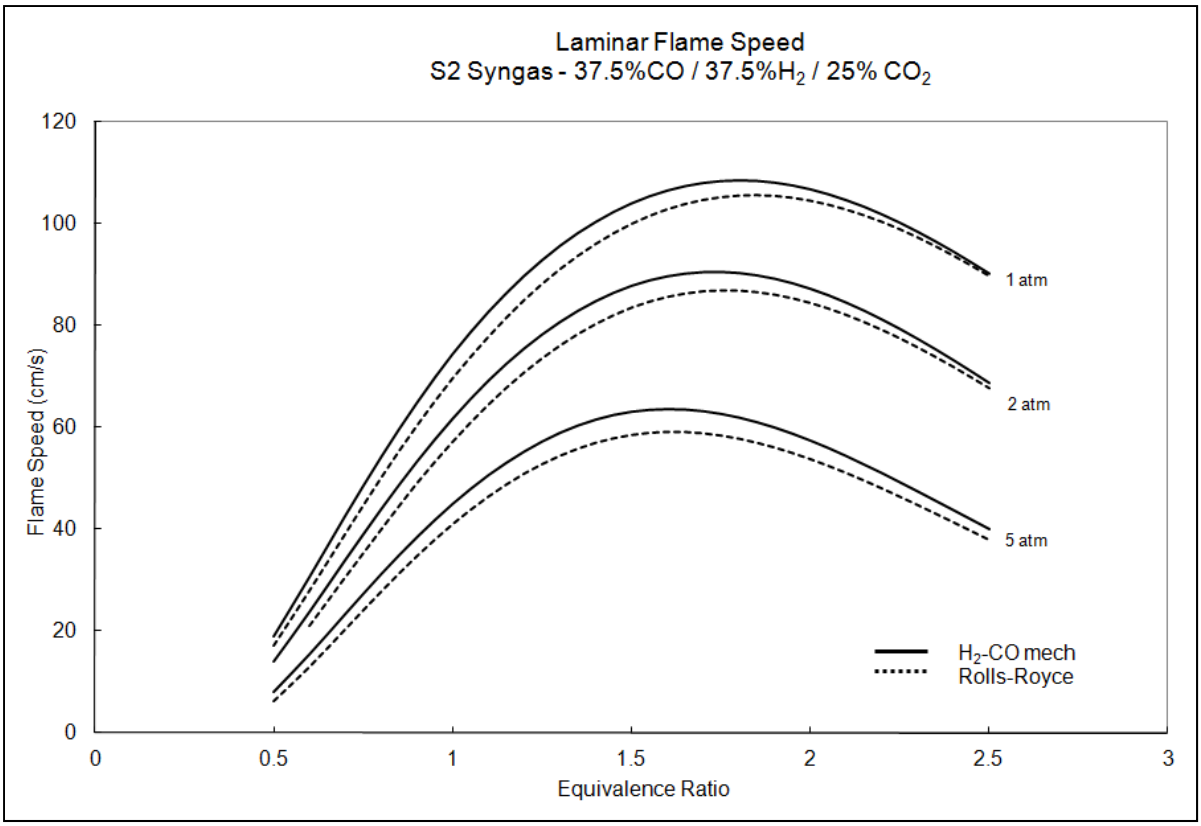

Figure-A IV- 3 Laminar flame speed with respect to equivalence ratio of S2 flame

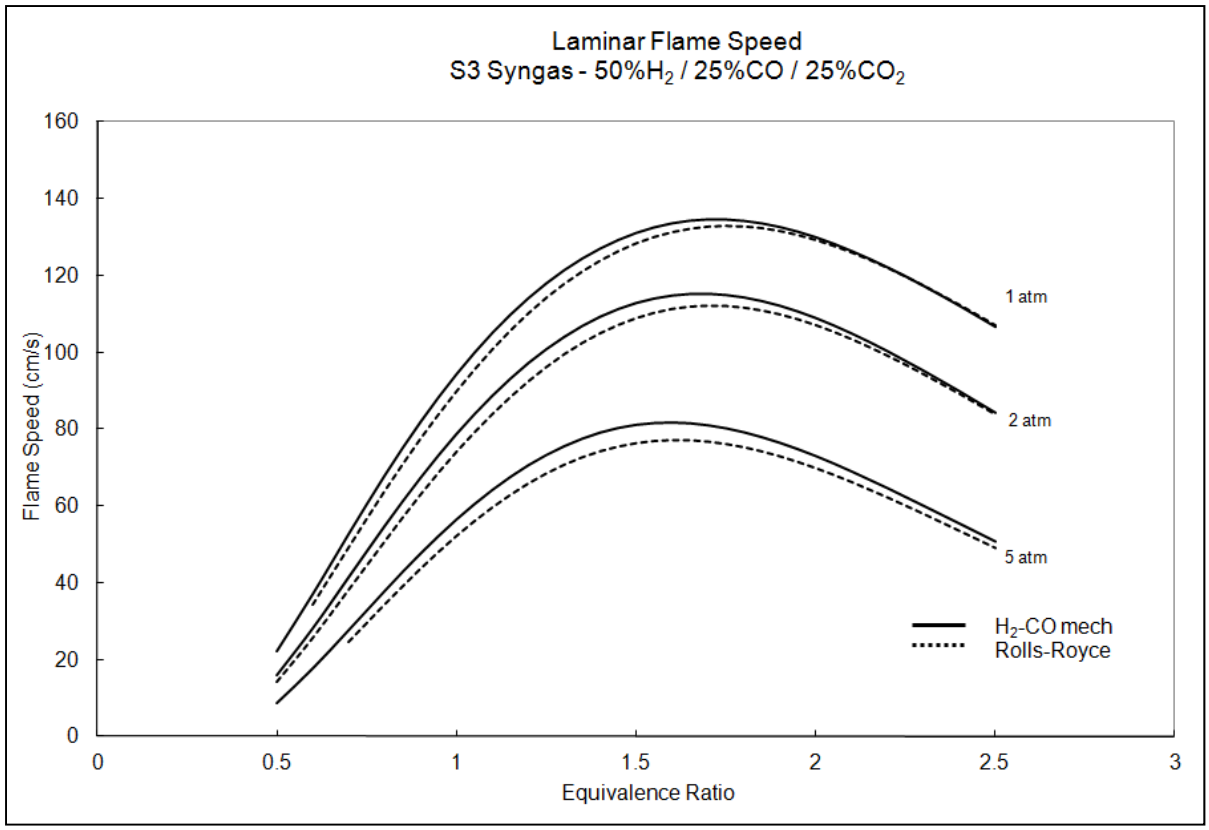

Figure-A IV- 4 Laminar flame speed with respect to equivalence ratio of S3 flame

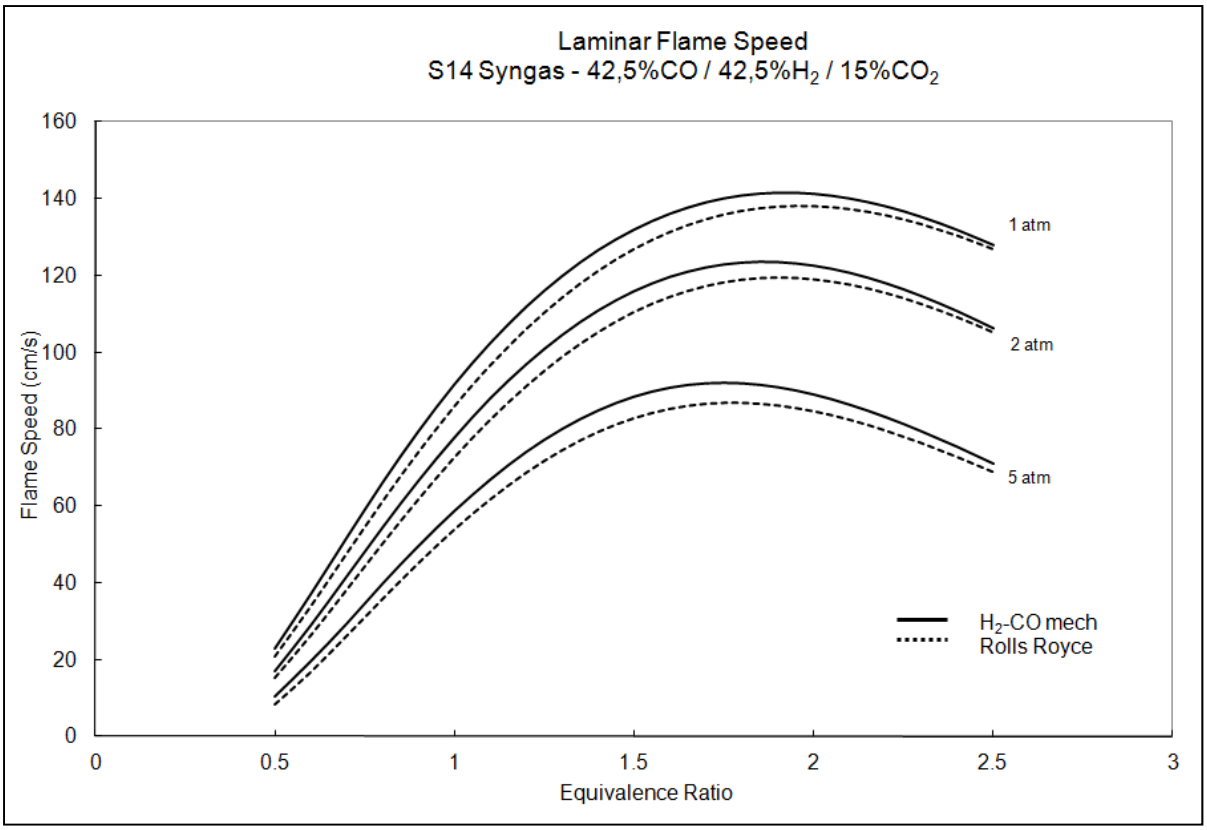

Figure-A IV- 5 Laminar flame speed with respect to equivalence ratio of S14 flame

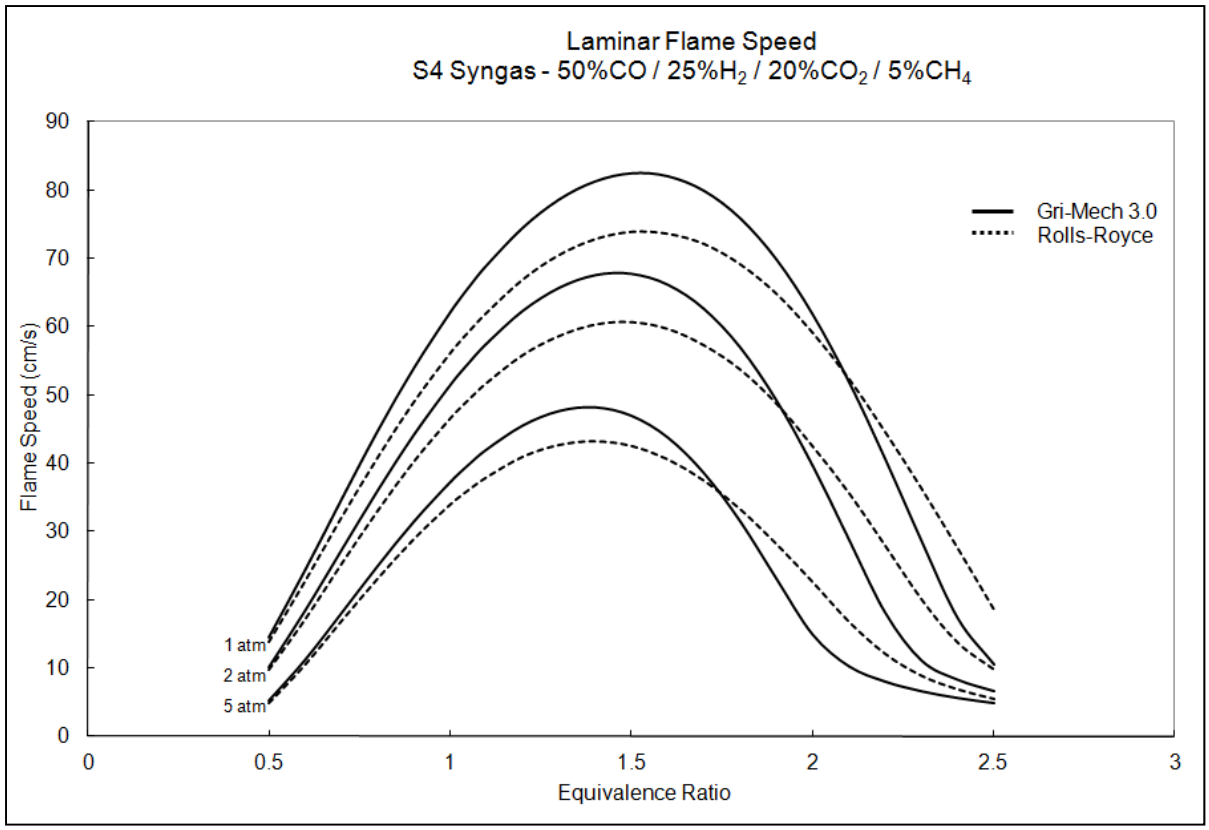

Figure-A IV- 6 Laminar flame speed with respect to equivalence ratio of S4 flame

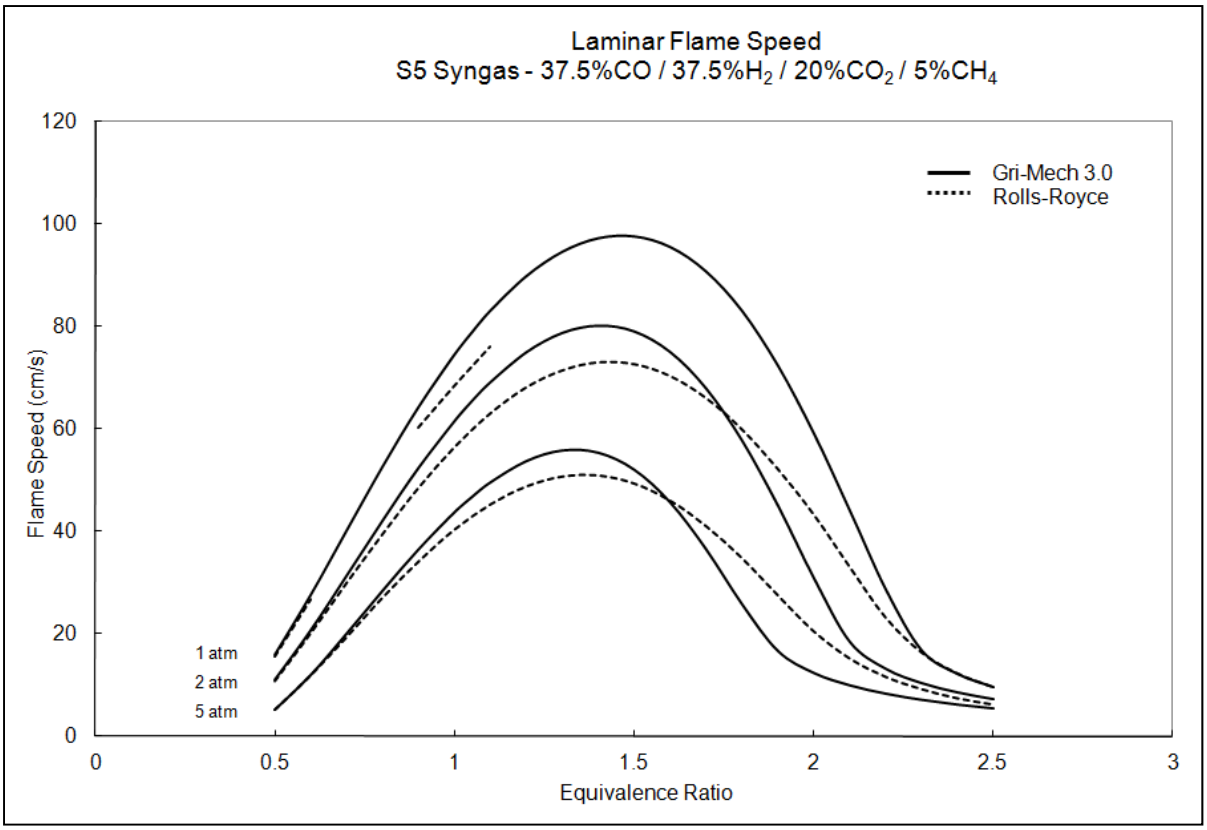

Figure-A IV- 7 Laminar flame speed with respect to equivalence ratio of S5 flame

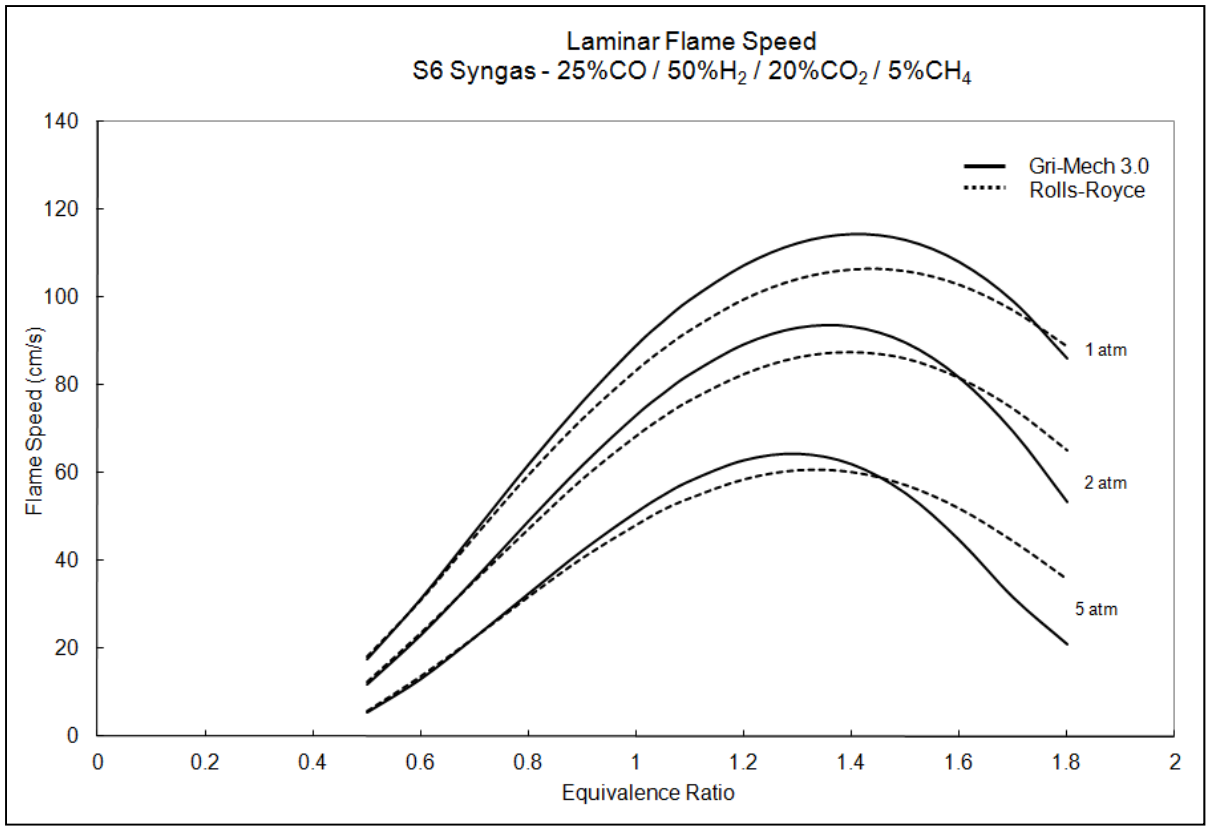

Figure-A IV- 8 Laminar flame speed with respect to equivalence ratio of S6 flame

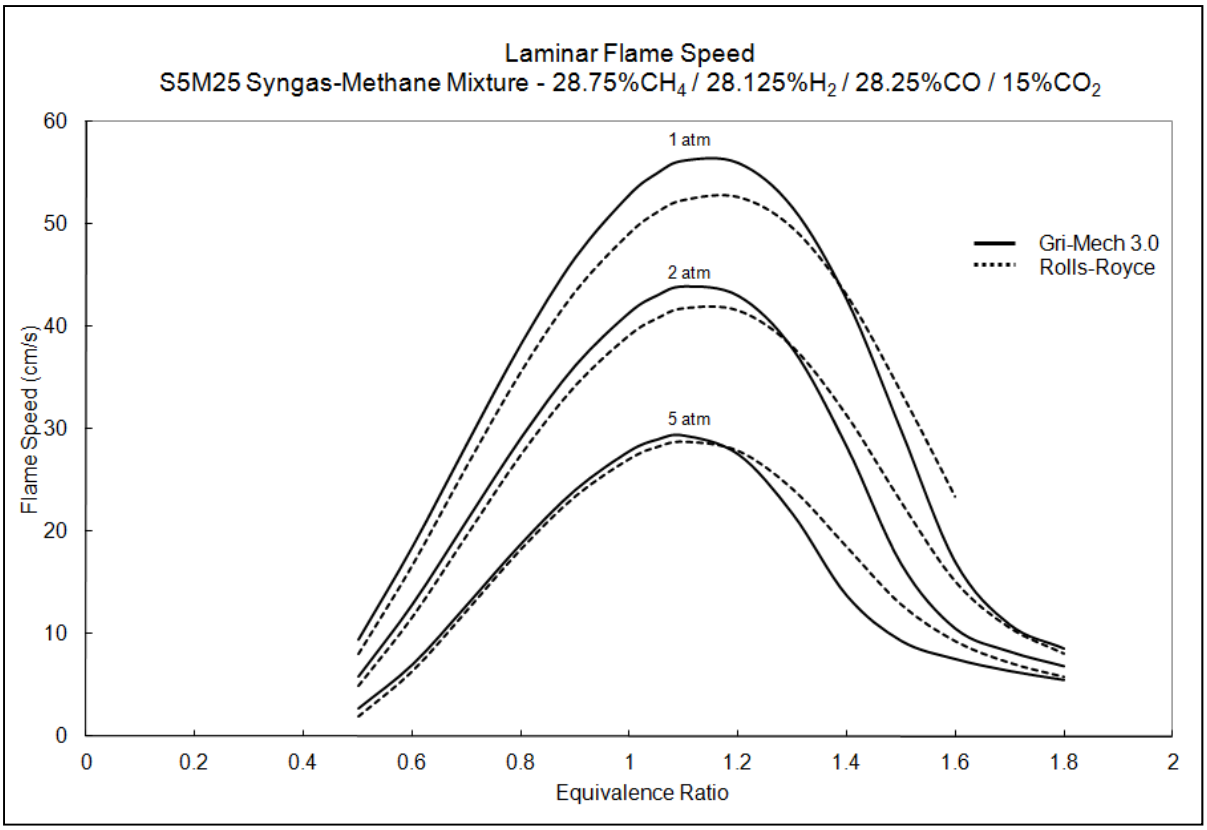

Figure-A IV- 9 Laminar flame speed with respect to equivalence ratio of S5M25 flame

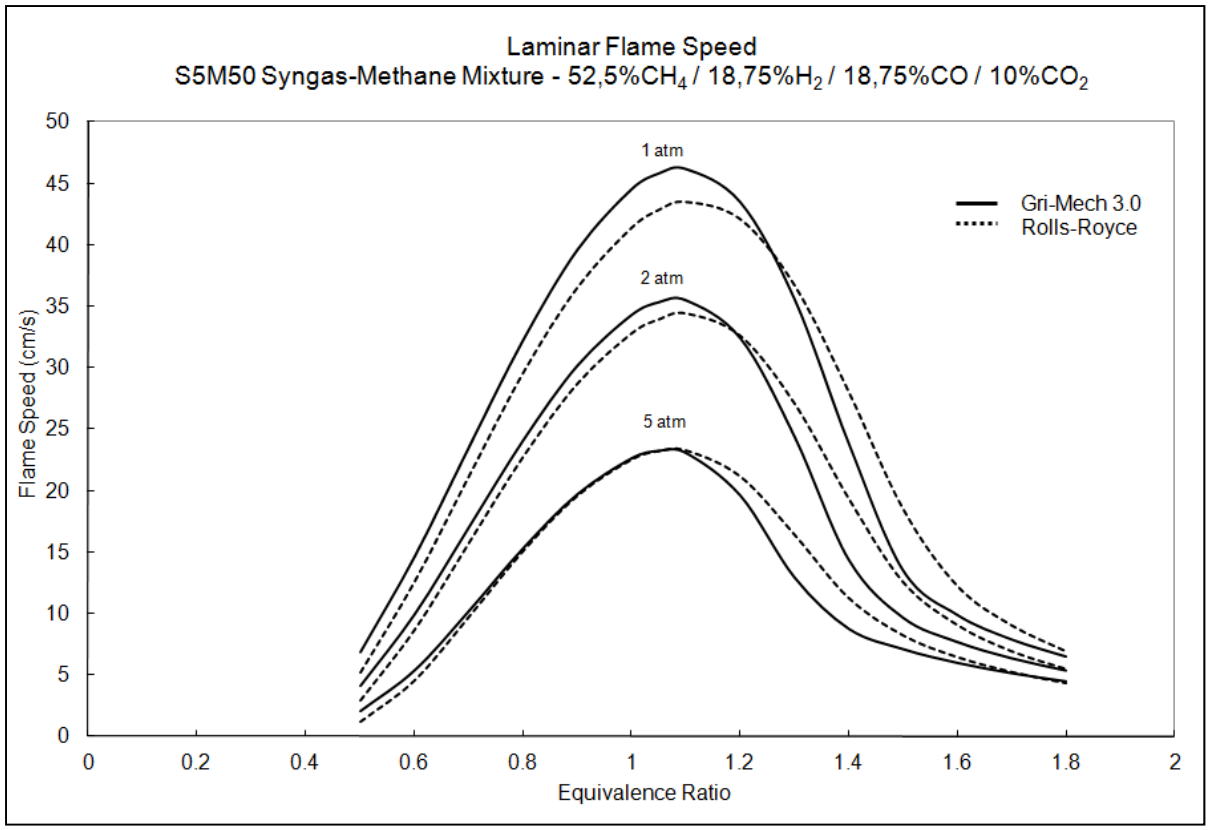

Figure-A IV- 10 Laminar flame speed with respect to equivalence ratio of S5M50 flame

BIBLIOGRAPHY

ANSYS, Inc., Fluent (2006). "ANSYS FLUENT User's Guide". Online: <https://www.sharcnet.ca/Software/Fluent12/html/ug/node3.htm>

Bouvet, N., C. Chauveau, I. Gökalp, S. Y. Lee and R. J. Santoro (2011). "Characterization of syngas laminar flames using the Bunsen burner configuration." International Journal of Hydrogen Energy **36**(1): 992-1005.

Burbano, H. J., J. Pareja and A. A. Amell (2011). "Laminar burning velocities and flame stability analysis of H2/CO/air mixtures with dilution of N2 and CO2." International Journal of Hydrogen Energy **36**(4): 3232-3242.

Cheng, T. S., Y. C. Chang, Y. C. Chao, G. B. Chen, Y. H. Li and C. Y. Wu (2011). "An experimental and numerical study on characteristics of laminar premixed H2/CO/CH4/air flames." International Journal of Hydrogen Energy **In Press, Corrected Proof**.

Cohé, C., C. Chauveau, I. Gökalp and D. F. Kurtuluş (2009). "CO2 addition and pressure effects on laminar and turbulent lean premixed CH4 air flames." Proceedings of the Combustion Institute **32**(2): 1803-1810.

Dahoe, A. E. and L. P. H. de Goey (2003). "On the determination of the laminar burning velocity from closed vessel gas explosions." Journal of Loss Prevention in the Process Industries **16**(6): 457-478.

Echekki, T. and M. G. Mungal (1991). "Flame speed measurements at the tip of a slot burner: Effects of flame curvature and hydrodynamic stretch." Symposium (International) on Combustion **23**(1): 455-461.

Gu, X. J., M. Z. Haq, M. Lawes and R. Woolley (2000). "Laminar burning velocity and Markstein lengths of methane-air mixtures." Combustion and Flame **121**(1-2): 41-58.

Han, B., A. F. Ibarreta, C. J. Sung and James S. T'ien (2006). "Structure of low-stretch methane nonpremixed flames." Combustion and Flame **149**: 173-190.

Hariharan, P., C. Periasamy and S. R. Gollahalli (2007). "Effect of elliptic burner geometry and air equivalence ratio on the nitric oxide emissions from turbulent hydrogen flames." International Journal of Hydrogen Energy **32**(8): 1095-1102.

Hayashida, K., Kenji Amagai, Keiji Satoh and Masataka Arai (2006). "Measurement of Fuel Concentration Distribution in a Sooting Flame through Raman Scattering." JSME International Journal Series B Fluids and Thermal Engineering **49**(2): 512-519.

Hendra, P. (2004) "Raman Spectroscopy." The Internet Journal of Vibrational Spectroscopy.

Hollas, J. M. (2004). Modern Spectroscopy. West Sussex, England, John Wiley & Sons, Ltd.

Hu, E., Z. Huang, J. He and H. Miao (2009). "Experimental and numerical study on laminar burning velocities and flame instabilities of hydrogen-air mixtures at elevated pressures and temperatures." International Journal of Hydrogen Energy **34**(20): 8741-8755.

Lafay, Y., B. Renou, G. Cabot and M. Boukhalfa (2008). "Experimental and numerical investigation of the effect of H2 enrichment on laminar methane–air flame thickness." Combustion and Flame **153**(4): 540-561.

Law, C. K. (2006). Combustion physics. Cambridge; New York, Cambridge University Press.

Lee, J. and S. H. Chung (2001). "Characteristics of reattachment and blowout of laminar lifted flames in partially premixed propane jets." Combustion and Flame **127**(4): 2194-2204.

Lee, T. W. (2008). Thermal and flow measurements. Boca Raton, CRC Press.

Lyle, K. H., L. K. Tseng, J. P. Gore and N. M. Laurendeau (1999). "A study of pollutant emission characteristics of partially premixed turbulent jet flames." Combustion and Flame **116**(4): 627-639.

Manton, J., G. von Elbe and B. Lewis (1953). "Burning-velocity measurements in a spherical vessel with central ignition." Symposium (International) on Combustion **4**(1): 358-363.

Moffat, R. (1988). "Describing the Uncertainties in Experimental Results." Experimental Thermal and Fluid Science **1**(1): 3-17.

Mohammad, B., S.-M. Jeng and G. Andac (2010). "Influence of Primary Jets and Fuel Injection on the Aerodynamics of a Prototype Annular Gas Turbine Combustor Sector." Journal of Engineering for Gas Turbines and Power **133**.

Monteiro, E., M. Bellenoue, J. Sotton, N. A. Moreira and S. Malheiro (2010). "Laminar burning velocities and Markstein numbers of syngas-air mixtures." Fuel **89**(8): 1985-1991.

Natarajan, J., T. Lieuwen and J. Seitzman (2007). "Laminar flame speeds of H2/CO mixtures: Effect of CO2 dilution, preheat temperature, and pressure." Combustion and Flame **151**(1-2): 104-119.

Ouimette, P. (2012). Caractérisation expérimentale et numérique de la flamme de carburants synthétiques gazeux. Mechanical Engineering. Montréal, École de technologie supérieure. **Ph. D.:** 178.

Park, J., D. S. Bae, M. S. Cha, J. H. Yun, S. I. Keel, H. Chang Cho, T. K. Kim and J. S. Ha (2008). "Flame characteristics in H2/CO synthetic gas diffusion flames diluted with CO2: Effects of radiative heat loss and mixture composition." International Journal of Hydrogen Energy **33**(23): 7256-7264.

Prathap, C., A. Ray and M. R. Ravi (2008). "Investigation of nitrogen dilution effects on the laminar burning velocity and flame stability of syngas fuel at atmospheric condition." Combustion and Flame **155**(1-2): 145-160.

Rabenstein, F. L., Alfred (1998). "One-Dimensional, Time-Resolved Raman Measurements in a Sooting Flame made with 355-nm Excitation." Applied Optics **37**(21): 4937-4943.

Rallis, C. J. and A. M. Garforth (1980). "The determination of laminar burning velocity." Progress in Energy and Combustion Science **6**(4): 303-329.

Shepherd, C., and M.S. Day (2003). The Dynamics of Flame Flicker in Conical Premixed Flames: An Experimental and Numerical Study. AETD. Berkeley, Lawrence Berkely National Laboratory.

Stewart, J. (1991). Calculus. Pacific Grove, Calif., Brooks/Cole Pub. Co.

Sutton, J. A. and J. F. Driscoll (2004). "Rayleigh Scattering Cross Sections of Combustion Species at 266, 355, and 532 nm for Thermometry Applications." Optics Letters **29**(22): 2620-2622.

Tang, C., J. He, Z. Huang, C. Jin, J. Wang, X. Wang and H. Miao (2008). "Measurements of laminar burning velocities and Markstein lengths of propane-hydrogen-air mixtures at elevated pressures and temperatures." International Journal of Hydrogen Energy **33**(23): 7274-7285.

Tang, C., Z. Huang, C. Jin, J. He, J. Wang, X. Wang and H. Miao (2008). "Laminar burning velocities and combustion characteristics of propane-hydrogen-air premixed flames." International Journal of Hydrogen Energy **33**(18): 4906-4914.

Tse, S. D., D. L. Zhu and C. K. Law (2000). "Morphology and burning rates of expanding spherical flames in H2/O2/inert mixtures up to 60 atmospheres." Proceedings of the Combustion Institute **28**(2): 1793-1800.

Williams, F. A., Ed. (1985). Combustion Theory. Reading, Mass., Addison-Wesley Pub. Co.

Zimmerman, Dr. WBJ and Dr. R I Ristic. (1999). CPE630: Introduction to Fuel and Energy: Notes from the course CPE-630. Department of Chemical and Process Engineering Masters Program, Sheffield: University of Sheffield.